

3857

JNCASR
Acc No. 3857
LIBRARY

LIBRARY
JAWAHARLAL NEHRU CENTRE
FOR ADVANCED SCIENTIFIC RESEARCH
JAKKUR POST
BANGALORE-560 064

JNCASR LIBRARY
3857


536.7 P06

Topics in Dynamics, Thermodynamics and Electronic Structure of Supercooled Liquids

A Thesis

Submitted For the Degree of
DOCTOR OF PHILOSOPHY
in the Faculty of Science

by

Ashwin S. Sampangiraj



THEORETICAL SCIENCES UNIT
JAWAHARLAL NEHRU CENTRE FOR ADVANCED SCIENTIFIC
RESEARCH

Bangalore – 560 064

FEBRUARY 2006

536.7

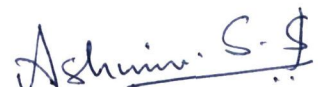
PO6

I dedicate this thesis to my parents.

DECLARATION

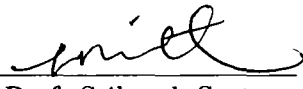
I hereby declare that the matter embodied in the thesis entitled “**Topics in Dynamics, Thermodynamics and Electronic Structure of Supercooled Liquids**” is the result of investigations carried out by me at the Theoretical Sciences Unit, Jawaharlal Nehru Centre for Advanced Scientific Research, Bangalore, India under the supervision of Prof. Srikanth Sastry and that it has not been submitted elsewhere for the award of any degree or diploma.

In keeping with the general practice in reporting scientific observations, due acknowledgement has been made whenever the work described is based on the findings of other investigators.


Ashwin S. Sampangiraj

CERTIFICATE

I hereby certify that the matter embodied in this thesis entitled “**Topics in Dynamics, Thermodynamics and Electronic Structure of Super-cooled Liquids**” has been carried out by Mr. Ashwin S. Sampangiraj at the Theoretical Sciences Unit, Jawaharlal Nehru Centre for Advanced Scientific Research, Bangalore, India under my supervision and that it has not been submitted elsewhere for the award of any degree or diploma.


Prof. Srikanth Sastry
(Research Supervisor)

Acknowledgements

I firstly like to thank my advisor Prof. Srikanth Sastry for his unmatched patience, sincerity, guidance, and for being an example of true professionalism. I would like to thank my collaborators Prof. U. Waghmare and Prof. G.I. Menon for their support, encouragement and guidance. I wish to thank my teachers Prof. Balasubramanian, Prof. S. Narasimhan, Prof. R. Pandit, Prof. Sriram Ramaswamy, Prof. T.V. Ramakrishnan, Prof. B. S. Shastry and Prof. R. Nityananda. Thanks to Bhaswati, Niels, Shibu, Krishnan, Joydeep, Lakshmi, Pushpa and all my other lab mates. I wish to also thank all my other friends at JNCASR. Finally I would like to thank my family, who have been of constant support and strength over the years.

Synopsis

This is a synopsis of the thesis entitled “**Topics in Dynamics, Thermodynamics and Electronic Structure of Supercooled Liquids.**”, delivered by Ashwin S. Sampangiraj of the Theoretical Sciences Unit, Jawaharlal Nehru Centre for Advanced Scientific Research, Bangalore, India. The thesis is divided into the following five parts.

- The dynamical behaviour of glass-forming liquids have been analyzed extensively *via* computer simulations of model liquids, among which the Kob-Andersen binary Lennard-Jones mixture has been a widely studied system. Typically, studies of this model have been restricted to temperatures above the mode coupling temperature. Preliminary results concerning the dynamics of the Kob-Andersen binary mixture are presented at temperatures that extend below the mode coupling temperature, along with properties of the local energy minima sampled. We show that a crossover in the dynamics occurs, alongside changes in the properties of the local energy minima sampled, from non-Arrhenius behaviour of the diffusivity above the mode coupling temperature, to Arrhenius behaviour at lower temperatures.

- Computer simulations, using the Stillinger-Weber potential, have previously been employed to demonstrate a liquid-liquid transition in supercooled silicon near 1060 K. From calculations of electronic structure using an empirical pseudopotential, we show that silicon undergoes an associated metal to semi-metal transition with a resistivity jump of roughly one order of magnitude. We show that the electronic states near the Fermi energy become localized in the low temperature phase, and that changes in electronic structure between the two phases arise from a change in atomic structure, and not from a change in density. We also investigate the electronic structure of the quenched structures in these two phases.
- We investigate the mechanical properties of several model liquids and corresponding local energy minima (inherent structures) in an attempt to explore their connection to slow dynamics and vitrification. In particular, we study the correlation between the distribution of forces between particles and the approach to the glass transition in a variety of liquids (with both attractive and repulsive interactions), including network forming liquid silicon, and silica. Such a correlation has been proposed, in analogy with granular materials, within the framework of a unified “jamming phase diagram” and has been studied for some model liquids through simulations recently. We postulate that the plateau behaviour at low forces is related to the fragility of the glass former, and provide preliminary supporting evidence. We also consider the critical strain amplitude needed to cause inherent structure transitions,

and show that the critical strain correlates with the depth of the local energy minima and the onset of slow dynamics.

- The stability of a liquid is bounded by the liquid-gas spinodal and the ideal glass transition. We calculate these stability boundaries using the Mezard-Parisi method for evaluating the thermodynamic glass transition and the Zerah-Hansen scheme for the equation of state of a model liquid. These two limiting boundaries intersect at a finite temperature. Our calculations are consistent with results from a previous work based on computer simulations.
- Using Müller-Plathe's method for calculating viscosity in computer simulations, we demonstrate the break down of the Stokes-Einstein relation between a liquid's viscosity and diffusivity. We calculate the viscosity and the diffusivity at various temperatures across the onset temperature of slow dynamics. We verify that the hydrodynamic radius does not remain a constant below the onset temperature. This is a signature of the break down of the Stokes-Einstein relation.

Nomenclature

α_p : Thermal expansion coefficient

ρ : Density

ω : Frequency

τ : Relaxation time

η : Viscosity

e^- : Electron

C_p : Specific heat constant pressure

C_v : Specific heat constant volume

DFT: Density Functional theory

EOS: Equation of state

ES : Electronic Structure

E_f : Fermi energy

D : Diffusivity

DOS: Density of states

g(r): Radial distribution function

HNC: Hypernetted Chain

IPR: Inverse participation ratio

IS: Inherent structure

k_B: Boltzmann constant

KABMLJ : Kob-Andersen binary Lennard Jones

LL: Liquid to liquid transition

MC: Monte Carlo

MCT: Mode coupling theory

MD: Molecular dynamics

MP: Monkhorst-Pack

MSD: Mean square displacement

N: Number of atoms

P: Pressure

P(f): Force distribution

PY: Percus-Yevick

REMC: Restricted ensemble Monte Carlo

T : Temperature

T_c, T_{MCT} : Mode coupling temperature

T_g : Glass transition temperature

T_K : Kauzmann temperature

T_M : Melting temperature

T_s : Onset of slow dynamics temperature

RY : Roger-Young

S : Entropy

S_c : Configurational Entropy

S_{vib} : Vibrational Entropy

V : Volume

VFT : Vogel-Fulcher-Tamman

ZH : Zerah-Hansen

Contents

Acknowledgements	iii
Synopsis	iv
Nomenclature	vii
1 Introduction	1
1.1 Introduction to Supercooled Liquids	2
1.1.1 Phenomenology of Glass Formation	3
1.1.2 Temperature Dependence of Viscosity	4
1.1.3 Relaxation in the Supercooled Regime	8
1.2 Energy Landscape in Supercooled Liquids	11
1.3 The Kauzmann Paradox	17
1.4 Thermodynamic Approach to Glass Transition	18
1.5 Computer Simulations in Glass Forming Liquids	24
1.5.1 Molecular Dynamics	24
1.5.2 Monte Carlo	30
1.5.3 Ewald Sum	30
1.5.4 Energy Minimization	37

1.6	Outline of the Thesis	39
2	Low-Temperature Behaviour of the Kob-Andersen binary mixture	40
2.1	Introduction	40
2.2	Computational details	43
2.3	Results	44
2.4	Summary	48
3	Electronic Structure of Supercooled Liquid Silicon	51
3.1	Introduction	51
3.2	Elements of Electronic Structure	52
3.3	Electronic Structure in Non-Crystalline Materials	57
3.4	Liquid-Liquid Phase Transition in Si	61
3.4.1	Simulation of Liquid Silicon	62
3.5	The Hamiltonian	65
3.5.1	Modified Pseudopotential	66
3.6	Procedure for Solving the Hamiltonian	68
3.6.1	Conjugate Directions	69
3.6.2	Search for the Minimum (Circle Minimization)	71
3.7	Results	71
3.7.1	Density of States	72
3.7.2	Density of States in Energy and Inverse Participation Ratio	72
3.7.3	Resistivity	73
3.8	Pinpointing the Cause of Conductivity change	80

3.9	Comparison with First Principles Density Functional Theory	87
3.10	Electronic Structure of Inherent Structures	91
3.11	Summary	93
4	The Relationship Between Mechanical and Dynamical Properties of Glass Forming Liquids	97
4.1	Introduction	97
4.2	Computational Details	101
4.3	Force Distributions	106
4.4	Response to Deformation	115
4.5	Force Networks	120
4.6	Discussion and Summary	122
5	Limits of a Liquid: Ideal Glass Transition and the Spinodal Line	124
5.1	Introduction	124
5.2	Prior Work	127
5.2.1	Spinodal Line	127
5.2.2	Glass Transition Line	129
5.3	Elements of Liquid State Theory	132
5.4	Treatment of the Integral Equations	137
5.4.1	Computational Details	139
5.4.2	Estimate of Switching Parameter	141
5.5	Thermodynamic Approach to Glass Transition	150
5.5.1	Replicated Free Energy for the One Component Atomic Liquid	152

5.5.2	Replicated Free Energy for Binary Mixture	156
5.5.3	Calculation of the Kauzmann Temperature	162
5.6	Phase Diagram	163
5.7	Conclusions	165
6	Onset of Breakdown of the Stokes-Einstein Relation	167
6.1	Müller-Plathe's Algorithm	168
6.2	Results and Discussions	171
6.3	Fractional Stokes-Einstein	174
6.4	Conclusions	176
	Bibliography	181

Chapter 1

Introduction

Supercooled liquids exhibit very rich physics and many observed phenomena have remained as long standing puzzles in statistical physics. In particular the problem of the glass transition has attracted a lot of attention. This thesis is devoted to understanding the properties of supercooled liquids, especially the dynamics, thermodynamics and electronic structure. I will use this chapter to briefly introduce certain important concepts and key phenomena involved in the understanding of supercooled liquids. I will introduce the phenomenology of glass formation, the relaxation and dynamics in glass forming systems, the various approaches to understanding these systems namely the energy landscape formalism and computational methods. I also briefly introduce a thermodynamic theory for the glass transition based on the replica approach.

1.1 Introduction to Supercooled Liquids

At high temperatures (*e.g.*, well above the melting temperature) the structural relaxation time, τ , of a liquid is typically of the order of a picosecond. In equilibrium, the liquid freezes to the crystalline state at the freezing temperature T_m . The structure in the crystalline phase of the system is generally the lowest energy structure the system can have. As one cools the liquid below the freezing temperature, crystal nucleation sites start to appear. These sites are energetically stable and tend to grow. The growth of these nucleation sites is dictated by the competition between the bulk and surface free energies of the crystal nucleus. If N were to be the number of atoms in a crystal nucleus, the free energy of the volume would go as $\sim N$ and free energy of the surface would go as $\sim N^{2/3}$. Therefore competition between the free energies exists only when the nuclei are small. The nucleus has a critical size beyond which it could grow irreversibly to make the entire system crystalline. If one were to cool the liquid fast enough so that critical nuclei do not form, one would be able to avoid crystallization and the liquid would exist in the supercooled state. Below the freezing temperature the relaxation time of the liquid increases dramatically. On cooling there comes a point when the relaxation time is $\tau \approx 100\text{s}$. At this point the liquid fails to relax structurally on experimental time scales and is said to have become a *glass*. The temperature at which this time scale is approached is known as the *glass transition* temperature (T_g). Once the system becomes a glass the system is not ergodic anymore.

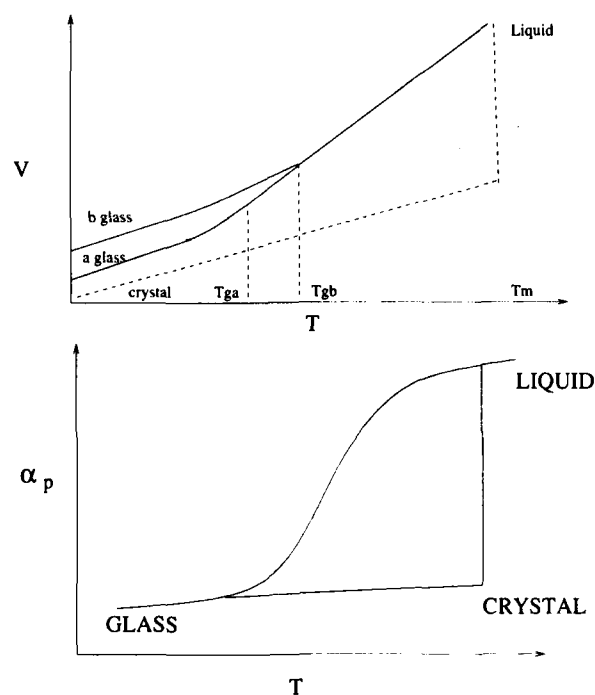


Figure 1.1: The upper panel shows the isobaric relationship between the volume and temperature in the liquid, glassy and crystalline states. The lower panel shows the coefficient of thermal expansion α_p in the liquid and glassy phase. This figure has been adapted from [34].

1.1.1 Phenomenology of Glass Formation

Consider an experiment when a liquid is cooled below its freezing temperature at constant pressure (See Fig 1.1). Above the melting temperature the expansion coefficient of the liquid (α_p) is nearly constant. As one cools the liquid further (in the supercooled phase), α_p changes rapidly. Eventually at the glass transition α_p is approximately the same as that of a crystal. α_p in the glass is lesser than that of the liquid branch. If one were to look at the volume-temperature plot one would notice a distinct change of slope

below and above the glass transition. Illustrated in Fig 1.1 is the volume-temperature plot showing two branches labeled a and b . These correspond to two different cooling rates, the cooling rate of b being higher than a . Slower the cooling rate of the supercooled liquid the longer the time it has, to equilibrate. If the cooling rate of the liquid is fast, the liquid does not have time to equilibrate on experimental time scales and would get into the glassy phase at a higher temperature than for slower cooling rates. Hence slower the cooling rate lower the glass transition temperature. In Fig 1.1 one would notice that $T_{ga} < T_{gb}$. If one were to look at the enthalpy changes across the glass transition (See Fig 1.2), the behaviour is similar to volume. The isobaric derivative of the enthalpy, the specific heat C_p , changes very steeply around T_g . The fact that the enthalpy changes continuously would mean that no latent heat effects are involved during this transition.

1.1.2 Temperature Dependence of Viscosity

Structural parameters such as the structure factor or the pair correlation function of the supercooled show moderate dependence on temperature below the freezing temperature [66]. Unlike structural parameters, dynamical parameters are very sensitive to temperature. Consider the case of a dynamical quantity like the viscosity (η). Relatively small change in temperature by a factor of 3 brings about 12-14 decades of change in η . Therefore it is convenient sometimes to use an alternate definition of the glass transition temperature, T_g as the temperature at which $\eta(T) = 10^{12}$ Pas or 10^{13} Poise (1 Poise = 0.1 Pas). Angell [3] has used the temperature dependence

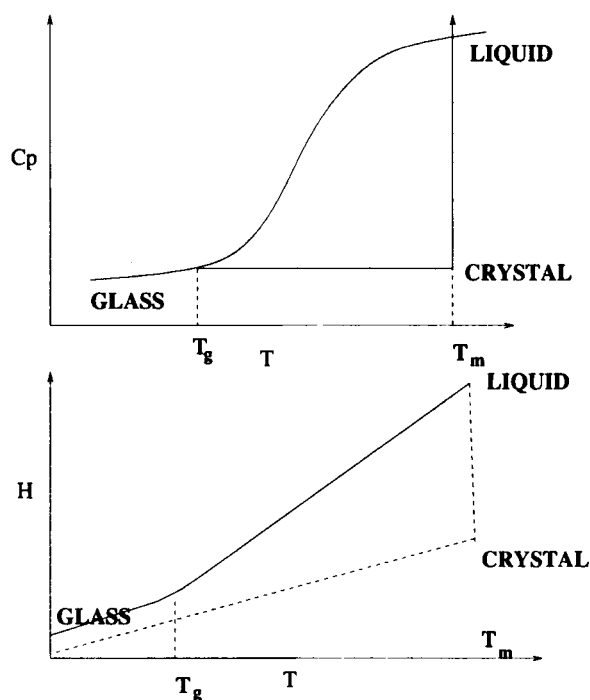


Figure 1.2: The upper panel shows the behaviour of specific heat in the glassy and liquid phase. Lower panel shows isobaric relationship between the enthalpy and temperature in the liquid, glassy and crystalline states. This fig has been adapted from [34].

of $\eta(T)$ to classify supercooled liquids. A liquid is called *strong* if the temperature dependence of $\eta(T)$ for the liquid approximates the Arrhenius law $\eta(T) = \eta_0 \exp(\frac{E}{k_B T})$ well, where E is the activation energy. Examples of such liquids are networked oxides such as SiO_2 , GeO_2 etc. The plot of $\log(\eta)$ vs T would be a straight line as illustrated in Fig.1.3 in the case of strong liquids. In contrast to this we have systems such as o-terphenyl, toluene and chlorobenzene where $\log(\eta)$ vs T show pronounced curvature around $T_g/T \approx 0.7$ are classified as *fragile*. Strong liquids are in general characterized by open networks (SiO_2) whereas fragile liquids constitute more compact local

arrangement of particles.

We can get a good representation of liquids with varying degrees of fragility by plotting T_g/T vs $\log(\eta)$ known as the *Angell plot* (See Fig 1.3).

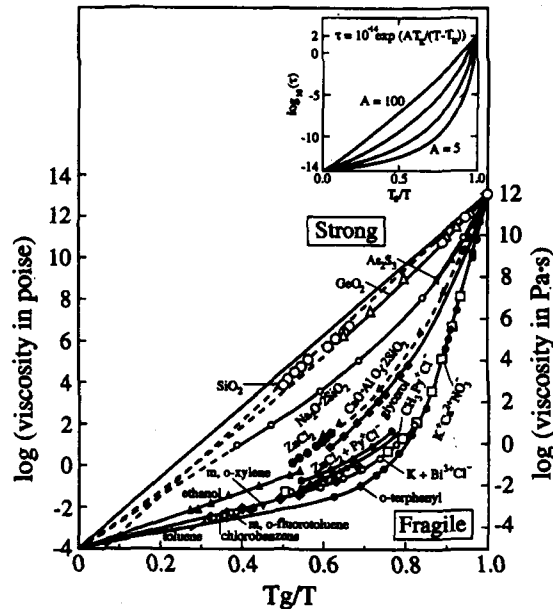


Figure 1.3: Angell Plot characterizes a liquid based on how much its viscosity deviates from the Arrhenius behaviour. $\log(\eta)$ vs T_g/T is plotted for various liquids. Liquids which exhibit Arrhenius behaviour are known as strong liquids and those that show deviation are known as fragile. This figure is from [3].

Illustrated in Fig 1.4 are the various regimes of viscosity important for glass makers. An η of 10^{-3} Pas is the typical viscosity of a liquid like water at room temperature. Generally the pouring interval is between $10^1 - 10^3$ Pas. The onset of glass forming or working interval is $10^5 - 10^8$ Pas. Vitrification or glass formation is characterized by the point when η is 10^{12} Pas.

An ansatz which fits $\eta(T)$ well at low and intermediate temperatures is

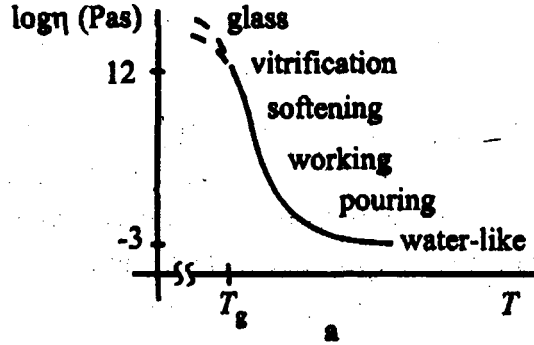


Figure 1.4: A schematic picture of the viscosity variation over a range of temperatures up to the the glass transition temperature. This figure is from [39].

the Vogel-Fulcher-Tammann (VFT) [44, 120, 130] equation.

$$\eta(T) = \eta_0 \exp \left[\frac{A}{T - T_0} \right] \quad (1.1)$$

T_0 is called as the “*Vogel temperature*”, the Arrhenius law is a special case of the VFT equation with $T_0 = 0$. This is a very useful parameterization, but it is known not to hold exactly in experiments [34]. η in the range 0.1 Poise to 100 Poise can be fit well with the power law behaviour.

$$\eta(T) = \eta_0 (T - T_c)^{-\gamma} \quad (1.2)$$

This law is predicted by a dynamic theory known as the “*Mode coupling theory*” (MCT). T_c here is called the critical temperature, also known as the mode coupling temperature, where dynamical arrest takes place in this theory. The mode coupling temperature predicted is 20-30% higher than the laboratory glass transition temperature T_g [66].

1.1.3 Relaxation in the Supercooled Regime

Correlation functions are very useful tools to probe dynamics of supercooled liquids. Transport quantities such as viscosity and diffusion can be written as integrals over microscopic correlators [19]. In experiments such as dynamic light scattering one has direct access to such correlation functions. Typical correlation functions are the coherent intermediate scattering $F(\mathbf{q}, t)$ and the incoherent intermediate scattering function $F_s(\mathbf{q}, t)$. The magnitude of the wave vector \mathbf{q} are inversely related to the length scale of the dynamics. These correlation function are functions of the wave vector \mathbf{q} and time t . If one chooses to study dynamics at short length scales one calculates the correlation at large momenta and *vice versa*. These correlation functions are defined as follows

$$F(\mathbf{q}, t) = \frac{1}{N} \sum_{\mathbf{k}=1}^N \sum_{j=1}^N \langle \exp[i\mathbf{q} \cdot (\mathbf{r}_j(t) - \mathbf{r}_k(0))] \rangle \quad (1.3)$$

$$F_s(\mathbf{q}, t) = \frac{1}{N} \sum_{j=1}^N \langle \exp[i\mathbf{q} \cdot (\mathbf{r}_j(t) - \mathbf{r}_j(0))] \rangle \quad (1.4)$$

Illustrated in Fig 1.5 is the behaviour of a typical density-density correlation function $F(\mathbf{q}, t)$ for a liquid at high temperature and in the supercooled regime. At very short times the motion of particles is ballistic for both high and low temperatures and the correlation function depends on t as t^2 . This regime is known as the ballistic regime. Beyond this regime the high temperature liquid shows a Debye relaxation (exponential relaxation) but the situation with the low T liquid is much more complex. Beyond the ballistic regime the particles of the low T liquid experience the presence of neighboring atoms and the correlation function enters a plateau known as the β

relaxation regime (in the MCT terminology). It is only much later in time that the correlation function decays further, and this is known as the α -relaxation regime. The presence of the plateau is often explained by the so called *caging effect*. A temporary cage is formed by particles surrounding the moving particle and it is unable to diffuse out for some time.

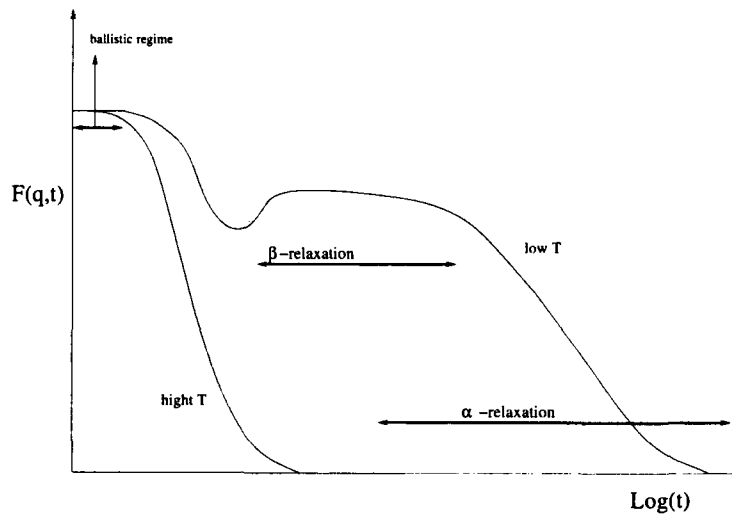


Figure 1.5: Illustrated in the figure are the various relaxation regimes for a typical correlation function like the self scattering function. The high temperature liquid exhibits Debye relaxation. The low temperature exhibits a two step relaxation process, namely the α and β relaxation shown. This figure has been adapted from [66].

Fig 1.6 illustrates the β relaxation regime when the system is stuck inside a temporary cage and Fig 1.7 illustrates particle escaping from the temporary cage and entering the α relaxation regime.

The decay in the case of slowly relaxing liquid follows the so called Kohlraush-Williams-Watts (KWW) function, also known as the stretched exponential function,

$$\Phi(t) = A \exp[-(t/\tau)^\beta] \quad (1.5)$$

where A is the amplitude, τ is the relaxation time and β is the KWW exponent, $\beta \leq 1$. Two scenarios have been proposed to understand non-Debye relaxation in the supercooled regime: (i) it is the cumulative effect of several Debye relaxation centers having different relaxation times, (ii) individual centers of relaxation have non Debye relaxation, but have the same relaxation time. Which of these scenarios holds is a subject of ongoing research.

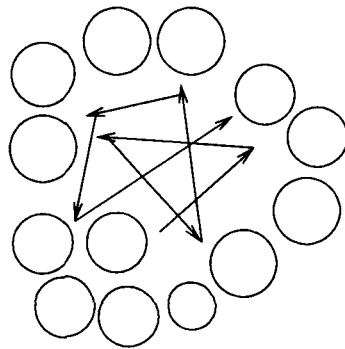


Figure 1.6: Particle motion confined to temporary cage, central particle is yet to escape.

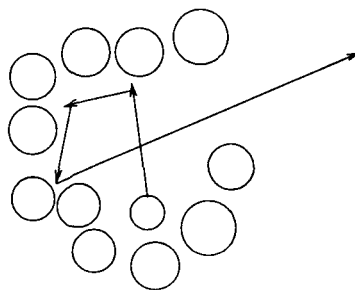


Figure 1.7: Particle escaping out of the temporary cage to go into diffusive motion.

1.2 Energy Landscape in Supercooled Liquids

The Energy landscape approach has been a very important method in the study of liquids and approach to glass formation. The energy landscape of a system is described by the potential energy $\Phi(\mathbf{r}_1, \mathbf{r}_2, \dots, \mathbf{r}_N)$ which depends on $3N$ coordinates of particles having positions $\mathbf{r}_1 \dots \mathbf{r}_N$. The energy surface described is in a $3N+1$ dimensional space defined by $3N$ particle coordinates and one energy coordinate. The local minima on this surface are the mechanically stable structures of the system (since the net force on each particle is zero). These minima are known as *inherent structures*. The global minimum is possibly the crystalline phase. Stillinger and Weber in their seminal papers [115, 117, 118] discuss how the dynamics of a liquid at a temperature could be mapped to the dynamics of how the system explore the inherent structures in the landscape. The idea is that, the liquid configurations are uniquely mapped to the closest local minimum to the configuration on the energy hyper-surface. This kind of configurational mapping separates the mechanically stable and the vibrational part of the configuration. The local minimum to which an instantaneous configuration is mapped can be reached in principle via the steepest descent route (to be discussed in section 1.44). The points on the boundaries which separate distinct quenched regions cannot be mapped uniquely to a local minimum. Nevertheless, the dimension of the such boundary regions is a dimension lower than the hyper-surface dimension. Hence in the limit of large dimensionality of the hyper-surface, such points become relatively negligible and the mapping is justified. Such a map is very advantageous as we will later see.

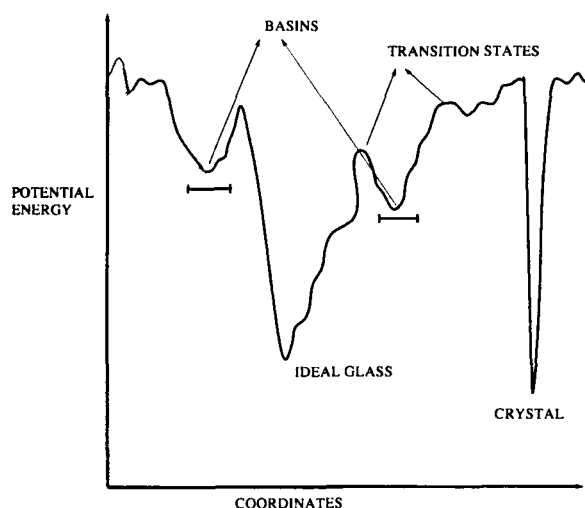


Figure 1.8: A qualitative sketch of the energy landscape shown for simplicity in one dimension. Adapted from [34].

Figure 1.8 is a qualitative sketch of the complex $3N$ dimensional surface, showing potential energy as a function of coordinates, which shows the crystalline phase and the ideal glass phase as deep energy minima. Also illustrated are basins of attraction to inherent structures and transition points on the surface. The system explores different parts of the landscape at different temperatures. At high temperatures the system dynamics is quite independent of the topography of the landscape and corresponds to free diffusion of the liquid. Fig 1.9 illustrates the inherent structure energy per particle for the case of a model glass former known as the Kob-Andersen binary Lennard Jones mixture (KABMLJ) [67] studied extensively in computer simulations. For this system with density $\rho = 1.2$, at reduced temperatures higher than $T=1$, there is free diffusion. The relaxation above this temperature is exponential. Deep minima are rare in this regime.

Below $T=1$, slow dynamics sets in [104]; this temperature is known as

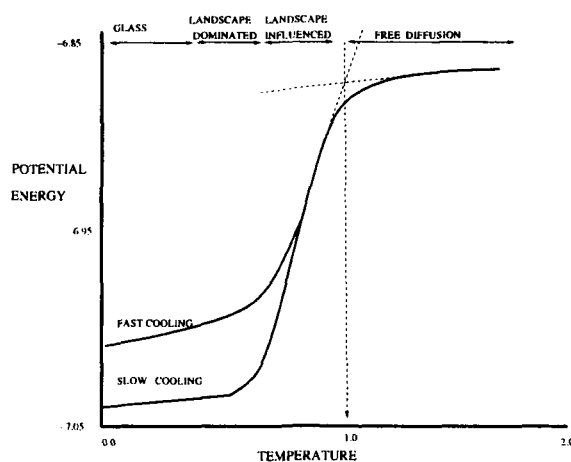


Figure 1.9: A schematic of the inherent structure potential energy per particle as a function of the temperature. Behavior of the inherent structure energy in various regimes are indicated. This has been calculated for the KABMLJ liquid at for density 1.2. The figure has been adapted from [104].

the *onset of slow dynamics temperature* (T_s). Below the onset temperature the system shows stretched exponential relaxation behaviour. From here on the system dynamics is landscape influenced. As illustrated in Fig 1.9 one would notice that below this temperature the system explores deeper parts of the energy landscape.

As we lower the temperature of the KABMLJ liquid to around $T \approx 0.45$, the liquid starts to explore deeper regions in the landscape and samples only distinct potential energy minima and vibrations within the minima. This temperature corresponds closely to the temperature at which the mode coupling theory predicts the glass transition. This temperature is known as the *mode coupling temperature* (T_{MCT}). Mode coupling theory is a dynamical theory, it fails to describe thermal hopping between inherent structures. In order to investigate the energy landscape explored by the system below

T_{MCT} , Angelani *et al.*, [2] and Broderix *et al.*, [24] mapped the instantaneous configurations of the liquid to its closest saddle points on the energy landscape. They found that the number of unstable modes of the saddle point become zero as we approach the T_{MCT} from above. They thus show that the landscape sampled above the T_{MCT} is saddle point dominated and below as minima dominated. It was shown earlier by Schroeder *et al.* [108] that below T_{MCT} one can almost separate the dynamics into vibration within the inherent structures and hopping between the inherent structures. In order to show this, the intermediate self scattering function for the actual dynamics ($F_s(\mathbf{q}, t)$) and the inherent structure dynamics ($F_s^I(\mathbf{q}, t)$) was calculated. The use of the superscript “I” is to denote inherent structure from now on.

$$F_s(\mathbf{q}, t) = \langle \cos(\mathbf{q} \cdot (\mathbf{r}_j(t) - \mathbf{r}_j(0))) \rangle \quad (1.6)$$

$$F_s^I(\mathbf{q}, t) = \langle \cos(\mathbf{q} \cdot (\mathbf{r}_j^I(t) - \mathbf{r}_j^I(0))) \rangle \quad (1.7)$$

The inherent structure dynamics is created by quenching the instantaneous configurations. From the Fig. 1.10 one can see that the plateau disappears in the case of $F_s^I(\mathbf{q}, t)$. Both the $F_s(\mathbf{q}, t)$ and $F_s^I(\mathbf{q}, t)$ are well described by the stretched exponential $f(t) = f_c \exp[-(\frac{t}{\tau})^\beta]$ in the long time regime. This provides us a way to quantitatively compare the long time behaviour of $F_s(\mathbf{q}, t)$ and $F_s^I(\mathbf{q}, t)$ by comparing the fitting parameters τ, β, f_c . If one can indeed separate the dynamics into vibrations within the inherent structures and hopping between the inherent structures one should expect this to be reflected in the relation between τ^I, β^I, f_c^I and τ, β, f_c . If one assumes

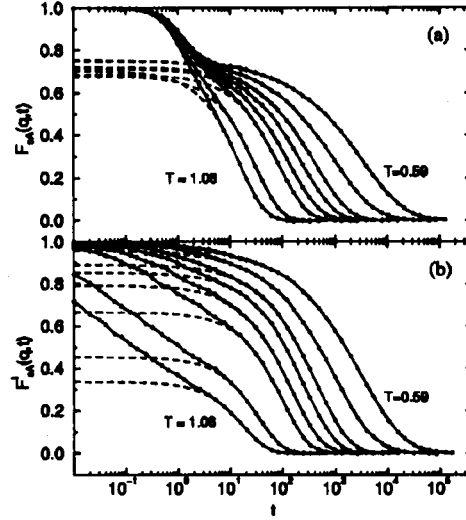


Figure 1.10: Illustrated here is the (a) $F_s(\mathbf{q} = 7.5, t)$ and (b) $F_s^I(\mathbf{q} = 7.5, t)$. Dashed lines are fit to the stretched exponential $f(t) = f_c \exp[-(\frac{t}{\tau})^\beta]$. Taken from [108].

such separation of dynamics, then the quenching should remove the initial vibrational relaxation, i.e., $F_s^I(\mathbf{q}, t)$ can be thought of as $F_s(\mathbf{q}, t)$ with the initial relaxation removed. Instead of using the *cosine* formula if we use the exponential in Eq. 1.6-1.7 and write the displacement as $\delta x = \delta x_{vib} + \delta x_{inh}$. If δx_{vib} and δx_{inh} are statistically independent, the self scattering function becomes a product of terms involving transition between inherent states and vibrations with the inherent state (which vanishes in the long time limit). At long times the vibrational part becomes time independent and converges to the nonergodicity parameter (f_c). This implies that $F_s^I(\mathbf{q}, t)$ is the same as $F_s(\mathbf{q}, t)$ for long times but rescaled to start at unity, $(\tau^I, \beta^I, f_c^I) = (\tau, \beta, 1)$. Illustrated in Fig 1.11 are the fitting parameters to the stretched exponential discussed for both the inherent and the real dynamics. Notice that the relaxation times and the stretching parameters at low temperatures for the

inherent structures and the real dynamics are the same. This confirms that at low temperatures inherent structure dynamics is a coarse grained version of the real dynamics. The interesting thing to note is the nonergodicity parameters, at the lowest T , f_c^I goes to unity, whereas f_c is roughly independent of T .

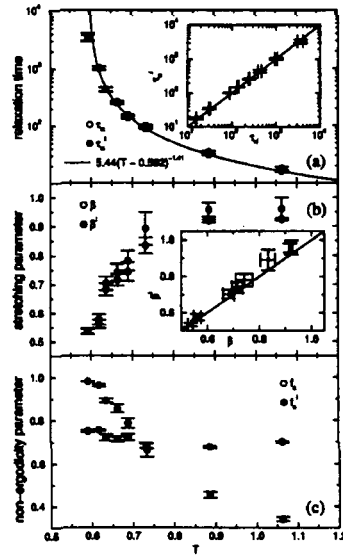


Figure 1.11: Fitting parameters describing fit of $F_s^I(\mathbf{q} = 7.5, t)$ and $F_s(\mathbf{q} = 7.5, t)$ to the stretched exponential. (a) Relaxation times τ^I and τ vs T . The solid line shows a power law fit. (b) The stretching parameters β^I and β vs T . (c) The Nonergodicity parameters f_c and f_c^I vs T . Taken from [108].

The dynamics in this temperature ($T \sim 0.45$) regime is dominated by the topography of the landscape and not simply influenced. On cooling further the system gets stuck in a single minimum. The depth of the minima is deeper if the cooling is slower.

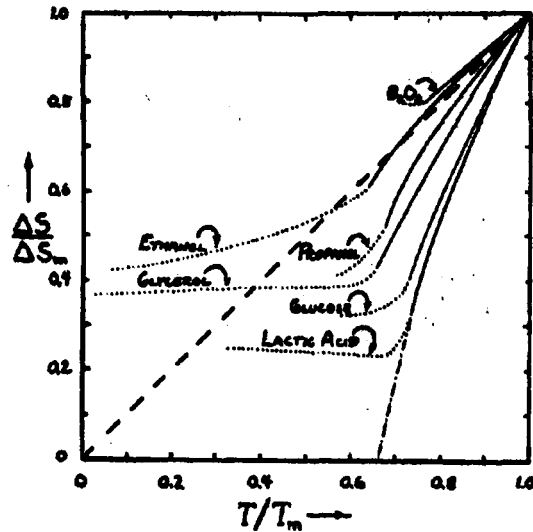


Figure 1.12: The original plot of Kauzmann is presented here. The y-axis is the ratio of the entropy difference between the liquid and the crystal at a certain temperature with respect to the same quantity at the melting temperature. The x-axis is the ratio of the temperature and the melting temperature. The behaviour for various liquids are shown. We would notice that there are certain liquids which lose entropy quickly and exhibit features predicting a finite temperature ideal glass transition. From [63].

1.3 The Kauzmann Paradox

We generally expect the supercooled liquid to be more disordered than the corresponding crystal. Thus the liquid entropy S_{liq} is larger than the crystal entropy S_{crys} . Kauzmann noted that the difference $\Delta S = S_{liq} - S_{crys}$ is an increasing function of temperature. We call ΔS the excess entropy. Kauzmann originally considered six liquids below their melting temperatures (See Fig 1.12). These liquids have different fragility. Fig 1.12 illustrates the behaviour of $\frac{\Delta S}{\Delta S_m}$ vs $\frac{T}{T_m}$, here ΔS_m is the excess entropy at the melting temperature (T_m). We would notice that if we extrapolate the behaviour of B_2O_3 we

would find that its ΔS vanishes somewhere close to 0 K. The interesting feature for lactic acid is that if we were to extrapolate its ΔS , it vanishes at around $2/3 T_m$. In experiment one is not able to go so low in temperature since the glass transition intervenes. In computer simulations again one is not able to equilibrate the liquid, because of the large relaxation times one encounters at these temperatures, hence the exact nature of what happens is yet unresolved. If we were to continue cooling the liquid very slowly, there arises a possibility that the entropy of the liquid becomes lower than the entropy of the corresponding solid. Though this feature would seem unphysical, it does not violate any law of thermodynamics. If one were to continue the cooling towards zero Kelvin, one encounters a situation where, liquid entropy becomes negative, which is inconsistent with thermodynamics. This scenario is known as the *Kauzmann paradox*. If a glass transition were to intervene at the temperature when $\Delta S = 0$, the glass obtained is known as an *ideal glass*. The temperature at which $\Delta S = 0$, is known as the *Kauzmann temperature* (T_K).

1.4 Thermodynamic Approach to Glass Transition

The transition from the liquid to the glassy phase can be understood in the framework of the Gibbs-Dimarzio scenario [45]. Briefly one could think of it in the following manner. At low temperatures the system is trapped for long times in one of the exponentially large number of local energy minima

in the energy landscape. The dynamics in this region is very slow as it involves hopping between these local energy minima. The entropy of such a system has two contributions (i) logarithm of the number of accessible local energy minima, known as the *configurational entropy* S_c (ii) vibrational entropy within the local energy minima. As one lowers the temperature; the configurational entropy $S_c(T) \rightarrow 0$ *i.e.*, the number of relevant minima at a temperature T becomes lesser than an exponential in N ; leading to a thermodynamic transition. This understanding of glass transition is captured based on coupled replicated glassy system [42,76,80], leading to a formulation of a first principles computational scheme which provides a description of equilibrium thermodynamics of glasses. We will briefly summarize here the basic idea of the scheme. The energy landscape of a supercooled liquid can be decomposed into regions which are mapped to the closest local energy minima (inherent structures). The dynamics of the supercooled liquid, itself can be mapped to the dynamics of the inherent structure exploration of the system *i.e.*, the trajectories of the supercooled liquid can be mapped to a trajectory exploring just the inherent structure visited in the region. The partition function can thus be represented as a sum over the inherent structure states in the following manner

$$Z = \sum_i \exp\left(\frac{-\beta N f_i}{T}\right) \quad (1.8)$$

here f_i represent the free energies per particle of inherent structures in the configurational space. The density of states of the inherent structure energy is given by $\Omega(f_i, T)$ and is proportional to $\exp[NS_c(f_i, T)]$, S_c is known as the

configurational entropy density or *complexity*. Let us assume the following form for the complexity (See Fig 1.13). The range of f where this model for the configurational entropy is valid is temperature dependent.

$$\begin{aligned} S_c(f) &= 0, f < f_{min} \\ S_c(f) &= \text{concave function}, f > f_{min} \end{aligned} \quad (1.9)$$

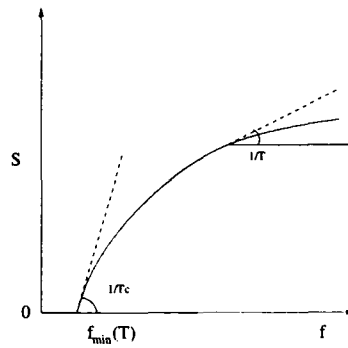


Figure 1.13: A schematic of the configurational entropy vs the free energy across the ideal glass transition temperature.

We can thus write the approximate partition function in the following manner.

$$Z \approx \int_{f > f_{min}} df \exp[-N\beta(f - TS_c)] \quad (1.10)$$

In the thermodynamic limit one gets the free energy for temperatures

greater than T_c to be

$$F(T) = f^*(T) - TS_c(f^*(T), T) \quad (1.11)$$

where $1/T_c$ is the maximal slope of the function $S_c(f)$. $f^*(T)$ is defined through the relation $(\frac{\partial S_c}{\partial f})_{f^*} = 1/T < 1/T_c$. Below T_c the free energy would be stuck to f_{min} . Mezard and Parisi's method involves capturing the above phenomenology using replicas of a system of liquids having the same temperature and particle numbers. Assume we have m replicas coupled together with an attractive potential which makes the particles positions remains correlated among the different replicas. The attractive term is then switched to zero. The partition function of the m replica system is given by

$$Z_m \approx \int_{f > f_{min}} df \exp[-Nm(f - (T/m)S(f, T))/T] \quad (1.12)$$

The important point to note here is that the phase space volume $\Omega(f)$ remains the same as the non replicated liquid since the atoms in different replicas are assumed to remain in the same basin hence no m in front of $TS(f, T)$. The free energy with an effective temperature T/m in the thermodynamic limit is given by

$$\begin{aligned} F(m, T) &= f^*(m, T) - \frac{T}{m} S(f, T), \quad T > mT_c \\ F(m, T) &= f_{min}, \quad T < mT_c \end{aligned} \quad (1.13)$$

here $f^*(m, T)$ is defined via the equation

$$\left(\frac{\partial S(f, T)}{\partial f} \right)_{f^*} = \frac{m}{T} < \beta_c \quad (1.14)$$

Let us define $m_*(T) = T/T_c$. For any temperature $T < T_c$, there exists a value $m_* < 1$ such that $m < m_*$. At T_c we would have $m_*(T_c) = 1$. Once the free energy is defined as a function of m and T , one analytically continues m to non integer values, especially to values smaller than 1. When m approaches m_* from below and if m_* is less than 1, the system is stuck with a free energy f_{min} . The system is defined to be in the glassy phase. If $m_* > 1$ then the system is in the liquid phase. This allows us to determine the Kauzmann temperature to be the temperature through the relation $m_*(T) = 1$. In principle one could calculate the derivatives of the free energy $F(m, T)$ with respect to m at $m = m_*(T)$ and it is identical to zero, and the second derivative of the free energy with respect to m is negative (due to the choice of the specific shape of the $S(f, T)$). We thus conclude that $F(m, T)$ exhibits a maxima at m_* (See Fig 1.14). The free energy as a function of temperature is illustrated in Fig 1.15.

In short the following is the procedure one uses to calculate the Kauzmann temperature.

1. Calculate the free energy for the replicated system, number of replicas being m .
2. Analytically continue the function to non integer values of m .
3. Maximize the free energy $F(m, T)$ in the interval $[0, 1]$.

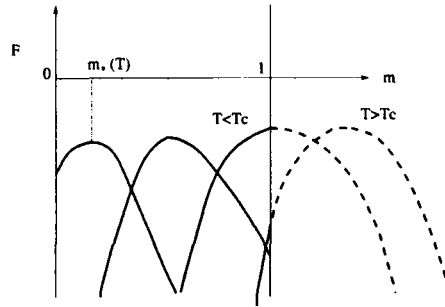


Figure 1.14: Behaviour of the free energy vs m , above and below the the transition.

4. if $m_* < 1$, then $T < T_c$ and we are in the glass phase.
5. if $m_* > 1$, then $T > T_c$, and we are in the liquid phase.
6. The relation $m_*(T) = 1$ determines the transition temperature.

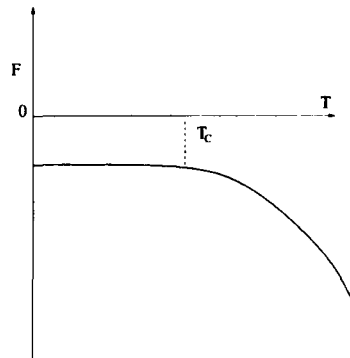


Figure 1.15: Free energy vs temperature.

We will discuss further in chapter 5 how one calculates the partition function of the liquid close to the ideal glass transition temperature. We calculate in that chapter, the ideal glass transition temperature for the Kob-Andersen model [67] using certain closure approximations from liquid state theory.

1.5 Computer Simulations in Glass Forming Liquids

Computer simulation is one of the most important tools in the investigation of glass forming liquids. It gives one access to many aspects of a glass forming liquid which are out of the reach of experiments or theoretical calculations. In this section we discuss some aspects of computer simulation namely molecular dynamics (based on [43, 129]), Monte Carlo and energy minimization.

1.5.1 Molecular Dynamics

Molecular dynamics (MD) is a computer simulation technique where the time evolution of a set of interacting atoms is followed by integrating their equations of motion. We discuss here only classical molecular dynamics, wherein the forces are calculated via Newton's laws (Eq 1.15) in contrast quantum methods, which use the Feynman-Hellmann theorem [75].

$$F_i = m_i a_i \quad (1.15)$$

F_i is the force acting on particle i with mass m_i due to all the other interacting atoms and acceleration $a_i = \frac{d^2 r_i}{dt^2}$. MD is a deterministic method unlike the *Monte Carlo* method. If one knows the initial conditions, the system (in principle) evolves according to the set of deterministic equations. Though at the level of atoms the origin of the forces are quantum, we still use classical forces. The validity of classical approximation can be assessed in terms of the de Broglie wavelength (λ). Here M is the mass and T is the

temperature.

$$\lambda = \sqrt{\frac{2\pi\hbar^2}{Mk_B T}} \quad (1.16)$$

The classical approximation is justified when $\lambda \ll l$, where l is the mean nearest neighbor distance. A liquid near its triple point has $\lambda/l \approx 0.1$. The classical approximation would be bad for systems with low mass such as H_2 , He etc. At low temperatures quantum effects become important. Molecular dynamics should be treated with caution in these regions. The most important aspect is to model the system which amounts to choosing a potential $V(r_1, r_2, \dots, r_N)$, where r_1, \dots, r_N are the position coordinates of the nuclei. The forces can then be calculated as the derivative with respect to the atomic coordinates. A simple choice of V is a sum of pairwise interactions of the atoms. There are more involved forms of the potentials that are in common use which involve the three body term. One such potential will be discussed for the case of silicon later in the thesis. Development of potentials is an important aspect of the molecular dynamics.

In the study of glass forming liquids, one tends to face the problem of crystallization while performing molecular dynamics below the melting temperature of many model liquids with potentials such as the Lennard-Jones which is a good potential for liquid Argon. With such systems it becomes very difficult to take the system to the supercooled state below the melting temperature due to crystallization. Such problems are circumvented by choosing potentials which do not easily allow formation of the crystalline state. One such potential is given by Kob and Andersen [67]. This system is popularly known as the Kob-Andersen binary mixture. This is a mixture

of two kinds of atoms A and B in the ratio 80:20 which interact via the Lennard-Jones potential

$$V^{\alpha\beta}(r) = 4\epsilon_{\alpha\beta} \left[\left(\frac{\sigma_{\alpha\beta}}{r} \right)^{12} - \left(\frac{\sigma_{\alpha\beta}}{r} \right)^6 \right]$$

$$\alpha, \beta \in \{A, B\} \quad (1.17)$$

The parameters $\sigma_{AB}/\sigma_{AA} = 0.8$, $\sigma_{BB}/\sigma_{AA} = 0.88$, $\epsilon_{AB}/\epsilon_{AA} = 1.5$, $\epsilon_{BB}/\epsilon_{AA} = 0.5$, the masses of both particles are the same.

In order to evolve the system in time, one needs to integrate the equations of motion. One well-known algorithm to do this is the velocity Verlet algorithm [43].

$$\mathbf{r}_i(t+h) = \mathbf{r}_i(t) + h\mathbf{v}_i(t) + \frac{h^2}{2} \frac{\mathbf{F}_i(t)}{m_i}$$

$$\mathbf{v}_i(t+h) = \mathbf{v}_i(t) + \frac{h}{2} \left[\mathbf{F}_i(t) + \frac{\mathbf{F}_i(t+h)}{m_i} \right] \quad (1.18)$$

\mathbf{r}_i , \mathbf{v}_i and \mathbf{F}_i are the position, velocity and the force on the i^{th} particle, and h is the time step for typical liquids which is of the order of a few femto seconds. This kind of integration conserves energy and is also known as constant energy molecular dynamics. We could also do molecular dynamics simulation for constant temperature and constant pressure. We first deal with constant temperature MD. To do constant temperature molecular dynamics one couples the system with a thermal bath. Particles randomly collide with imaginary heat bath particles. The particles instantaneously change momentum. The particle velocities are reset to new values taken from a

Maxwell distribution. This way the average kinetic energy and hence the temperature is kept a constant. Early algorithms for constant temperature MD used to scale velocities after every few hundred MD steps such that the kinetic energy is kept a constant. This sort of method is crude and cannot be shown to correspond to a canonical ensemble. A method which does rescaling but reproduces to a canonical ensemble is the Nose-Hoover thermostat [43,129]. The idea is to introduce an additional degree of freedom η describing an external bath and the corresponding temperature $\chi = \partial\eta/\partial t$. the potential energy is then $Q\chi^2/2$ and the kinetic energy $\eta \sum_{i=1,N} p_i^2/2m - 3/2K_B T_o$. We then obtain the equation of motion as

$$\begin{aligned}\frac{d\mathbf{r}}{dt} &= \frac{\mathbf{p}_i}{m_i} \\ \frac{d\mathbf{p}}{dt} &= \mathbf{F}_i - \chi\mathbf{p}_i \\ \frac{d\chi}{dt} &= \frac{f}{Q} \left(\frac{1}{f} \sum_i \frac{p_i^2}{2m} - k_B T_o \right)\end{aligned}\tag{1.19}$$

f here is the total number of degrees of freedom. We can show by direct substitution that the canonical distribution is obtained.

$$\rho \sim \exp \left[-\beta \left(\sum_{i=1,N} \frac{p_i^2}{2m} + U(q_1 \dots q_N) \right) \right]\tag{1.20}$$

Where $q_1 \dots q_N$ are the position coordinates of the system.

The constant pressure scenario is realized by having an imaginary piston of mass M which under constant force reproduces a constant pressure P_o .

An additional kinetic energy $(\frac{1}{2})M\dot{V}$ and potential energy P_oV are added to the Hamiltonian for the constant pressure and constant enthalpy ensemble (NPH), V is the volume in this case which is allowed to fluctuate. We then define rescaled variables

$$\begin{aligned} r_i &= V^{1/3} s_i \\ \dot{r}_i &= V^{1/3} \dot{s}_i \end{aligned} \quad (1.21)$$

We thus obtain through the Hamiltonian equation of motion that

$$\begin{aligned} \ddot{s}_i &= \frac{\mathbf{F}_i}{m_i V^{1/3}} - (2/3)\dot{s}_i(\dot{V}/v) \\ \ddot{V} &= \frac{(P - P_o)}{M} \end{aligned} \quad (1.22)$$

$$(1.23)$$

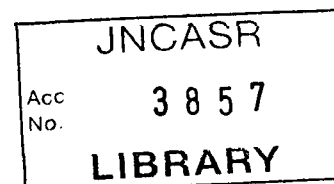
We could couple the method with Nose-Hoover thermostat discussed earlier by introducing the variable η and $\chi = \partial\eta/\partial t$. This would give us a constant pressure and constant temperature ensemble (NPT). The NPT molecular dynamics equations are thus:

$$\begin{aligned}
 \dot{s}_i &= \frac{\dot{\mathbf{p}}}{mV^{1/3}} \\
 \dot{\mathbf{p}}_i &= \mathbf{F}_i - (\chi + \omega)\mathbf{p}_i \\
 \dot{\chi} &= \frac{f}{Q} \left(\frac{1}{f} \sum_{i=1, N} \frac{\mathbf{p}_i^2}{2m} - k_B T_o \right) \\
 \omega &= \frac{\dot{V}}{V} \\
 \dot{\omega} &= \frac{(P - P_o)V}{\tau^2 k_B T}
 \end{aligned}
 \tag{1.24}$$

Additionally one requires the volume to be a variable in NPT simulation. The parameter ω is introduced to allow for volume fluctuation in the system, in order to maintain constant pressure. Parameter τ describes the characteristic time for volume relaxation.

Glass forming liquids when cooled the relaxation time increases by 12-15 decades in time. If one is to investigate the mechanism in these systems using molecular dynamics one needs to propagate the system for the same interval of time. As mentioned the time steps in molecular dynamics of liquids is of the order of a few femto seconds, the time involved to propagate a system to one second would be 10^{15} time steps. This is an impossibility with the computers we have today. With the present computational facilities one could relax a system to at most a few microseconds. This becomes the biggest problem of using molecular dynamics for studying systems having slow dynamics. However, with MD one is able to directly calculate the dynamics of such systems. This is the main reason, despite the drawback discussed, that MD

536.7
POL



is used extensively in the study of glass forming liquids.

1.5.2 Monte Carlo

A stochastic method in contrast to a deterministic method like the MD to study time evolution of a system is the Monte Carlo simulation. In the heart of this kind of simulation is the law of detailed balance. The transition probability from a state s to a state s' given by $w(s \rightarrow s')$ fulfill the relation $w(s \rightarrow s')/w(s' \rightarrow s) = \exp[-\beta(H(s) - H(s'))]$, where $\beta = 1/k_B T$ and $H(s)$ is the value of the Hamiltonian when the state of the system is s . Even this sort of a scheme does not allow for equilibration at low temperatures for realistic models. There have been recent Monte Carlo algorithms for hard sphere systems (which are athermal) which claim to take the system successfully above the glass transition density [99]. Analogous algorithms have been developed for short range potentials [71] but they are yet to be tested for temperatures close to the glass transition temperature.

1.5.3 Ewald Sum

For systems having long range interactions one cannot truncate the potential in a molecular dynamics simulation. If our system size is N ; computing all pair interactions is $\sim N(N - 1)$ operation. Computational effort for large system sizes would scale as $\sim N^2$. The BKS model [128] of silica that we use (later in the thesis) has a Coulomb term, which is a long ranged potential. In this section we discuss a procedure; the *Ewald Sum*, which improves the efficiency and scales computation to a $\sim N^{3/2}$ operation. Other methods exist,

depending on the system size in order to make the computation efficient. For very large system sizes ($N \approx 10^5$) methods such as PPPM (Eastwood and Hockney [40]) scales as $\sim O(N \log N)$, Fast multipole method of Greenhard-Rockhlin [50] scales as $O(N)$. Intermediate sizes ($N \approx 10^3$), which we use; the Ewald Sum is preferred. In order to describe the procedure of the Ewald sum, we study Coulomb potential as model long range potential. We briefly summarize the method in this section.

The main idea is to represent the point coulomb charges as; point charges + smeared gaussian charge distribution of the opposite charge + compensating gaussian charge distribution of the same sign as the point charges (Fig 1.16). We calculate the total interaction energy as follows: (i) Calculate the potential at the location of a point charge due to the compensating charge distribution. This is done in Fourier space. From this the interaction energy is calculated straightforwardly. (ii) The simplest way to do (i) is to treat *all* the compensating charge distributions, including the one corresponding to the point charge for which we calculate the potential. This leads to an extra self energy term that must be subtracted. (iii) Calculate the interaction energy for units made up of point charge + smeared charge distribution of opposite sign. These interactions will be short ranged. The calculation is done in real space. The sum of these three terms gives us the total energy. By appropriate choice of the width of the Gaussian distributions, both the Fourier and real space parts can be handled by sums over a finite (small) number of Fourier components, and a reasonable real space cutoff, respectively.

Using the basic idea described, we proceed in the following manner. Central problem is to compute the energy due to charge distribution $\rho(r)$. In

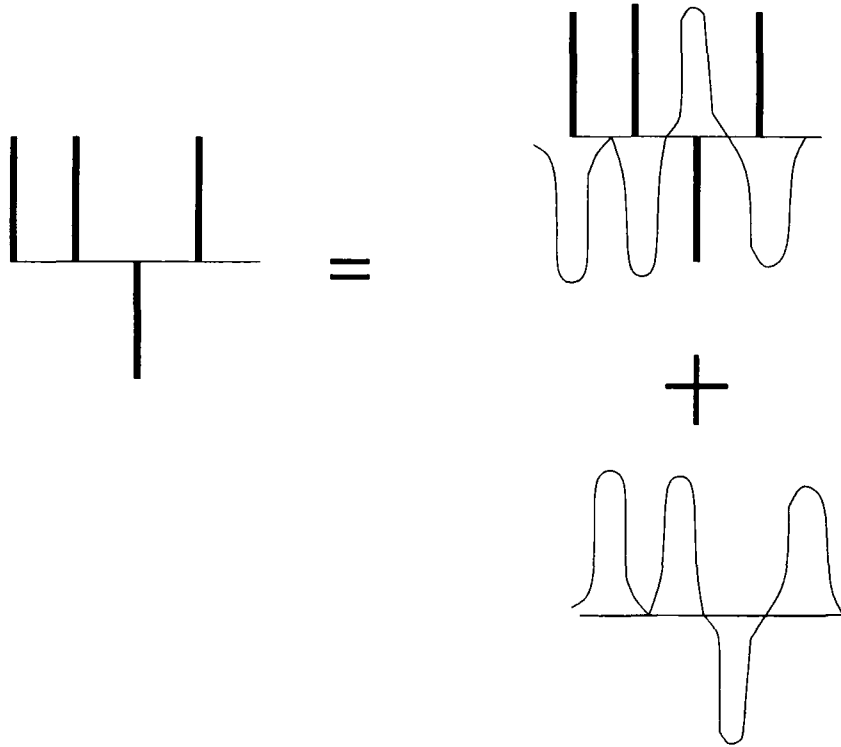


Figure 1.16: Schematic of the Ewald method, Showing point charge distribution and the equivalent smeared gaussian charge and compensating gaussian charge with the point charges. This figure has been adapted from [43].

order to do so one has to solve the Poisson equation Eq. 1.25.

$$-\nabla^2 \phi(r) = 4\pi\rho(r) \quad (1.25)$$

Doing a Fourier transform we have

$$k^2 \phi(k) = 4\pi\rho(k) \quad (1.26)$$

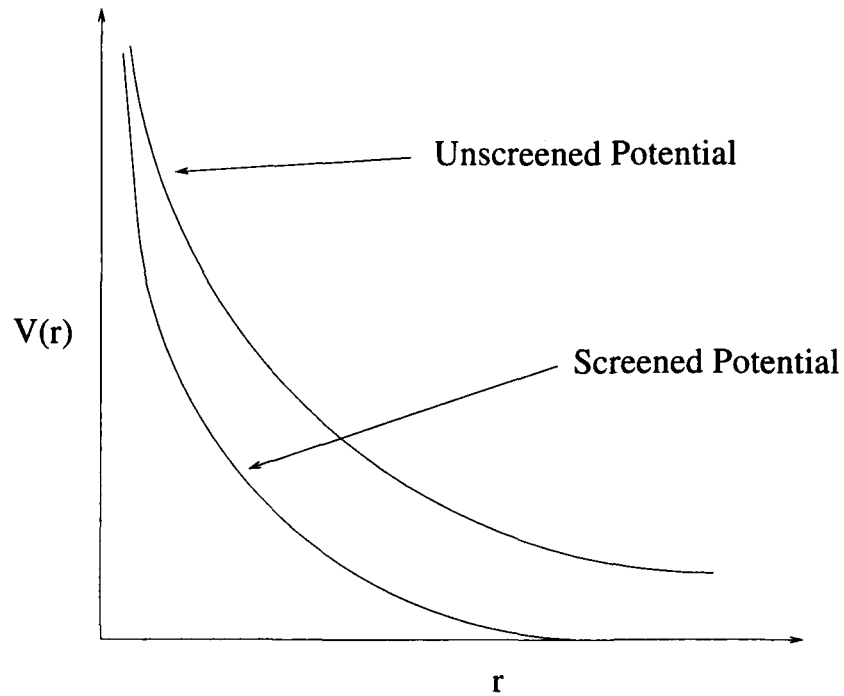


Figure 1.17: Screened and unscreened potential $V(r)$ as a function of the distance. The long range behaviour is depleted due to the screening. This figure has been adapted from [43].

where $\rho(k)$ is defined as

$$\rho(k) = \int_V \mathbf{dr} z \delta(r) \exp[-i\mathbf{k}\cdot\mathbf{r}] \quad (1.27)$$

We then have

$$\phi(k) = \frac{4\pi z}{k^2} \quad (1.28)$$

If we define $g(k)$ as the solution per unit charge ($\frac{4\pi}{k^2}$) we have

$$\phi(k) = g(k)\rho_P(k) \quad (1.29)$$

$\rho_P(k)$ is the the distribution of point charges in the smeared case we would have the distribution of the form

$$\rho(k) = \int d\mathbf{r}' \gamma(\mathbf{r}') \rho_P(\mathbf{r} - \mathbf{r}') \quad (1.30)$$

Using the convolution theorem we have,

$$\phi(k) = g(k) \gamma(k) \rho(k) \quad (1.31)$$

We now go further to calculate the Fourier part of the Ewald Sum. The potential at the point \mathbf{r}_i due to a periodic distribution of gaussians having a charge distribution $\rho_1(r)$ given by

$$\rho_1(r) = \sum_{j=1, N} \sum_{\mathbf{n}} q_j \left(\frac{\alpha}{\pi}\right)^{3/2} \exp[-\alpha |\mathbf{r} - (\mathbf{r}_j + \mathbf{nL})|^2] \quad (1.32)$$

Here \mathbf{n} runs over all the periodic cells. The Fourier transform of the charge density ρ_1 is

$$\begin{aligned} \rho_1(\mathbf{k}) &= \frac{1}{V} \int_{\text{all space}} d\mathbf{r} \exp[-i\mathbf{k} \cdot \mathbf{r}] \sum_{j=1, N} q_j \left(\frac{\alpha}{\pi}\right)^{3/2} \exp[-\alpha |\mathbf{r} - \mathbf{r}_j|^2] \\ &= \frac{1}{V} \sum_{j=1, N} \exp(-i\mathbf{k} \cdot \mathbf{r}_j) \exp\left(-\frac{k^2}{4\alpha}\right) \end{aligned} \quad (1.33)$$

We thus obtain $\phi_1(k)$ as

$$\phi_1(k) = \frac{4\pi}{k^2} \frac{1}{V} \sum_{j=1,N} q_j \exp(-i\mathbf{k} \cdot \mathbf{r}_j) \exp\left(-\frac{k^2}{4\alpha}\right) \quad (1.34)$$

The real space the potential $\phi_1(r)$ is then the Fourier transform

$$\phi_1(r) = \sum_{k \neq 0} \sum_{j=1,N} \frac{4\pi q_j}{k^2} \exp[i\mathbf{k} \cdot (\mathbf{r}_i - \mathbf{r}_j)] \exp\left(-\frac{k^2}{4\alpha}\right) \quad (1.35)$$

The energy U_1 due to all charges is then given by

$$\begin{aligned} U_1 &= \frac{1}{2} \sum_i q_i \phi_1(r_i) \\ &= \frac{1}{2V} \sum_{k \neq 0} \sum_{j=1,N} \frac{4\pi q_j q_i}{k^2} \exp[i\mathbf{k} \cdot (\mathbf{r}_i - \mathbf{r}_j)] \exp\left(-\frac{k^2}{4\alpha}\right) \\ &= \frac{V}{2} \sum_{k \neq 0} \frac{4\pi}{k^2} |\rho(k)|^2 \exp\left(-\frac{k^2}{4\alpha}\right) \end{aligned} \quad (1.36)$$

Here $\rho(k)$ is defined as

$$\rho(k) = \frac{1}{V} \sum_{j=1,N} q_j \exp[i\mathbf{k} \cdot \mathbf{r}_j] \quad (1.37)$$

The previous calculation yields an extra term due to the Gaussian distribution and the point charge at the center of the Gaussian. The self interaction term needs correction. The charge distribution that is over counted is

$$\rho_{Gauss}(r) = q_i (\alpha/p_i)^{3/2} \exp[-\alpha r^2] \quad (1.38)$$

The Poisson equation is given by

$$-\frac{1}{r} \frac{\partial^2 \phi_{Gauss}(r)}{\partial r^2} = 4\pi \rho_{Gauss}(r) \quad (1.39)$$

Substituting for ρ_{Gauss} and integrating twice we have

$$\phi_{Gauss}(r) = q_i \text{erf}(\sqrt{\alpha}r) \quad (1.40)$$

Here $\text{erf}(x)$ is the error function. The spurious contribution is at $r = 0$.

Thus the total self energy is

$$\begin{aligned} U_{self} &= \frac{1}{2} \sum_{i=1, N} q_i \phi_{self}(r_i) \\ &= \left(\frac{\alpha}{\pi}\right)^{1/2} \sum_{i=1, N} q_i^2 \end{aligned} \quad (1.41)$$

Energy of point charges and Oppositely charged Gaussian is easy to calculate. If the charge is q_i with the oppositely charged screening gaussian would yield a net potential of (Fig 1.17)

$$\begin{aligned} \phi_{short-range}(r) &= \frac{q_i}{r} - \frac{q_i}{r} \text{erf}(\sqrt{\alpha}r) \\ &= \frac{q_i}{r} \text{erfc}(\sqrt{\alpha}r) \end{aligned} \quad (1.42)$$

The net potential due to this term is thus

$$U_{short-range} = \frac{1}{2} \sum_{i,j} q_i q_j \text{erfc}(\sqrt{\alpha}r)/r_{ij} \quad (1.43)$$

Finally collecting Eq 1.36, 1.41 and Eq. 1.43 one gets the total Ewald sum energy, which is given by

$$U_{Coul} = \frac{V}{2} \sum_{k \neq 0} \frac{4\pi}{k^2} |\rho(k)|^2 \exp\left(-\frac{k^2}{4\alpha}\right) \quad (1.44)$$

$$- \left(\frac{\alpha}{\pi}\right)^{1/2} \sum_{i=1, N} q_i^2$$

$$+ \frac{1}{2} \sum_{i \neq j} q_i q_j \operatorname{erfc}(\sqrt{\alpha r}) / r_{ij} \quad (1.45)$$

Utilizing this procedure helps in improving the efficiency of the MD simulations for long ranged interactions.

1.5.4 Energy Minimization

We have discussed earlier that a powerful way to understand the energy landscape of a supercooled liquid is to divide the landscape into basins. The basin minima are identified by hyper-quenching instantaneous liquid configurations to their closest local minima (inherent structures). We discuss here the numerical procedure which has been used in the calculations of inherent structures. The method is known as the conjugate gradient minimization. Before introducing the method we will discuss a simpler variant known as the steepest descent method. Consider a system of N particles interacting via potential $V(r_1, \dots, r_N)$ having coordinates r_1, \dots, r_N . The idea here is to calculate the gradient of the potential $\nabla V(r_1, \dots, r_N)$ for an instantaneous set

of coordinates r_1, \dots, r_N obtained from molecular dynamics. Once the gradient direction is specified one moves along the negative gradient (*i.e.*, the force). We move only as long as the energy decreases along the force direction (line).

$$\mathbf{r}_{i_{n+1}} = \mathbf{r}_{i_n} - \lambda \nabla V(r_1, \dots, r_N) \quad (1.46)$$

$\mathbf{r}_{i_{n+1}}$ is the new position vector and \mathbf{r}_{i_n} is the old position vector. The parameter λ determines the distance to move until the energy is a minimum along the negative gradient direction. This procedure is also known as the line minimization procedure. A root finding procedure such as the bisection method is typically used for the line minimization procedure. Once one has line minimized we again find the gradient and this procedure is continued until the gradient is less than a certain tolerance value. This assures us that we are at the closest minimum to the instantaneous position we started from. The conjugate minimization procedure is an efficient variant of the steepest descent which optimizes the direction of the move. The conjugate gradient direction is given by,

$$\mathbf{h}_{i+1} = \mathbf{g}_{i+1} + \gamma_i \mathbf{h}_i \quad (1.47)$$

where \mathbf{g}_{i+1} is the gradient at the $i+1^{\text{th}}$ step and \mathbf{h}_i is the conjugate direction at the i^{th} step, the scalar quantity γ_i is given by the relation

$$\gamma_i = \frac{\mathbf{g}_{i+1} \cdot \mathbf{g}_{i+1}}{\mathbf{g}_i \cdot \mathbf{g}_i} \quad (1.48)$$

The details of calculation of the conjugate gradient is given in [124]. The important thing to notice here is that optimization memory is always present

in the conjugate direction chosen.

1.6 Outline of the Thesis

With this introduction to supercooled liquids, I am in a position to explain the rest of my thesis. This thesis consists of six chapters. Chapter 2 deals with the behaviour of a well known glass former KABMLJ at low temperatures above the glass transition. Chapter 3 deals with electronic structure of supercooled silicon which is known to exhibit a structural phase transition in the temperature range studied. We study how this phase transition triggers an electronic phase transition. Chapter 4 deals with the mechanical and dynamical properties of glass forming liquids especially in the context of a newly proposed phase diagram unifying jamming phenomenon in various systems such as gels, colloids, granular materials and glass forming liquids. Chapter 5 deals with the boundaries of existence of a liquid namely the spinodal and the glass transition line. We apply here semi analytic and numerical procedures to confirm computer simulation which predict a finite temperature intersection of the ideal glass and the spinodal line. Chapter 6 deals with the onset of break down of the Stokes-Einstein relation in supercooled liquids.

Chapter 2

Low-Temperature Behaviour of the Kob-Andersen binary mixture

2.1 Introduction

As described in the introductory chapter, when a liquid is cooled fast enough below its melting temperature, crystallization can be averted. The liquid then is called supercooled. On cooling much further the liquid gets into a glassy phase. In the range of temperatures between the melting and the glass transition temperature the liquid shows very rich dynamic and thermodynamic behaviour. The emergence of slow dynamics as a liquid is cooled, as a precursor to glass formation at low enough temperatures in the absence of crystallization, has been studied extensively. In particular, computer simulations have played an important role in elucidating many details not accessible

to experiments, and not amenable to simple theoretical modeling and calculation. Such simulation studies have been performed either for simplified model potentials [67, 108, 113], or empirical potentials for specific substances such as water, silica, and orthoterphenyl (OTP) [56, 82, 87, 97, 106, 114, 131]. A widely studied [104, 105, 109] model system in the former category is the Kob-Andersen binary Lennard-Jones mixture (KABMLJ) [67]. Until recently, molecular dynamics simulations of KABMLJ as well as other systems have largely been performed at temperatures above the mode coupling temperature [49]. A notable exception has been silica, where it has been observed that a crossover takes place in the temperature dependence of the diffusivities, from super-Arrhenius dependence at intermediate temperatures, to Arrhenius temperature dependence at low temperatures [56].

Among the approaches that have been extensively employed in analysing aspects of slow dynamics and the glass transition is the inherent structure approach [115, 117, 118], wherein the configuration space explored by the liquid at a given state point is characterized *via* the statistics and properties of local potential energy minima (inherent structures) sampled. Computer simulations have played a significant role in pursuing this approach, as they permit a detailed analysis of the dynamics of the system, as well as the generation and analysis of local energy minima. In addition to energy minima, attention has also been paid recently to the analysis of saddle points [2, 24], their connection to the study of instantaneous normal modes [64], as well as more global aspects of connectivity in the energy landscape, which may be employed in developing dynamical models to describe relaxation in liquids at low temperature [35, 36, 78].

Some of the studies mentioned above have been directed at understanding the nature of the dynamical crossover that is associated with the critical temperature of mode coupling theory. In [104], evidence was presented for a change in the local topography of the energy minima sampled above and below this crossover temperature, as well as for a change in the heights of barriers separating energy minima. A detailed analysis of the dynamics of transitions between energy minima [108] provided evidence that below a crossover temperature, one begins to observe a clear separation between vibrations within basins of individual energy minima and transitions between them, as discussed long ago by Goldstein [48]. The analysis of the order of saddle points sampled by the liquid as a function of temperature [2, 24] shows that the saddle order extrapolates to zero at the estimated mode coupling temperature; thus, the nearest extremum point on the potential energy surface below the mode coupling temperature is a minimum. A similar analysis, in terms of negative eigen value instantaneous normal modes [110], lead to the same conclusion. However, the studies mentioned above were based on simulations which were performed above the crossover temperature in question. It is of interest to revisit some of these analysis with simulations performed both above and below the crossover temperature. We present preliminary results here from a set of simulations of the Kob-Andersen BMLJ liquid, which extend to temperatures below the mode coupling temperature.

2.2 Computational details

Results presented here are from molecular dynamics simulations of the Kob-Andersen BMLJ, with 204 type A and 52 type B particles. The particles interact *via* the Lennard-Jones (LJ) potential, with parameters $\epsilon_{AB}/\epsilon_{AA} = 1.5$, $\epsilon_{BB}/\epsilon_{AA} = 0.5$, $\sigma_{AB}/\sigma_{AA} = 0.8$, and $\sigma_{BB}/\sigma_{AA} = 0.88$, and $m_B/m_A = 1$. The LJ potential is modified with a quadratic cutoff and shifting at $r_c^{\alpha\beta} = 2.5\sigma_{\alpha\beta}$ [104]. All quantities are reported in reduced units, length in units of σ_{AA} , volume V in units of σ_{AA}^3 (density $\rho \equiv N/V$, where N is the number of particles, in units of $\sigma_{AA}^{-3} \equiv \rho_0$), temperature in units of ϵ_{AA}/k_B , energy in units of ϵ_{AA} and time in units of $\tau_m \equiv (\sigma_{AA}^2 m/\epsilon_{AA})^{1/2}$, where $m = m_A = m_B$ is the mass of the particles. A time step of $0.003\tau_m$ is used in most of the runs, but a bigger time step of $0.01\tau_m$ is used for the lowest temperature studied. All the simulations are performed at the reduced density of 1.2. Molecular dynamics simulations are performed at constant energy $[(N,V,E)]$, over a wide range of temperatures, using the velocity Verlet integration. The temperature for the runs are calculated, as usual, from the average kinetic energy of the particles. Run lengths range from 4.5 million time steps ($29.1ns$, using Argon units for the A particles, *i. e.* $\epsilon_{AA} = 119.8K \times k_B$, $\sigma_{AA} = 0.3405 nm$, $m_A = 6.6337 \times 10^{-26} kg$) at the highest temperature to 510 million time steps ($11\mu s$) at the lowest temperature. Local energy minimizations are performed for a few thousand configurations for each temperature, to obtain a sample of typical local energy minima or ‘inherent structures’ [115,117,118]. The Hessian (matrix of second derivatives of the potential energy) evaluated at the minima are diagonalized to obtain the vibrational frequencies.

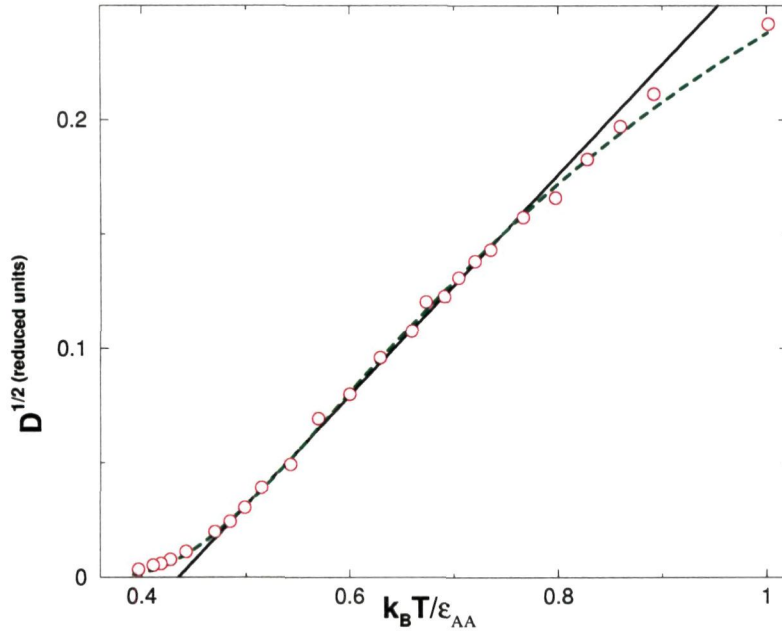


Figure 2.1: Diffusivity of A particles, raised to $1/2$, plotted against temperature. The data points are linear in the intermediate temperature range. Also shown are the straight line fit (black, solid, line; corresponding to power-law behaviour), and the VFT fit to the data (dashed line).

2.3 Results

The mean squared displacement of A and B particles are calculated from the MD trajectories as a function of time. The slopes of the mean squared displacements *vs.* time, reported as the diffusivities D , are shown in Fig. 2.1 for the A particles. In [67], the mode coupling temperature T_{MCT} was estimated to be 0.435, and the power-law exponent γ was estimated to be 2. A plot of the $D^{1/\gamma}$ *vs.* temperature should linearize the data in the range where the mode coupling behaviour holds. This is seen to be the case for the intermediate temperature range shown in Fig. 2.1. Also included in the plot are the power-law fit (straight, solid, line) and a VFT fit (dashed line) to the

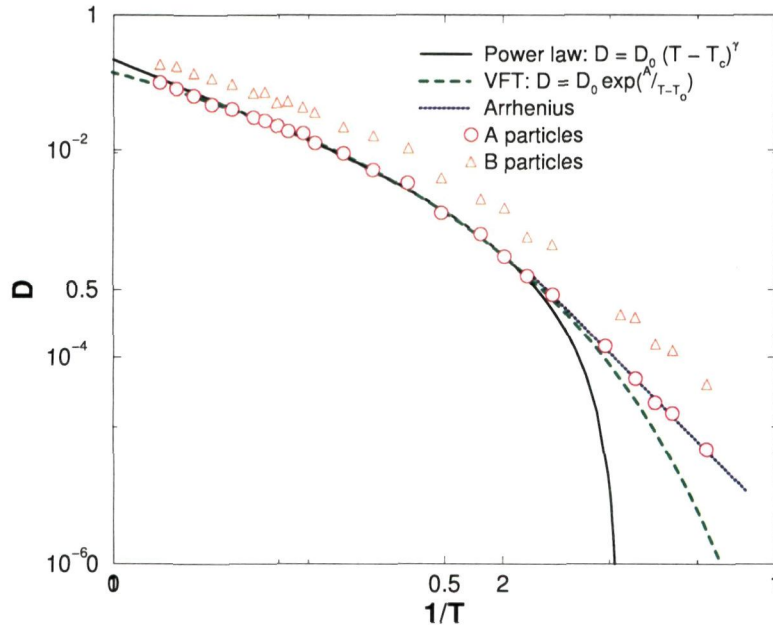


Figure 2.2: Diffusivity of *A* (circles) and *B* (triangles) particles, shown in an Arrhenius plot. Also shown are the straight line fit (black, solid, line; corresponding to power-law behaviour), the VFT fit to the data (dashed line), and the low temperature Arrhenius fit, for the *A* particles.

data. It is clear that for temperatures below 0.469, the diffusivities deviate from the power-law behaviour.

The diffusivity data for both *A* and *B* particles is shown in Fig. 2.2, in an Arrhenius plot. It is seen that above $T = 0.469$, the diffusivities show non-Arrhenius behaviour, which has previously been reported [100]. Below $T = 0.469$, however, the temperature dependence is seen to be Arrhenius. Also shown in the figure are the power-law (solid line) and VFT (dashed line) fits for the *A* particles. In both cases, the fits are obtained for data above $T = 0.469$. It is seen that neither fit describes well the data at lower temperatures. The diffusivities for the *B* particles show a similar trend. However, the ratio

of the A particle and B particle diffusivities is temperature dependent; at high temperatures (above $T = 1.0$), the ratio is roughly constant with a value of about 1.25, but increases progressively at lower temperatures, reaching a value of about 4.25 at the lowest temperature shown (data not shown). A crossover to Arrhenius temperature dependence has been observed in the case of silica, in which case the experimentally observed behaviour is Arrhenius. The observation of Arrhenius temperature dependence in the Kob-Andersen liquid, which is generally described in the literature as a typical ‘fragile’ liquid (as opposed to silica, the archetypal ‘strong’ liquid) is somewhat surprising and needs to be properly understood.

Next we present results concerning the local energy minima sampled by the liquid as a function of temperature. The mean squared distance between typical liquid configurations and the local energy minima to which they map, was considered in [104]. It was observed that the temperature dependence of this quantity shows a change in slope around the mode coupling temperature previously estimated [67]. In addition, evidence was also found for a change in the energy barriers separating basins of minima. However, in [104], the simulations were performed at specified cooling rates, and the cooling rates used were not small enough to permit equilibration at temperatures below the mode coupling temperature. The mean squared distance (MSD) separating instantaneous configurations, and the corresponding local energy minima, averaged over the sampled configurations, is shown in Fig. 2.3 as a function of temperature. Consistently with the observation in [104], the MSD values show a change in slope across the temperature where the diffusivities show a deviation from power-law temperature dependence. For comparison, we

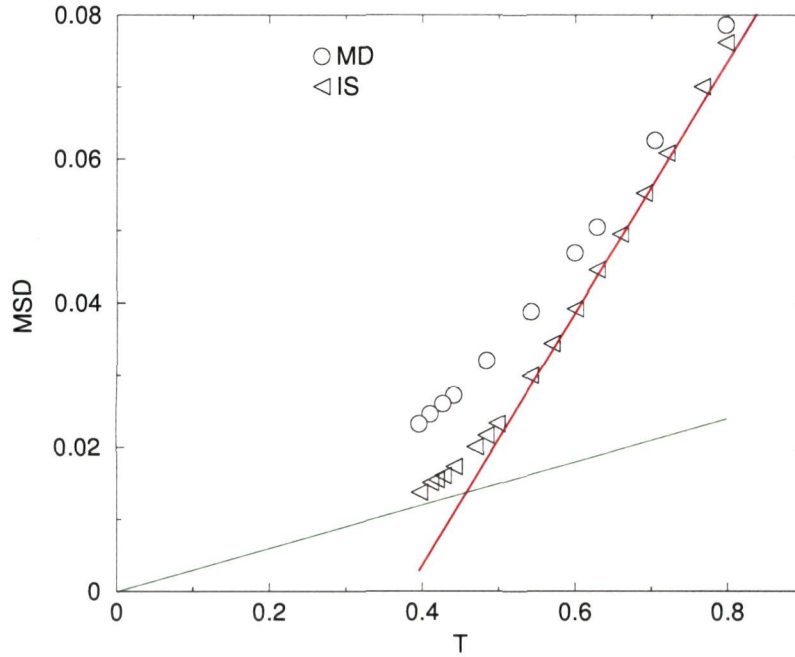


Figure 2.3: The mean squared distance between instantaneous configurations and the corresponding local energy minima (triangles), showing a crossover in slope around the mode coupling temperature. High and low temperature straight lines are drawn as a guide to the eye. The mean squared displacements from MD trajectories are also shown (circles).

calculate the plateau value of the mean squared displacement obtained from MD trajectories, calculated at $t = 1.2$. The time $t = 1.2$ corresponds to the beginning of the plateau in a log-log plot of the mean squared displacement *vs.* time, for low temperatures where a clear plateau is discernible. These values track the inherent structure MSD values, as seen in Fig. 2.3, although the difficulty of determining the plateau value of the mean squared displacements at higher temperatures makes the comparison difficult.

The vibrational frequencies for the sampled minima are calculated by diagonalizing the Hessian matrix (matrix of second derivatives of the potential

energy). In the harmonic approximation to the basins, the basin free energy is proportional to the average of the logarithm of the frequencies, which we refer to as f_{vib} (see, *e.g.*, [109]). It has been observed that this part of the basin free energy depends linearly on the energy of the minima in the temperature range previously studied [102]. This quantity is shown in Fig. 2.4 as a function of the average inherent structure energy. It is observed that f_{vib} , while displaying the nearly linear dependence on the inherent structure energy for the higher temperatures, begins to deviate from such linear behaviour below $T = 0.469$ (corresponding to inherent structure energy per particle ~ -6.98). This must reflect a change in the topography of the basins sampled at lower temperatures, but further analysis is needed to characterize the nature of the change, and its significance.

2.4 Summary

Results concerning the dynamics and properties of the local energy minima have been presented [12] for the Kob-Andersen BMLJ liquid for a range of temperatures that extends below the mode coupling temperature previously estimated. The diffusivity displays a crossover at low temperatures to Arrhenius temperature dependence. The mean squared distance between instantaneous configurations and the corresponding local energy minima, as well as the vibrational frequencies, display a crossover in behaviour across the mode coupling temperature. It is important to mention a recent work [74] which models diffusion based on the density of diffusive directions and barrier heights of the potential energy landscape. This model

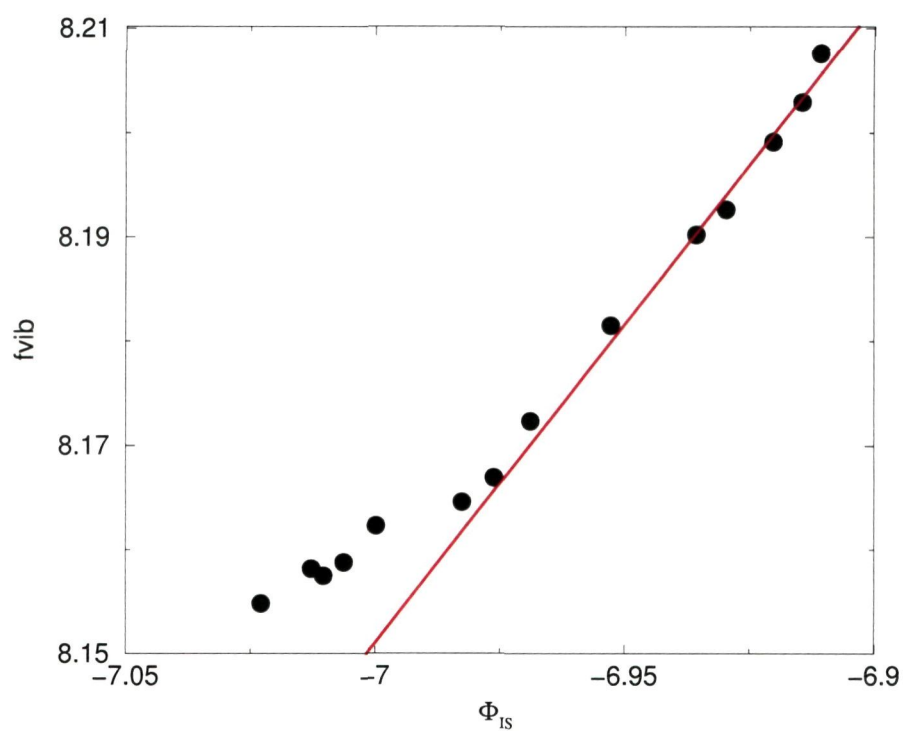


Figure 2.4: Average of the logarithm of vibrational frequencies, f_{vib} , shown as a function of the average inherent structure energy per particle. The straight line fit to the higher energy points is shown as a guide to the eye.

predicts a fragile to strong crossover [27] at approximately the same temperature as the T_{MCT} . The model considers particles following Brownian motion in the three dimensions, the means square displacement is modelled as $\langle r^2(t) \rangle = 6T[t - (1 - e^{-t})]$, in order to exhibit ballistic behaviour at short times and diffusive behaviour at long times. The number of diffusive directions above T_{MCT} is [2] is given by $k(T) = A(T - T_{MCT})^\gamma$. Below the T_{MCT} , the dynamics is dominated by barrier hopping, barrier height being ΔE . The diffusive directions below T_{MCT} was modelled as $k(T) = f_0 e^{\Delta E[1/T_{MCT} - 1/T]}$. The parameters f_0, A, γ etc., were fit to data from [2]. The diffusivity calculated from the mean square displacement of this model shows fragile behaviour at high temperatures and becomes Arrhenius at a temperature close to T_{MCT} . This model facilitates a qualitative understanding of the results of simulations presented. In the same breath we mention that, the behaviour of the configurational entropy in KABMLJ is analogous to silica [60], where one does find a fragile to strong cross over, but it is not sufficiently pronounced to be unambiguous.

Chapter 3

Electronic Structure of Supercooled Liquid Silicon

3.1 Introduction

Silicon is an element of technological importance, and of interest at a fundamental level, particularly in the crystalline and amorphous forms. In addition to the liquid-to-crystal transition occurring around $T_m = 1685K$, another first order *liquid to amorphous* transition $\sim 250K$ below T_m (in the supercooled liquid) has been inferred from experimental data [7, 15, 112]. Subsequent experiments at ambient [38, 125] and high pressures [33], as well as computer simulations [5, 72, 103] support the occurrence of such a transition. In particular, recent computer simulations [103] using the Stillinger-Weber (SW) potential [119] demonstrate the transition to be a *liquid-liquid transition*, as indeed suggested by Aptekar [7]. The inference, thus, is that

amorphous, *solid*, silicon is thermodynamically contiguous with the *low temperature* liquid (below the liquid-liquid (*LL*) transition), while the liquid at the freezing transition is thermodynamically continuous with the supercooled liquid above the *LL* transition. There has been considerable interest in *LL* transitions in single component substances [23], proposed and studied extensively in recent years, *e.g.*, for water [79, 94], silica [98], carbon [47], and phosphorus [62]. Brazhkin *et al* [22] have interpreted large changes in electronic conductivity in iodine, selenium and sulphur at high pressures, to be due to *LL* phase transitions. Amorphous silicon (a-Si) is a semiconductor, while liquid silicon near T_m is a metal [46]. It is thus of interest to study changes in conductivity and electronic structure of silicon with temperature in the supercooled liquid, and in particular, those occurring at the *LL* transition [14]. We address these questions in this chapter, and investigate the nature of localization properties of the wave functions above and below this phase transition, how the atomic structure affects the localization, what the electronic and conductive properties are of inherent structures (local energy minima) obtained from high and the low temperature phases across the liquid-liquid phase transition [13].

3.2 Elements of Electronic Structure

Before we attempt to introduce the electronic structure in disordered systems, we will very briefly introduce electronic structure of crystalline systems. At the heart of studying electronic properties of condensed matter systems lies the problem of solving the Schrödinger equation. The method of plane waves

provides a general methodology to handle several types of differential equations, especially the Schrödinger equation for periodic systems. In the case of periodic crystals, the plane wave methods simplify as well as bring a good deal of understanding of the electronic structure in these systems by exploiting a fundamental theorem known as the *Bloch theorem* [9,18]. The electronic states in a crystal are described by the solutions to the Schrödinger equation.

$$\hat{H}\psi_i(\mathbf{r}) = \left[-\frac{\hbar^2}{2m}\nabla^2 + \hat{V}(\mathbf{r})\right]\psi_i(\mathbf{r}) = \epsilon_i\psi_i(\mathbf{r}) \quad (3.1)$$

The Hamiltonian \hat{H} consists of the kinetic part $-\frac{\hbar^2}{2m}\nabla^2$ and the potential term $\hat{V}(\mathbf{r})$, \mathbf{r} is the position coordinate. $\psi_i(\mathbf{r})$ are the electronic states which are normalized and which also obey periodic boundary conditions. The eigenfunctions $\psi_i(\mathbf{r})$ can be written as Fourier series.

$$\psi_i(\mathbf{r}) = \sum_{\mathbf{q}} c_{i,\mathbf{q}} \times \frac{1}{\Omega} \exp(i\mathbf{q} \cdot \mathbf{r}) \quad (3.2)$$

Where Ω is the volume of the crystal and $c_{i,\mathbf{q}}$ are the expansion coefficients. In the *bra* and *ket* notation we have

$$|\psi_i\rangle = \sum_{\mathbf{q}} c_{i,\mathbf{q}} |\mathbf{q}\rangle \quad (3.3)$$

Substituting this relation in the Schrödinger equation and using the following facts :

- $|\mathbf{q}\rangle$'s are orthogonal.
- Periodicity of the crystal potential allows one to expand the potential

in the form,

$$V(\mathbf{r}) = \sum_m V(\mathbf{G}_m) \exp(i\mathbf{G}_m \cdot \mathbf{r}) \quad (3.4)$$

where \mathbf{G}_m is the reciprocal lattice vector [9].

- The matrix elements of the kinetic energy are

$$\langle \mathbf{q}' | -\frac{\hbar^2}{2m} \nabla^2 | \mathbf{q} \rangle = \frac{\hbar^2}{2m} |q|^2 \langle \mathbf{q}' | \mathbf{q} \rangle \quad (3.5)$$

and the potential energy matrix elements is given by

$$\langle \mathbf{q}' | V | \mathbf{q} \rangle = \sum_m V(\mathbf{G}_m) \delta_{\mathbf{q}-\mathbf{q}', \mathbf{G}_m} \quad (3.6)$$

Note potential energy matrix element is finite only when \mathbf{q}, \mathbf{q}' differ by a reciprocal lattice vector.

If we define a \mathbf{k} such that $\mathbf{q} = \mathbf{k} + \mathbf{G}_m$ and $\mathbf{q}' = \mathbf{k} + \mathbf{G}_{m'}$, substituting this into the Schrödinger equation one obtains the following matrix form:

$$\sum_{m'} H_{m,m'}(\mathbf{k}) c_{i,m'}(\mathbf{k}) = \epsilon_i(\mathbf{k}) c_{i,m}(\mathbf{k}) \quad (3.7)$$

where,

$$H_{m,m'}(k) = -\frac{\hbar^2}{2m} |\mathbf{k} + \mathbf{G}_m|^2 \delta_{m,m'} + V(\mathbf{G}_m - \mathbf{G}_{m'}) \quad (3.8)$$

Hence the wave function for any given \mathbf{k} is given by,

$$\begin{aligned}\psi_i(\mathbf{k}) &= \sum_m c_{i,m}(\mathbf{k}) \times \frac{1}{\Omega} \exp[i(\mathbf{k} + \mathbf{G}_m) \cdot \mathbf{r}] \\ &= \exp(i\mathbf{k} \cdot \mathbf{r}) \frac{1}{\sqrt{N_{cell}}} u_{i,k}(\mathbf{r})\end{aligned}\quad (3.9)$$

Where $\Omega = N_{cell}\Omega_{cell}$, and Ω_{cell} is the volume of a unit cell and N_{cell} number of such cells. $u_{i,k}(\mathbf{r})$ is defined by,

$$u_{i,k}(\mathbf{r}) = \frac{1}{\Omega_{cell}} \sum_m c_{i,m} \exp(i\mathbf{G}_m \cdot \mathbf{r}) \quad (3.10)$$

$u_{i,k}(\mathbf{r})$ has the periodicity of the crystal. This is known as the *Bloch theorem* [9, 18]. Each state is identified by \mathbf{k} and in the limit of large volume Ω , \mathbf{k} become dense and $\epsilon_{i,k}$'s become a continuous band. The first *Brillouin zone* is the Wigner-Seitz cell [9] of the reciprocal lattice. Inside the Brillouin zone there is no boundary unlike other primitive cells where Bragg scattering can occur. All properties such as the total energy etc, can be obtained by integrating over \mathbf{k} in the Brillouin zone (BZ). One could write the average of the function $f_i(\mathbf{k})$, i denotes the discrete band index as,

$$\langle f_i \rangle = \frac{1}{N_k} \sum_k f_i(\mathbf{k}) \rightarrow \frac{\Omega_{cell}}{(2\pi)^3} \int_{BZ} d\mathbf{k} f_i(\mathbf{k}) \quad (3.11)$$

As we have just seen evaluation of bulk properties requires one to integrate over the Brillouin zone. In order to get accurate results one must have many points in the region of BZ, especially where the function varies rapidly.

Symmetry of the system can be exploited to reduce the number of points to integrate over. Such high symmetry points are known as *special points*. This is useful since all information can be found from states with \mathbf{k} inside the *irreducible Brillouin zone*. A general method proposed by Monkhorst and Pack [81] is widely used. For the sake of simplicity we illustrate the method for one dimension [75]. Consider the integral

$$I_1 = \int_0^{2\pi} \sin(k) dk = 0 \quad (3.12)$$

The exact value of the integral is given by the value of the integrand ($f_1(k) = \sin(k)$) at the midpoint ($k = \pi$) of the interval of integration, that is $I_1 = f_1(\pi)$. If the integrand has two functions $f_2 = A_1 \sin(k) + A_2 \sin(2k)$ then the value of the integral is given by sum over two points $f_2(k = \pi/2) + f_2(k = 3\pi/2)$, which are symmetric in the interval of integration. A general formula for a three dimensional crystal the \mathbf{k} points are given by [81]

$$\mathbf{k}_{n_1, n_2, n_3} = \sum_{i=1,3} \frac{2n_i - N_i - 1}{2N_i} \mathbf{G}_i \quad (3.13)$$

Where $n_i \in I$ and $n_i \in [1, N_i]$.

Solving the Schrödinger equation is a many body problem for the crystal. However one can invoke various approximations to solve this problem, each has a different degree of success depending on the kind of material. The nearly free electron approximation, the tight binding approximation and various other methods are dealt with in standard text books [9]. We use a method known as the *empirical pseudopotential method*. I will describe the

pseudopotential we use in section 3.5.1. This method involves approximating the total potential as a sum of spherical potentials that can be written in an analytic form (the coefficients of the summands being undetermined) and also possess the property of transferability between different structures. One then uses the photoemission data for the crystal obtained from experiments to fit the unknown coefficients of the analytic form, such that they yield the correct band structure. This method has been very useful since it allows bands of many important materials to be described by using only a few parameters.

3.3 Electronic Structure in Non-Crystalline Materials

In the limit of weak scattering the resistivity of liquid metals can be calculated by the formalism proposed by Ziman [41, 135]. If the mean spacing between the atoms is a and the mean free path is l in the limit of $l \gg a$ the Ziman theory would hold. The scattering in this theory is considered as a perturbation and since the system is a liquid and hence there is no axis of symmetry. The Fermi surface is assumed to be spherical. The scattering potential can be replaced by an empirical pseudopotential [8]. The amplitude of scattering by two atoms at a distance \mathbf{R} from each other is given by $[1 - \exp(i\mathbf{q}\cdot\mathbf{R})]f(\theta)$, where $\mathbf{q} = \mathbf{k} - \mathbf{k}'$, the change of wave vector due to the scattering and $f(\theta)$ is the amplitude scattered by an atom through an angle

θ . Neglecting multiple scattering the conductivity is then [83]

$$\sigma = e^2 S_F l / 12\pi^3 \hbar \quad (3.14)$$

where the Fermi surface S_F is assumed to be that of a sphere of radius k_F and is given by

$$S_F = 4\pi k_F^2 \quad (3.15)$$

The mean free path l is then,

$$\frac{1}{l} = N \int S(q)(1 - \cos(\theta)) |f(\theta)|^2 2\pi \sin(\theta) d\theta \quad (3.16)$$

N here is the number of atoms per cm^3 and $S(q)$ is the modified structure factor given by

$$S(q) = N^{-1} \int [1 + \exp(i\mathbf{q}\cdot\mathbf{R})]^2 g(R) d^3\mathbf{R} \quad (3.17)$$

Using the first order perturbation theory the resistivity is [83],

$$\rho = \frac{3\pi}{\hbar e^2 v_F^2 \Omega} \int_0^{2k_F} \frac{|v(q)|^2 S(q) q^3}{4k_F^4} dq \quad (3.18)$$

Here $v(q)$ is the form factor got from the pseudopotential. The possibility of applying the perturbation theory depends on the assumption that the perturbation is small. This theory has been successful in the case liquid metals. In the case of liquid silicon this does not yield the right results. It predicts the resistivity of the high temperature phase to be around $400 \mu\Omega cm$ compared to the known value of around $77 \mu\Omega cm$. A good way to treat a

liquid like silicon is described in detail in this chapter. One has a large random system in a supercell, and further one calculates electronic structure by assuming the supercell is periodic. The treatment from here on is the same as that for a crystal.

A powerful way of calculating conductivity in disordered systems was given by Kubo and Greenwood [126]. The Green-Kubo formalism goes beyond the approximations of the Ziman theory. This formalism involves calculating the conductivity for finite frequency ω and extrapolating it to zero frequency in order to get the DC conductivity. We give here a brief derivation of the formula. Assume that an electric field $F\cos(\omega t)$ acts on a specimen of volume Ω . Then the probability P that an electron makes a transition from a state of energy E to any of the degenerate states of energy $E + \hbar\omega$ can be calculated using perturbation theory and is given by,

$$P = \frac{e^2}{4} F^2 \frac{2\pi}{\hbar} | \langle E + \hbar\omega | x | E \rangle |_{\text{average}}^2 \Omega N(E + \hbar\omega) \quad (3.19)$$

The matrix elements are defined as

$$\langle E' | x | E \rangle = \int \psi_{E'}^* x \psi_E d^3x \quad (3.20)$$

Using the Ehrenfest's relation $[x_i, H] = p_i/m$, one writes the elements in the form

$$\langle E' | x | E \rangle = \frac{\hbar}{m\omega} D_{E+\hbar\omega, E} \quad (3.21)$$

where $D_{E',E}$ is defined as

$$D_{E',E} = \int \psi_{E'}^* \frac{\partial}{\partial x} \psi_E d^3x \quad (3.22)$$

This leads us to the result

$$P = \frac{\pi e^2 \hbar \Omega}{2m^2 \omega^2} F^2 |D|^2 N(E + \hbar\omega) \quad (3.23)$$

The mean rate of loss of energy $\frac{1}{2}\sigma(\omega)F^2$ can be related to the probability P . If $N(E)f(E)dE$ is the number of occupied states, where $f(E)$ is the Fermi distribution function. The probability that the state $E + \hbar\omega$ is unoccupied is given by $1 - f(E + \hbar\omega)$. $\hbar\omega$ is the energy absorbed in the quantum jump. One thus has

$$\begin{aligned} \sigma(\omega) = & \frac{2\pi e^2 \hbar \Omega}{2m^2 \omega^2} \int [f(E)(1 - f(E + \hbar\omega)) - f(E + \hbar\omega)(1 - f(E))] \\ & \times |D|_{average}^2 N(E)N(E + \hbar\omega)dE \end{aligned} \quad (3.24)$$

This quantity simplifies to

$$\sigma(\omega) = \frac{2\pi e^2 \hbar^3 \Omega}{m^2} \int \frac{[f(E) - f(E + \hbar\omega)] |D_{average}|^2 N(E)N(E + \hbar\omega)}{\hbar\omega} dE \quad (3.25)$$

In order to get the DC conductivity one calculates the conductivity close to the zero frequency and extrapolates the data to zero frequency. We have used this formalism to calculate the conductivity in the low and the high temperature phase of liquid silicon.

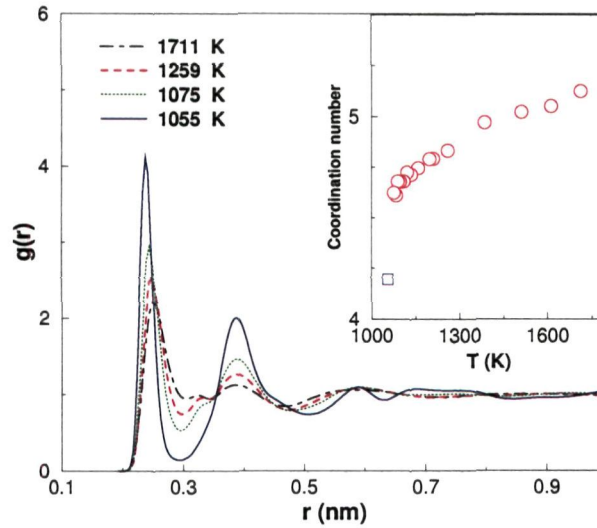


Figure 3.1: Pair correlation function change across the phase transition. The phase transition occurs at around 1060 K. One notices a distinct change in the pair correlation function between $T = 1055\text{K}$ and $T = 1075\text{K}$. The inset shows coordination number change across the transition. From Ref. [103]

3.4 Liquid-Liquid Phase Transition in Si

The freezing temperature at zero pressure for silicon has previously been estimated to be $\approx 1685\text{ K}$. It has been shown by Sastry and Angell [103] by computer simulation that supercooled silicon undergoes a first order liquid-liquid phase transition at around 1060 K at zero pressure. Constant temperature (NPT) and constant enthalpy (NPH) simulations were done for a 512 particle system using the Stillinger Weber Potential [119]. The low temperature phase is prone to crystallization on the scale of nanoseconds. A 63 ns long NPT simulation at $T=1055\text{ K}$ (the low temperature phase) which does not display crystallization, was used to demonstrate that the low temperature phase was a liquid. Illustrated in Fig 3.1 is the pair correlation function at $T = 1055, 1075, 1259$ and 1711K . One notices a distinct change around

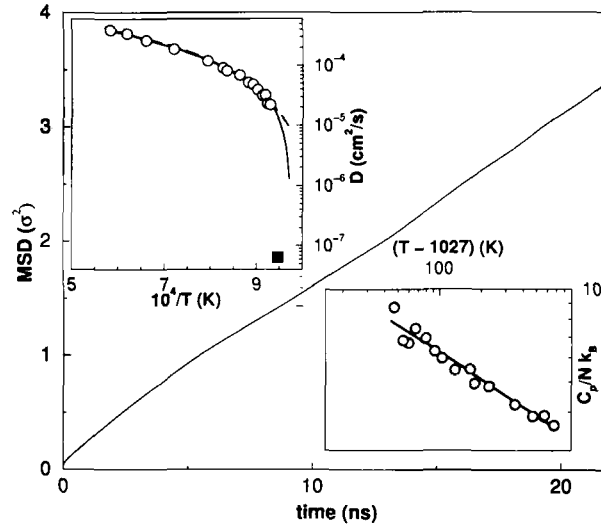


Figure 3.2: The mean squared displacement for the low temperature phase $T=1055$ K. This is evidence that the system has finite diffusivity. Also shown in the inset is the diffusivity *vs* inverse temperature. The lower inset shows specific heat at constant pressure. From Ref. [103].

the first minimum of the pair correlation function of the low temperature phase $T = 1055$ K and the high temperature phases. This gives rise to a coordination number jump of 4.2 to 4.61 across the transition. Diffusivity of the low temperature phase was seen to be three orders of magnitude lower than the high temperature phase (See Fig 3.2). It was confirmed that the low temperature phase has a finite diffusivity, a little more than glycerol at its melting point. This indicates that the low temperature phase is indeed a liquid.

3.4.1 Simulation of Liquid Silicon

The supercell method is the standard approach to study liquids using simulation. The idea is to imitate a liquid in the thermodynamic limit by assuming

a large collection of atoms in a big cell with periodic boundary conditions. The coordinates of the supercell are obtained from well equilibrated NPT simulations using Stilling Weber Potential (SW) [119] for 512 particle system. The Stillinger-Weber potential consists of two and a three body term. The two body term has the form:

$$v_2(r_{ij}) = \epsilon f_2(r_{ij}/\sigma) \quad (3.26)$$

Here f_2 is given by,

$$\begin{aligned} f_2 &= A(Br^{-p} - r^{-q})\exp[(r - a)^{-1}], & r < a \\ f_2 &= 0, & r > a \end{aligned} \quad (3.27)$$

The parameters appearing in the potential are given in the Table 3.1. The constants ϵ and σ are energy and length units and r_{ij} is the inter particle distance between the i^{th} and the j^{th} particles. The cutoff is at $r = a$, beyond which the potential is equal to zero.

The three body term has the following form:

$$v_3(\mathbf{r}_i, \mathbf{r}_j, \mathbf{r}_k) = \epsilon f_3(r_i/\sigma, r_j/\sigma, r_k/\sigma) \quad (3.28)$$

where f_3 is given by,

$$\begin{aligned} f_3(\mathbf{r}_i, \mathbf{r}_j, \mathbf{r}_k) &= h(r_{ij}, r_{ik}, \theta_{jik}) \\ &+ h(r_{ji}, r_{jk}, \theta_{ijk}) + h(r_{ki}, r_{kj}, \theta_{ikj}) \end{aligned} \quad (3.29)$$

Parameter	values
A	7.049556277
B	0.6022245584
p	4
q	0
a	1.8
λ	21.0
γ	1.20
σ	0.20951 nm
ϵ	50 kcal/mol

Table 3.1: Parameter of the Stillinger-Weber potential [119].

T in Kelvin	T in reduced Units
1055	0.0419
1082	0.0430
1258	0.0500
1510	0.0600
1711	0.0680

Table 3.2: MD simulation is done for the temperatures indicated in the table.

Here θ_{ijk} is the angle between $\mathbf{r}_i - \mathbf{r}_j$ and $\mathbf{r}_j - \mathbf{r}_k$ subtended at the vertex j .

The function h is given by

$$h(r_{ij}, r_{ik}, \theta_{jik}) = \lambda \exp[\gamma(r_{ij} - a)^{-1} + \gamma(r_{ik} - a)^{-1}] \cos(\theta_{jik} + \frac{1}{3})^2 \quad (3.30)$$

These Simulations were done for the temperature given in Table 3.2. First two temperatures in Table 3.2 are the temperatures across which the first order LL transition occurs.

3.5 The Hamiltonian

Heine and Aberenkov Pseudo potential

The empirical potential we use is a modified form of the Heine-Aberenkov pseudopotential [54]. Heine and Aberenkov have proposed a model pseudopotential which involves input from photoemission spectroscopic data for the core region rather than Hartree-Fock which is conventionally used. I briefly describe the method. Consider an energy eigen state with angular momentum quantum numbers l, m and energy E for an electron in the presence of an ion of charge Z . We define a core radius r_M . Outside the core, the potential is Coulombic and inside it is a constant A_l . The wave function outside the core is fully defined by the energy E , the angular momentum quantum numbers l, m and the boundary condition $\frac{\partial \ln(\psi)}{\partial r}$ at the core radius should be continuous. Similarly inside the core where the potential is a constant, the wave function is $j_l(\kappa r)$ (solution to the Schrödinger equation with constant potential) where $\kappa = \sqrt{2m(E + A_l)/\hbar^2}$ and again at the boundaries the logarithm of the wave function should be continuous. We then have a model potential which imitates the real potential, i.e., it yields the same eigen value and eigen function outside the core. The model potential in general has the form

$$\begin{aligned}
 V_{HA}(r) &= \sum_l A_l(E) P_l & r < r_m \\
 V_{HA}(r) &= \frac{-Ze^2}{r} & r > r_m
 \end{aligned}
 \tag{3.31}$$

A_0	2.08
A_1	2.39
A_2	2.44
r_m	2.00
Z	4.0

Table 3.3: Parameter for the Heine-Abherenkov potential

P_l is the projection operator which extracts from the wave function it operates the component of the total angular momentum l . One could use perturbation calculation to show that the energy is $\hbar^2 k^2 / 2m + E_{min}$, where E_{min} is the band energy minimum. One could obtain the band minimum from the cohesive energy. One further selects r_m to be more than the core radius. An electronic state with a quantum number l, m is chosen. One can then adjust the constant energy A_l such that the eigen states obtained match the term values. Heine and Aberenkov have computed the potential by taking A_l up to $l = 2$. The model now has the form

$$\begin{aligned}
 V_{HA}(r) &= -A_2 + (A_0 - A_2)P_0 - (A_1 - A_2)P_1 & r < r_m \\
 V_{HA}(r) &= \frac{-Ze^2}{r} & r \geq r_m
 \end{aligned} \quad (3.32)$$

Evaluation of this potential was done by Animalu and Hiene [53] wherein the exchange and screening were included.

3.5.1 Modified Pseudopotential

For the electronic structure (ES) calculation, we use a model pseudopotential [28] V_{Si} which approximates the total potential seen by valence electrons. We avoid the more elaborate density functional theory (DFT) calculations

in view of, (i) the high computational cost, and (ii) the underestimation of the band gap in DFT calculations. A comparison with DFT calculations is described later. The Hamiltonian we use is,

$$H = T + \sum_i^N V_{Si}(\vec{r} - \vec{d}_i), \quad (3.33)$$

where T is the kinetic energy and \vec{d}_i is the position of the i^{th} atom. V_{Si} is based on (a) the empirical potential fit by Cohen and Heine to optical data [28] (V_{OP}) and (b) the Heine-Aberenkov pseudopotential [54] (V_{HA}) for the long wave-length part, both of which were reported in \mathbf{q} (momentum) space. Pseudopotentials similar to ours have been employed with success in electronic structure calculations of a variety of liquids [8, 55], notably liquid carbon [55]. V_{OP} is available only for $\frac{q}{2k_F} > 0.5$ ($k_F = 0.9590 \text{ Bohr}^{-1}$ being the Fermi wave vector), which we smoothly interpolate using V_{HA} for $\frac{q}{2k_F} < 0.5$. Our choice thus combines the accurate band gap estimation of the Cohen-Heine pseudopotential with the analytical form of the Heine-Aberenkov pseudopotential for long wavelengths. We truncate our potential for $q > q_c$ ($\frac{q_c}{2k_F} = 1.26$), equivalent to a scattering length of roughly half the $Si - Si$ bond-length. The resulting model pseudopotential is (See Fig. 3.3):

$$\begin{aligned} V_{Si}(q) &= V_{HA}(q), & q < k_F \\ V_{Si}(q) &= V_{OP}(q), & k_F < q < q_c \\ V_{Si}(q) &= 0, & q > q_c. \end{aligned} \quad (3.34)$$

This choice of potential allows the use of a plane-wave basis set with an

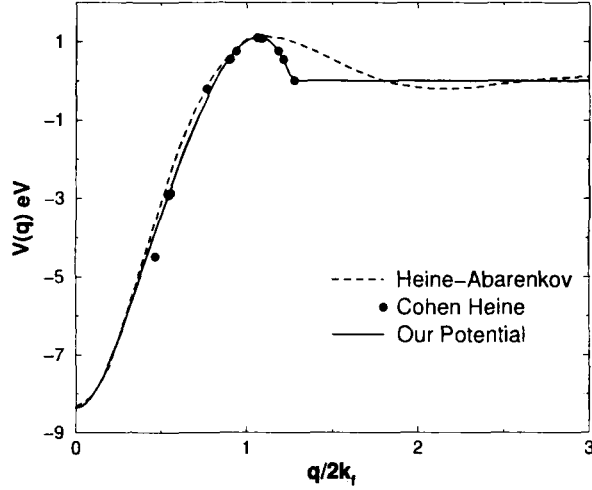


Figure 3.3: Comparison of our modified Pseudopotential with the Heine-Abarenkov Pseudopotential. Also shown are the Cohen-Heine [28] empirical fits to optical data.

energy cutoff of 69 eV to represent electron wave-functions (roughly 14000 plane waves per state of the 512 atom system). We obtain a band gap of 0.92 eV for crystalline silicon in the diamond structure, which compares well with the experimental value of 1.1 eV . We use a pre-conditioned conjugate gradient method [92] to diagonalize the Hamiltonian. In order to calculate the conductivity, we obtain states with energies at least $10k_B T$ above the Fermi energy E_f . We use 8 Monkhorst-Pack [81] (MP) points in sampling the Brillouin zone (BZ) of the 512-atom supercell, which amounts to sampling the BZ for the diamond structure with a $12 \times 12 \times 12$ MP mesh.

3.6 Procedure for Solving the Hamiltonian

We use a direct minimization procedure to diagonalize the Hamiltonian (H). As a first step one constructs a functional of the form $\langle \psi | H | \psi \rangle - \lambda \langle \psi | \psi \rangle$,

minimizing this functional would amount to minimizing H keeping the constraint that the wave functions remain orthogonal, thus diagonalizing H . λ , the Lagrange multiplier would correspond to the eigen energies obtained by diagonalizing H . The flow chart describing this procedure is given in Fig. 3.4. In principle one can update all the wave functions (all bands) simultaneously for a conjugate gradient iteration. Our system being large, one faces the problem of memory requirement for storing the wave functions. So it is very efficient to do single band updating as it retains all advantages of conjugate gradient without increasing memory requirements. The steepest descent direction is given by

$$g_k^m = -(H - \epsilon_k^m)\psi_k^m \quad (3.35)$$

Here k denotes the band, whereas m denotes the iteration number. ϵ_k^m is given by,

$$\epsilon_k^m = \langle \psi_k^m | H | \psi_k^m \rangle \quad (3.36)$$

The orthogonality constraint is maintained by ensuring that the steepest descent vector is orthogonal to all other bands. The steepest descent direction is calculated as

$$g_k'^m = g_k^m - \sum_{k \neq j} \langle \psi_j | g_k^m \rangle \psi_j \quad (3.37)$$

3.6.1 Conjugate Directions

Preconditioning is a method to make the functional dependence upon the variables more uniform. This involves making the curvature of the function

to be minimized with respect to all variables be similar in magnitude. The steepest descent directions are *preconditioned* using a preconditioning matrix K . The schemes for constructing K depend on the problem involved; a description may be found in [92]. Let the preconditioned steepest descent direction be η_k^m , given by

$$\eta_k^m = K g_k'^m \quad (3.38)$$

The preconditioned steepest descent direction is not orthogonal to all the bands. One further orthogonalizes the preconditioned steepest descent direction to all bands.

$$\eta_k'^m = \eta_k^m - \langle \psi_k^m | \eta_k^m \rangle \psi_k^m - \sum_{j \neq k} \langle \psi_j^m | \eta_k^m \rangle \psi_j^m \quad (3.39)$$

Using Eq 1.47 and 1.48 described in chapter 1, we can construct the conjugate direction (ϕ_k^m) from the preconditioned steepest descent direction

$$\phi_k^m = \eta_k^m + \gamma_k^m \phi_k^{m-1} \quad (3.40)$$

where γ_k^m is given by,

$$\gamma_k^m = \frac{\langle \eta_k'^m | g_k'^m \rangle}{\langle \eta_k'^{m-1} | g_k'^{m-1} \rangle} \quad (3.41)$$

and

$$\gamma_k^1 = 0 \quad (3.42)$$

Since the conjugate direction is constructed from the preconditioned steepest descent direction it is orthogonal to all the bands except the present band.

One needs to further orthoganalize it to the present band as follows

$$\begin{aligned}\phi_k^{\prime m} &= \phi_k^m - \langle \psi_k^m | \phi_k^m \rangle \psi_k^m \\ \phi_k^{\prime m} &= \frac{\phi_k^{\prime m}}{\langle \phi_k^{\prime m} | \phi_k^{\prime m} \rangle^{1/2}}\end{aligned}\quad (3.43)$$

3.6.2 Search for the Minimum (Circle Minimization)

An efficient minimization process is the so called *circle minimization*. The method is described here. The present wave function ψ_k^m and the conjugate direction vector $\phi_k^{\prime m}$ are both orthogonal to all the bands, a combination of these two vectors would also yield a vector which is orthogonal to all bands. We can exploit this fact and construct a vector of the form

$$\psi_k^m \cos(\theta) + \phi_k^{\prime m} \sin(\theta) \quad (3.44)$$

A “ θ ” is chosen such that it that minimizes our functional. The search for the minimum is performed by evaluating the functional for various values of “ θ ”. This amounts to searching for a minimum on a circle rather than a line minimization which is conventionally done for classical systems. One repeats the entire process until ψ_k and ϵ_k converge.

3.7 Results

In order to characterize the electronic structure the two phases of the liquid, we study the density of states (i) DOS(E), (ii) The density of states as a function of energy and a localization parameter, (iii) The resistivity using

the Kubo formula. Described below are results of our calculation.

3.7.1 Density of States

Density of states is an important parameter in the calculations of electronic structure, it is defined as

$$DOS(E) = \frac{1}{N_k} \sum_{i,k} \delta(\epsilon_{i,k} - E) \quad (3.45)$$

Where $\epsilon_{i,k}$ are the eigen states of the system in band k . Shown in Fig 3.5 is the density of states for the temperatures at which the analysis is done. The DOS remains essentially unchanged from $T = 1711K$ to $T = 1258K$. A small dip in the DOS at the Fermi energy E_f is apparent for $T = 1082K$, just above the transition. For $T = 1055K$, just below the transition, the dip in the DOS at the Fermi energy is dramatic. The DOS deviates significantly at other energies as well, compared to the DOS at higher temperatures. The DOS, however remains finite at the E_f , indicating a *pseudo gap* rather than a real gap which is observed in crystalline silicon.

3.7.2 Density of States in Energy and Inverse Participation Ratio

Conductivity depends not only on the DOS near E_f , but also on the degree to which the electronic states are localized. We therefore calculate the DOS as a function of both the energy and a measure of localization, the inverse

participation ratio (*IPR*), defined [37] as

$$IPR(\psi_k) = M \frac{\sum_i^M (|\psi_k(r_i)|)^4}{(\sum_i^M (|\psi_k(r_i)|)^2)^2} \quad (3.46)$$

where i runs over the M real space mesh points, and ψ_k is the wave function with a band index k . $IPR = M$ for fully localized states and $IPR = 1$ for a fully extended state. Figure 3.6-3.9 illustrate the density of states as a function of energy and *IPR* for all the studied temperatures. In Fig 3.10 is illustrated the contour plots of the $DOS(E, IPR)$ across the phase transition. At $T = 1082K$ (and at higher temperatures; contour plot data not shown) all states display roughly the same, low *IPR*, indicating that all states are extended. In contrast, at $T = 1055K$, states near the Fermi energy show markedly larger *IPR*, indicating a greater degree of localization. We may thus expect the conductivities for these two cases to be significantly different.

3.7.3 Resistivity

We calculate the frequency-dependent electrical conductivity $\sigma(\omega)$, using the Kubo formula [126], as previously done for liquid [1] and amorphous [37] silicon:

$$\sigma(\omega) = \frac{2\pi e^2}{3m^2V\omega} \sum_{i,k} (f_i - f_k) |\vec{M}_{i,k}|^2 \delta(E_k - E_i - \hbar\omega) \quad (3.47)$$

where e is the electron charge, V is the volume of the system, ω is the frequency, and f_i is the Fermi-Dirac occupation probability at electron energy

E_i . Matrix elements $\vec{M}_{i,k} = \langle \psi_i | \vec{P} | \psi_k \rangle$ (where \vec{P} is the momentum operator) are easily calculated in the plane wave basis. The DC conductivity is found by extrapolation to $\omega = 0$. Resistivities $\rho(\omega)$, shown in Figure 3.11 for four temperatures, vary slowly with T between $T = 1711K$ and $T = 1082K$, while for $T = 1055K$ the resistivity is significantly larger. We find the DC resistivity at $T = 1711K$ to be in the range of $70 - 80\mu\Omega cm$ which agrees very well with the experimental DC resistivity at 1740 K, in the range of $77 - 83\mu\Omega cm$ [46]. Our calculation yields better results than earlier methods for liquid Si [1] using the Slater-Koster (empirical LCAO) method. In the low temperature phase ($T = 1055K$) the DC resistivity is in the range $800 - 850\mu\Omega cm$, values typical of semi-metals (*e.g.*, graphite has a DC resistivity of $783\mu\Omega cm$). The resistivity at $T = 1082K$ is $120\mu\Omega cm$ which is comparable to that in metals, albeit on the higher end. The LL phase transition thus involves a roughly one order of magnitude jump in the resistivity, which may be termed a metal to semi-metal transition. Extrapolation of experimental data for a-Si in the range of 400 to 600°C [70]¹, yields resistivities ($0.66 - 3.3\Omega cm$) which are higher by 3 orders of magnitude than the calculated values for the low T liquid. We believe the difference to arise from the coordination number of 4.2 found for the low T liquid, higher than the a-Si value of 4. Such a discrepancy may arise either because the low T liquid structure is not predicted satisfactorily by the SW potential, or because in reality, the liquid structure is distinct from a-Si.

¹We have used the author's parameters for the Arrhenius temperature dependence of conductivity (slope $\sim 0.7eV$, $T^{-1} = 0$ intercept $\sim 100 - 500\Omega^{-1}cm^{-1}$) and used the experimental transition temperature of 1400K.

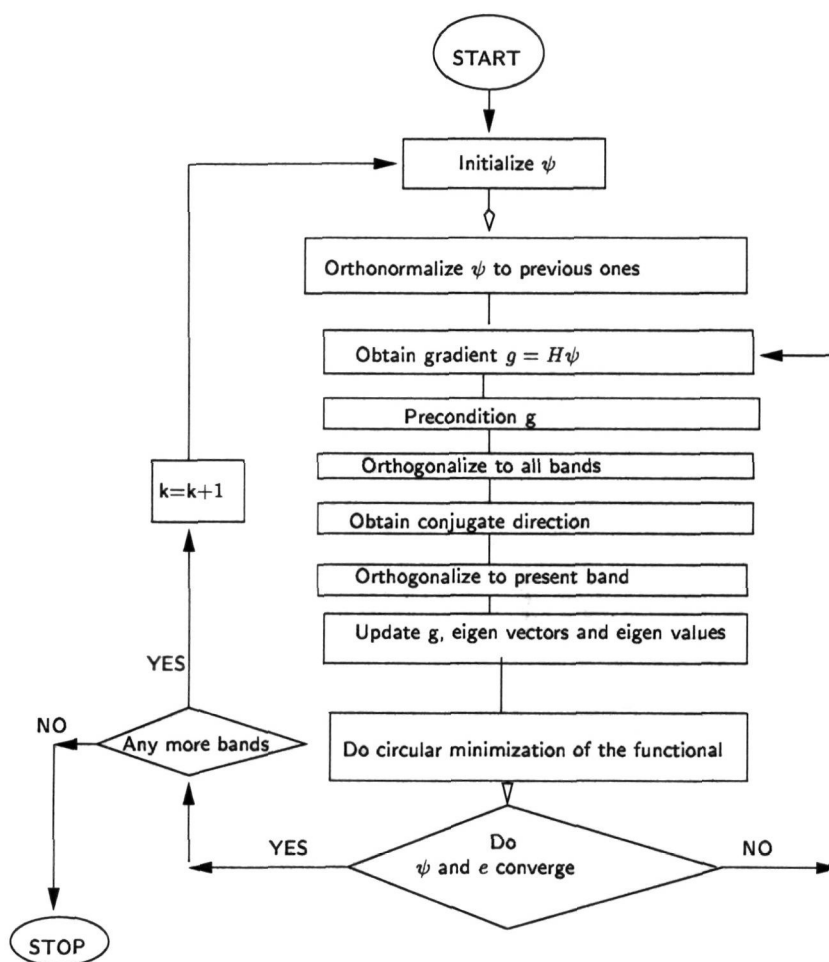


Figure 3.4: Flow chart of the algorithm for diagonalizing the Hamiltonian.

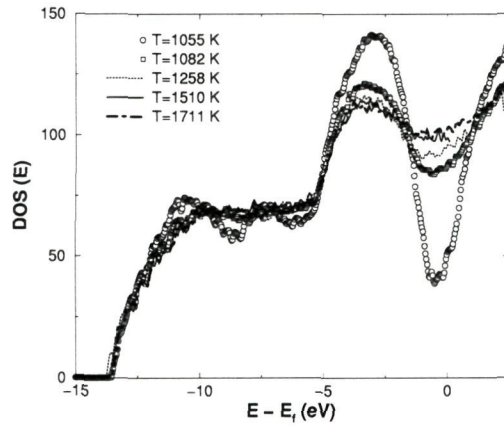


Figure 3.5: The electronic density of states (DOS) is shown for various temperatures analyzed. A pseudo-gap is seen for $T = 1055K$ (just below the LL transition). The DOS at higher temperatures approaches the free electron form, reflecting the observed metallic behavior. The Fermi energies are $11.21 eV$ ($1055K$), $11.83 eV$ ($1082K$), $12.1 eV$ ($1258K$), $12.05 eV$ ($1510K$), $11.99 eV$ ($1711K$).

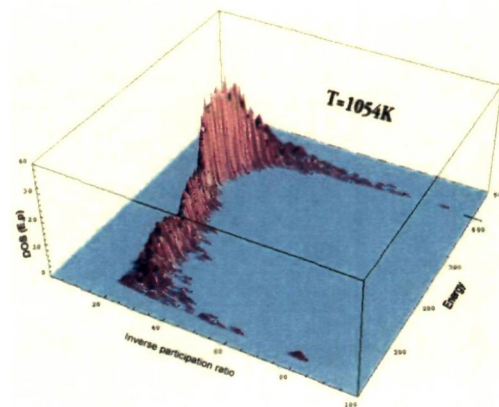


Figure 3.6: $DOS(E, IPR)$ for $T=1055 K$ the low temperature phase. The states near the Fermi energy are very localized.

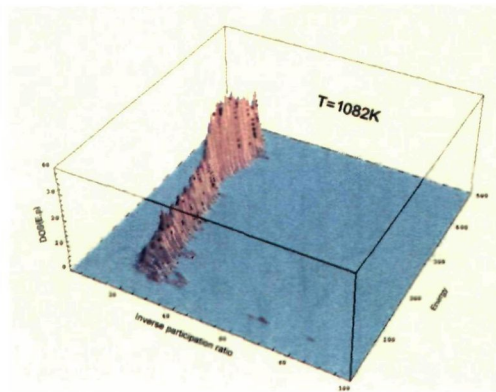


Figure 3.7: DOS(E,IPR) for T=1082 K the high temperature phase just above the transition. All states show low IPR values, importantly the ones close to the Fermi energy.

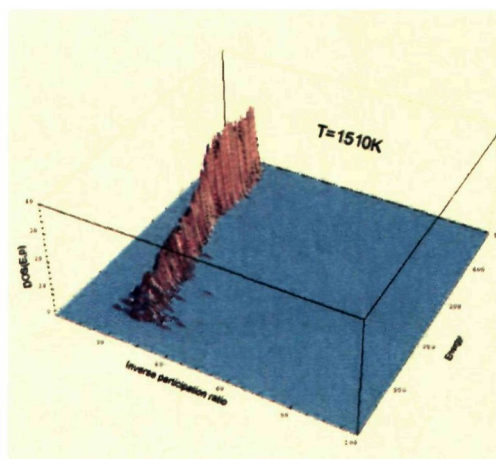


Figure 3.8: DOS(E,IPR) for T=1510 K. This phase shows the IPR values slightly lower than the T=1082 K. The IPR values tend to remain low.

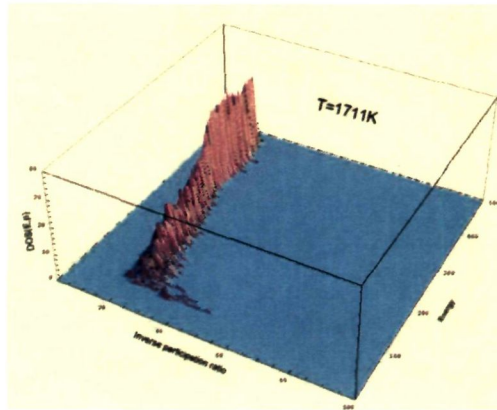


Figure 3.9: DOS(E, IPR) for $T=1711$ K. No significant change in the IPR values when compared to $T=1510$ K. The IPR values tend to remain low.

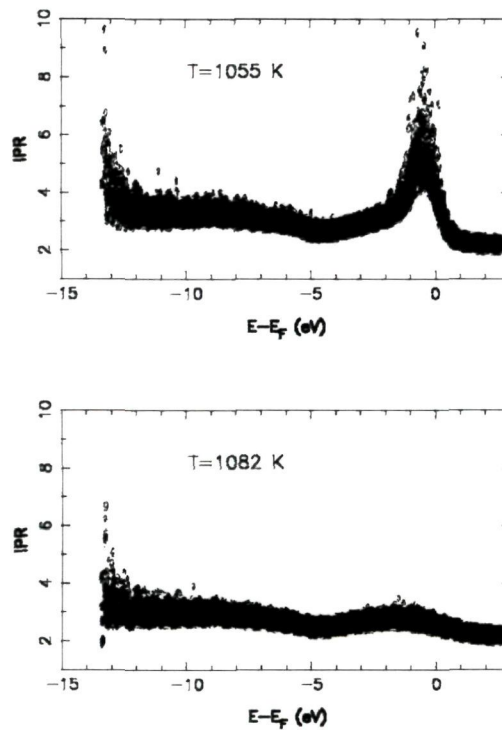


Figure 3.10: Contour plot of the density of states (DOS) as a function of $IPR(\psi_k)$ and energy for one configuration each at $T = 1055K$ and $T = 1082K$. The IPR for $T = 1082K$ remains essentially unchanged as a function energy, and is small, indicating that all states extended. For $T = 1055K$, states near the Fermi energy are seen to display a marked increase in IPR.

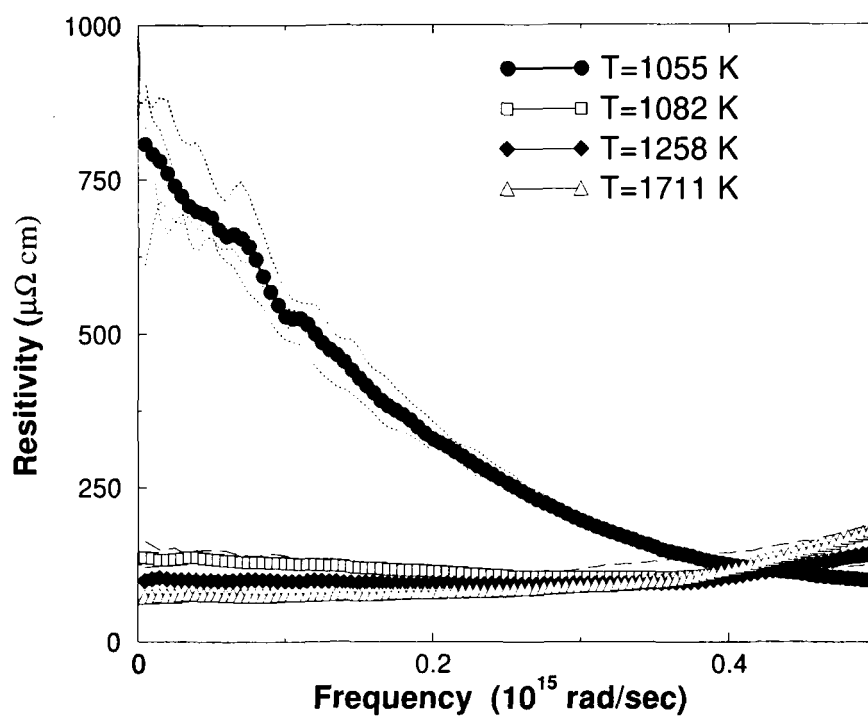


Figure 3.11: Plot of resistivity *vs.* frequency for $T = 1055K, 1082K, 1258K, 1711K$, showing a significant change in resistivity between $T = 1082K$ and $T = 1055K$. Thin lines (clearly visible only for $T = 1055K$) correspond to individual configurations and thick lines with symbols are averages for each temperature.

T (K)	Resistivity ($\mu\Omega cm$)	fraction (average over 5 configurations)	fraction (average over 1000 configurations)
1055	806	0.824707	0.787150
1082	196	0.45182	0.500658
1258	137	0.380859	0.349930
1711	72	0.32031	0.319750

Table 3.4: The table compares how the resistivity and the fraction of four coordinated atoms change as a function of temperature. The resistivities are calculated for a specific configuration whose fraction of four coordinated atoms are shown, also shown is average four coordination for the specified temperature. The average is taken over 1000 configurations.

3.8 Pinpointing the Cause of Conductivity change

There are several factors involved in the structural change across the *LL* phase transition. In this section we try to pinpoint the factor in the structural change which brings about the metal to semi-metal transition.

Illustrated in Table 3.4 is the resistivity for samples taken at several temperatures. As the temperature is increased the fourfold coordination in the liquid is lost. Shown in Table 3.4 is the fraction of fourfold coordinated atoms for specific samples whose resistivity is calculated, and the fraction of fourfold coordination averaged over 1000 configurations at the same temperature. We notice that fraction of the fourfold coordination increase correlates with an increase in resistivity. It should be noted that in crystalline silicon the coordination is four and it is a semiconductor. Shown in Fig. 3.12 is the angle distribution of the fourfold coordinated atoms at $T = 1055K$ and $T = 1082K$. One sees that the four fold coordinated atoms have a much

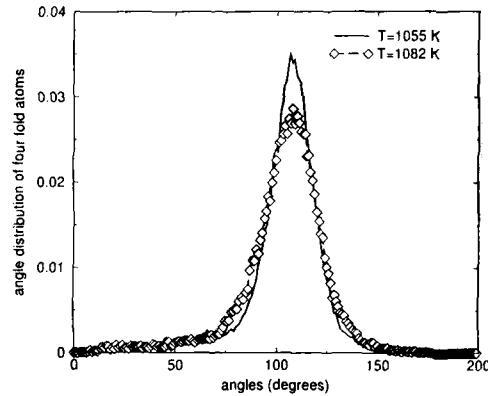


Figure 3.12: Normalized angle distribution of four coordinated atoms for the low ($T = 1055K$) and the high temperature phase is illustrated $T = 1082K$. The high temperature phase shows a broader distribution than the low temperature phase around the tetrahedral angle (109°) indicating that the low temperature phase liquid is more tetrahedral.

more tetrahedral geometry in the low temperature phase ($T=1055 K$), the angle distribution shows a peak near the tetrahedral angle of 109° . In the high temperature phase ($T = 1082K$) there is a decrease in height of the angle distribution maximum by about 17% indicating that the tetrahedrality of the system has decreased. Also the fraction of fourfold coordination changes 0.78 to 0.50. This is one very significant change in the structure of the system. Illustrated in Fig.3.13 are the angle distribution of the fivefold atoms at $T = 1055 K$ and $T = 1082 K$. One notices a peak close to the tetrahedral angle, but this is due to the fourfold atom contribution in the angle distribution. One notes that the distribution of the angle is much more spread out as compared to the fourfold case.

We will now analyze the influence of coordination on the pair correlation function. We will abbreviate four folded atoms as ff and the non four folded as nff . We then calculate the pair correlation function between (i) nff and

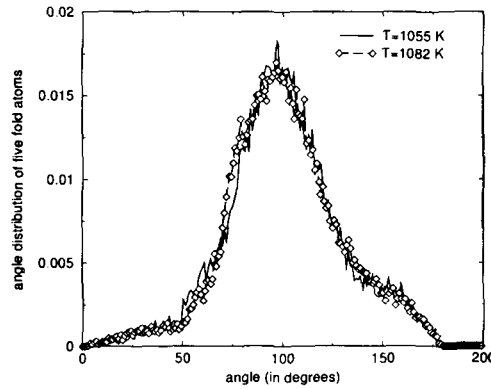


Figure 3.13: Normalized angle distribution of five coordinated atoms for the low ($T = 1055K$) and the high temperature phase is illustrated $T = 1082K$. The distribution is almost same in the high and the low temperature phase.

ff (Fig. 3.14), (ii) ff and ff (Fig. 3.15), (iii) nff and nff across the transition ie., for $T=1055$ and 1082 K (Fig 3.16). In the case of nff and ff , we find that across the transition, atoms from the second coordination shell peaks spreads such that nff and the ff atoms get closer. The $ff - ff$ correlation function shows that again across the transition we have ff atoms from the second coordination shell get closer to the first. Unlike the case of $nff - ff$ we find a small decrease in the atoms of the first coordination shell. If one were to look at the $nff - nff$ correlation function one would find that there is decrease in both the second and the third coordination shell across the transition. It should be noted no nff atoms coming closer to each other across the transition.

We now further investigate how this structural changes effect the electronic structure of the liquid. In order to find the contribution of the ff and the nff atoms to the electronic structure we use the following strategy. We obtain the charge distribution from the wave function by squaring the

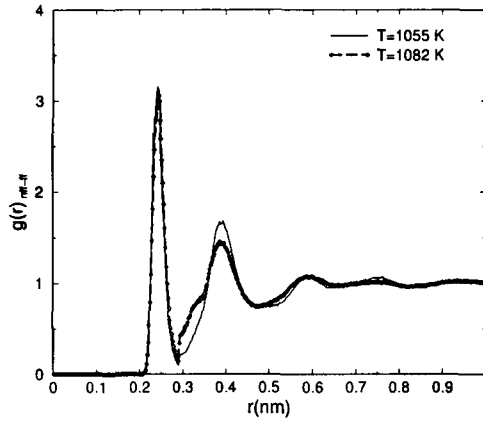


Figure 3.14: The partial pair correlation $g(r)_{nff-ff}$ between ff coordinated and the nff coordinated atoms, for temperatures $T = 1055$ K and $T = 1082$ K across the phase transition.

norm of the wave function. The box is divided into a $60 \times 60 \times 60$ mesh. Each of the eigen wave function is represented on the mesh points as charge density. The distance of each mesh point to all the atoms in the simulation box is calculated. The simulation box is divided into regions such that mesh points closest to a particular atom is said to belong to the region of the atom. This way the entire simulation box is divided into 512 regions, each region belonging to a particular atom. A region is defined as all the mesh points closest to a particular atom. We then take the charge on a mesh point in that region and multiply it to the *character* of the atom. The *character* of an atom is defined to be zero if it is a ff atom, else it is assigned a unit value. The net charge due to the atoms with unit *character* per mesh point is defined as the *projection ratio*. The projection ratio in principle is the charge contribution from the nff atoms per mesh point. The projection ratio is calculated for two cases of interest (i) high IPR wave functions i.e.,

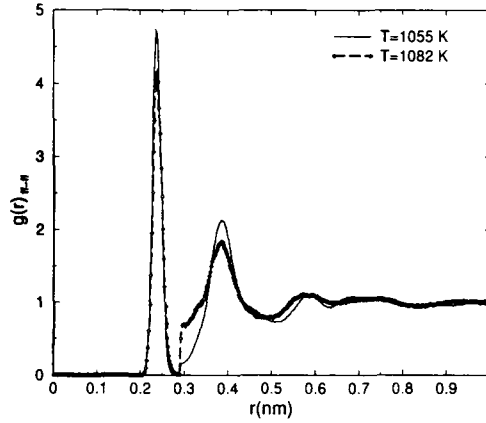


Figure 3.15: The partial pair correlation $g(r)_{ff-ff}$ between ff coordinated and the ff coordinated atoms, for temperatures $T = 1055$ K and $T = 1082$ K across the phase transition.

the localized wave functions which lie close to the Fermi energy (Fig.3.17). (ii) low IPR wave functions which are extended in nature (Fig.3.17). This would pinpoint if the localized character of the wave functions are due to the ff atoms. All these calculations are done for the low temperature phase $T = 1055$ K. This temperature is chosen since the tetrahedral character of the liquid is maximum in this case.

If it is true that the localization characteristic is due to the tetrahedral nature of the liquid structure, the projection ratio of the peak of the high IPR distribution should have been significantly lower than the projection ratio of the peak of the low IPR distribution. From Fig 3.17 it is clear that the peak of both the distributions occur at a projection ratio of 0.02052. But the high IPR distribution is shifted to low projection values which is consistent with localized states being preferentially localized near ff atoms. However the effect is not significant enough. This leaves us to investigate another

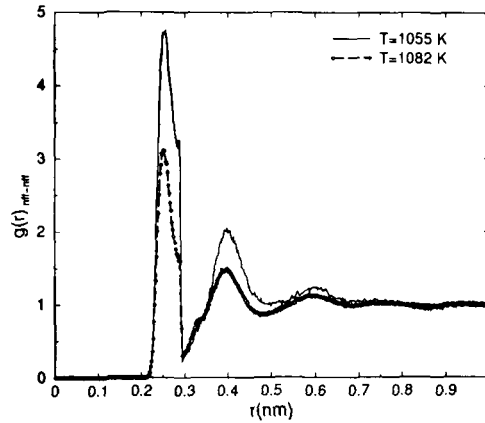


Figure 3.16: The partial pair correlation $g(r)_{nff-nff}$ between nff coordinated and nff coordinated atoms, for temperatures $T = 1055$ K and $T = 1082$ K across the phase transition.

important structural change, namely the coordination number change across the transition.

The density of the liquid jumps from 0.0524 above, to 0.0494 atoms per \AA^3 below, the LL transition.²The structure of the liquid also changes, as reflected, *e.g.* in the distribution of coordination number, whose average changes from 4.2 at $T = 1055K$ to 4.61 at $T = 1082K$, while the fraction of four-coordinated atoms changes from about 83% at $T = 1055K$ to about 43% at $T = 1082K$. The percentage of atoms displaying 3, 4 and 5 coordination (where a distance cutoff of 0.293nm is used) are, respectively, 0.268, 82.8, 16.1 for $T = 1055K$, 0.74, 42.9, 46.7 for $T = 1082K$ and 2.36, 28.9, 47 for $T = 1711K$ (Fig 3.18). The concentration of dangling bonds (associated with 3 coordinated atoms), at low temperatures where they may be expected

²The quoted densities are for 1055K and 1082K respectively. The lowest temperature above the LL transition at which a liquid was equilibrated in the present study was 1060K, where the density is .05207 atoms per \AA^3 .

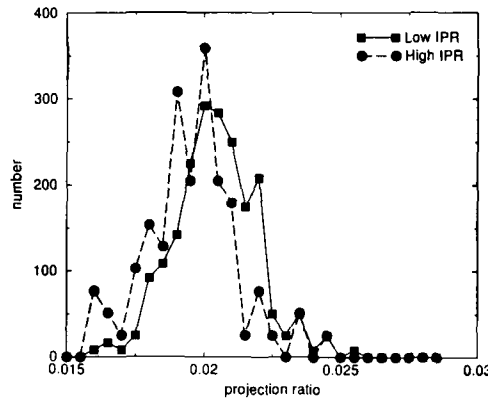


Figure 3.17: A normalized distribution of the projection ratio at $T = 1055K$, for a set of high IPR and low IPR wave functions is shown. Both the high and the low IPR distribution have peak around a projection ratio of 0.02052.

to play a significant role, is minimal, and would not have a substantial influence on the conductivity changes. To determine the relative importance of density and structural changes to electronic structure, we calculate the electronic structure for two additional atomic configurations obtained: (i) by rescaling atomic coordinates for a $T = 1055K$ configuration, to produce a configuration whose density equals that of the liquid at $T = 1082K$, (ii) by rescaling coordinates for a $T = 1082K$ configuration to produce a configuration whose density equals that of the liquid at $T = 1055K$. The DOS for these configurations, shown in Fig. 3.19 alongside the DOS for the original configurations, show that a change in density itself, without structural change, has marginal effect on the electronic DOS. We conclude that the marked change in the electronic DOS at the LL transition arises primarily from a change in liquid structure, rather than the change in density.

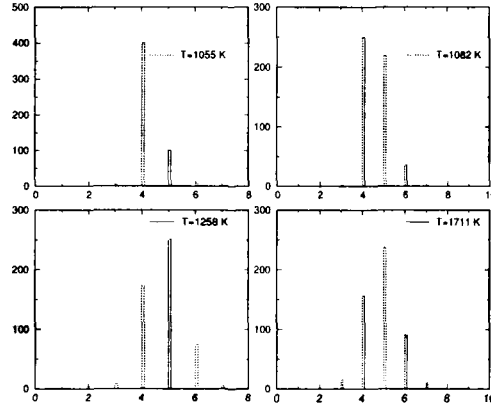


Figure 3.18: Histogram of the coordination number of the atoms at $T = 1055K, 1082K, 1258K, 1711K$

3.9 Comparison with First Principles Density Functional Theory

Since the coordination number of the liquid in the studied T range changes from 4.2 to 5.12, the reliability of the pseudopotential we use, based on data for four-coordinated crystalline silicon, needs further validation. To this end, we calculate the DOS (Fig 3.20), and resistivities for liquid configurations of 64 atoms for $T = 1082K, 1258K, 1510K$ and $1711K$ using our pseudopotential and *ab initio* DFT based on norm-conserving pseudopotential [52] (Fig 3.25). The DOS using the two methods agree reasonably, but the DFT band-widths are typically 8-10 % smaller, and, as remarked earlier, the pseudo-band gap is underestimated by DFT. We also include IPR compared for all the cases obtained from DFT and pseudopotential calculations (Fig 3.21-3.23).

Figure 3.24 shows the resistivities from the two methods for $T = 1258K$

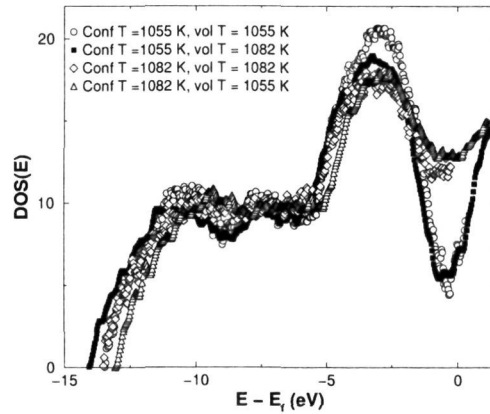


Figure 3.19: Density of states for (a) a $T = 1055K$ configuration, (b) the same $T = 1055K$ configuration, but with coordinates scaled so that the density equals that at $T = 1082K$, (c) a $T = 1082K$ configuration, and (d) the same $T = 1082K$ configuration, but with coordinates scaled so that the density equals that at $T = 1055K$.

and $1711K$, which are in moderate agreement for $T = 1711K$, and a much poorer agreement at $T = 1258K$. Since the liquid shows greater tetrahedral structure at $T = 1258K$, we conclude that the disagreement between pseudopotential and DFT calculations are due to the underestimation of the band gap by DFT rather than due to non-four-coordinated geometry. This supports our expectation that electronic structure itself is not so sensitive to the potential and its structure dependence can be captured well with a structure factor along with a reasonable potential [111].

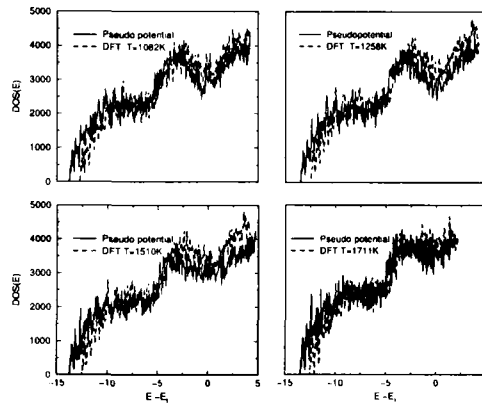


Figure 3.20: Density of states comparison for the DFT for temperatures $T = 1082K, 1258K, 1510K, 1711K$ are shown. The match is very good between these two methods for the high temperatures.

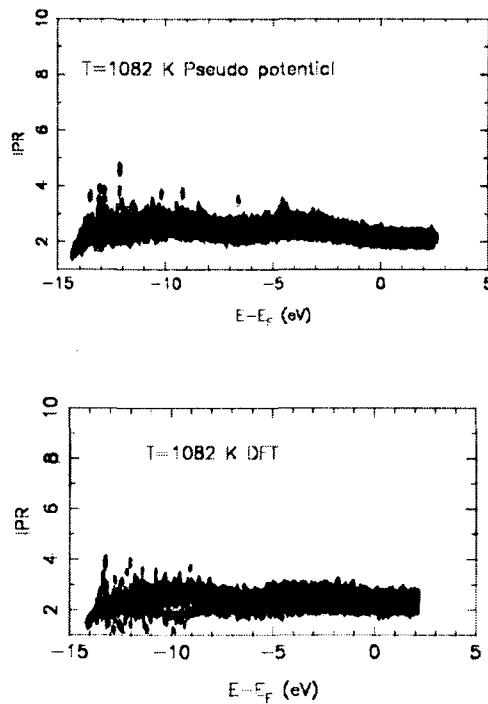


Figure 3.21: IPR comparison for the DFT for temperature $T = 1082K$. The localization characteristics predicted by Pseudo potential method and DFT are almost exact in the case of $T = 1082K$. This clearly justifies the use of the pseudopotential method for the study of localization properties in Si.

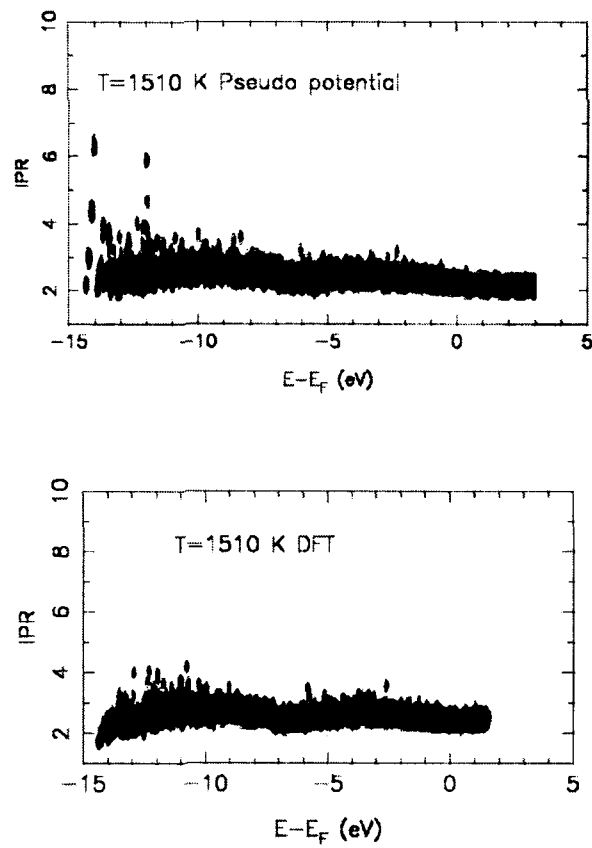


Figure 3.22: IPR comparison for the DFT for temperature $T = 1510K$. The localization characteristics predicted by Pseudo potential method and DFT are almost the same in the case of $T = 1510K$. This clearly justifies the use of the pseudopotential method for the study of localization properties in Si.

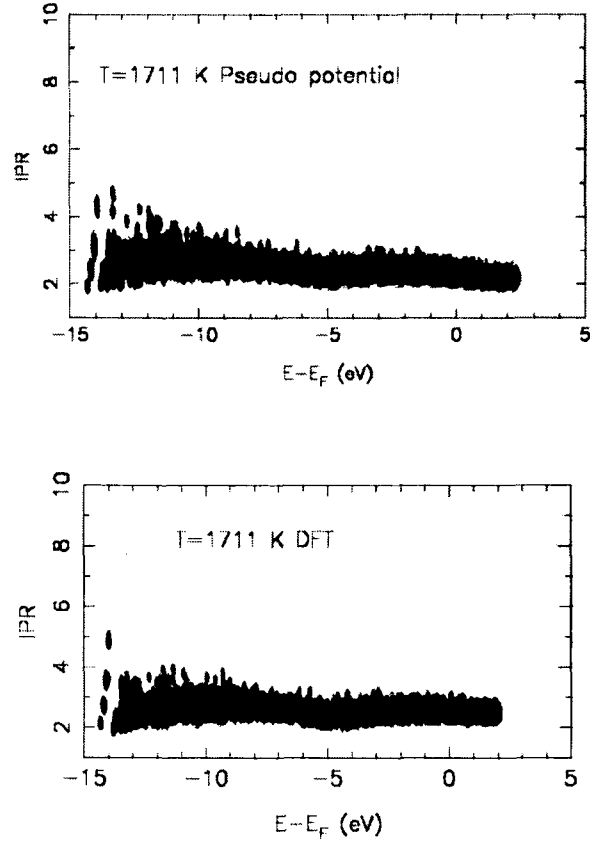


Figure 3.23: IPR comparison for the DFT for temperature $T = 1711K$. The localization characteristics predicted by Pseudo potential method and DFT are almost exact in the case of $T=1711 K$. This clearly justifies the use of the pseudopotential method for the study of localization properties in Si.

3.10 Electronic Structure of Inherent Structures

We further investigate the electronic behaviour of the inherent structures in the high ($T = 1082K$) and the low temperature phase ($T = 1055K$) across the phase transition. We use the conjugate gradient minimization for the

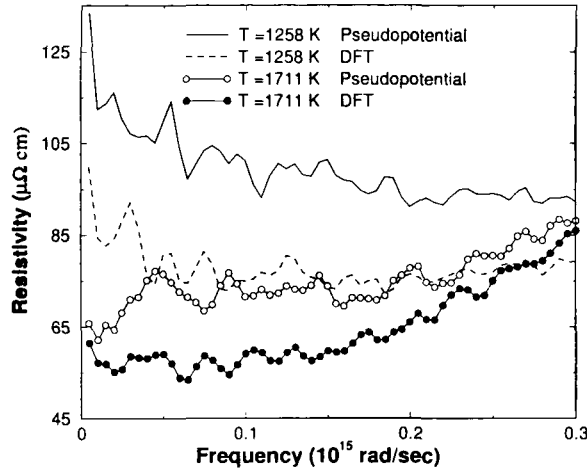


Figure 3.24: Plot of resistivity *vs.* frequency for $T = 1258K$ and $T = 1711K$, calculated using the pseudopotential, and using DFT. The resistivities from the two methods show better agreement at $T = 1711K$ – where the liquid shows greater non-tetrahedrality – than at $T = 1258K$ where the underestimation of the pseudo-band gap by DFT leads to underestimation of resistivities.

Stillinger-Weber potential to obtain the quenched states from the instantaneous states obtained from the earlier molecular dynamics simulation. Five inherent structure configurations are taken from the high and the low temperature phase. The density of states is calculated (See Fig 3.26). The height of the pseudo gap in the $T = 1055K$ is lower than the corresponding liquid. Localization properties from the contour plot show that the low T phase has about 15% larger *IPR* at the Fermi energy compared to the liquid, indicating that they are much more localized (Fig 3.27). Finally the resistivity shows about 56% increase for the inherent structure compared to the liquid for the low temperature phase (See Fig 3.28). The resistivity of the inherent structure quenched from $T = 1055 K$ is about $1250 \mu\Omega cm$, the

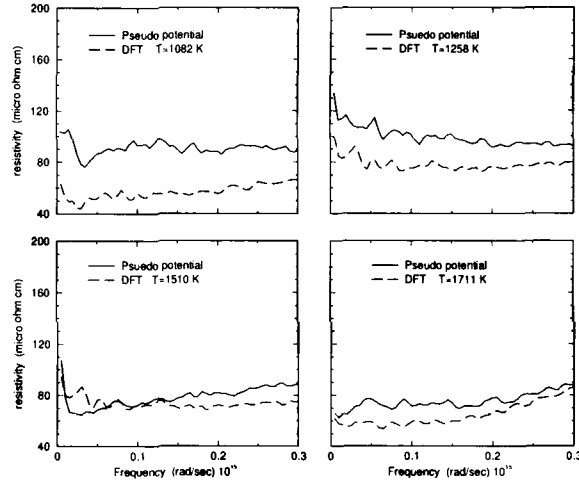


Figure 3.25: Plot of resistivity *vs.* frequency for temperatures $T = 1082, 1258, 1510, 1711\text{K}$ for both DFT and Pseudo potential methods. One would notice for the same temperature DFT resistivities are lower than the ones predicted by pseudopotential method. This difference seems to get lower for higher temperatures.

liquid is about $800 \mu\Omega\text{cm}$. In the high temperature phase the inherent structure resistivity quenched from $T = 1082\text{ K}$ is about $160 \mu\Omega\text{cm}$, which makes it about 33% more than the corresponding liquid (with a resistivity of about $120 \mu\Omega\text{cm}$).

3.11 Summary

In summary, we have demonstrated a metal to semi-metal transition in supercooled silicon [14], accompanying the *LL* transition previously found. The resistivity of the liquid changes by about one order of magnitude at the transition. Our analysis indicates the cause of the change in electronic properties to be the change in liquid structure rather than the density. We also have shown

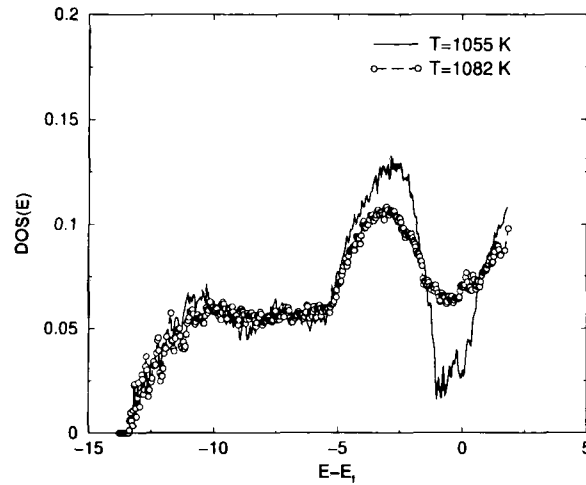


Figure 3.26: Plot of $DOS(E)$ for inherent structure from liquid at $T = 1055K$ and $1082K$ are shown. The pseudo gap in the low temperature phase is more pronounced than the liquid.

that the pseudopotential method works very well in our case. We have performed DFT calculations and shown that the pseudopotential method works better than DFT calculations for properties involving unoccupied states. We have also shown that our results compare well with experimental resistivities for the high temperature liquid. We have investigated the electronic properties of the inherent structure [13] of the high and low temperature phase across the transition. In the high temperature phase one finds an increased resistivity and localization of the wave functions in the inherent structures compared to the corresponding liquid configurations. In the low temperature phase the resistivity and the localization in the inherent structure phase is comparable to the liquid phase configurations.

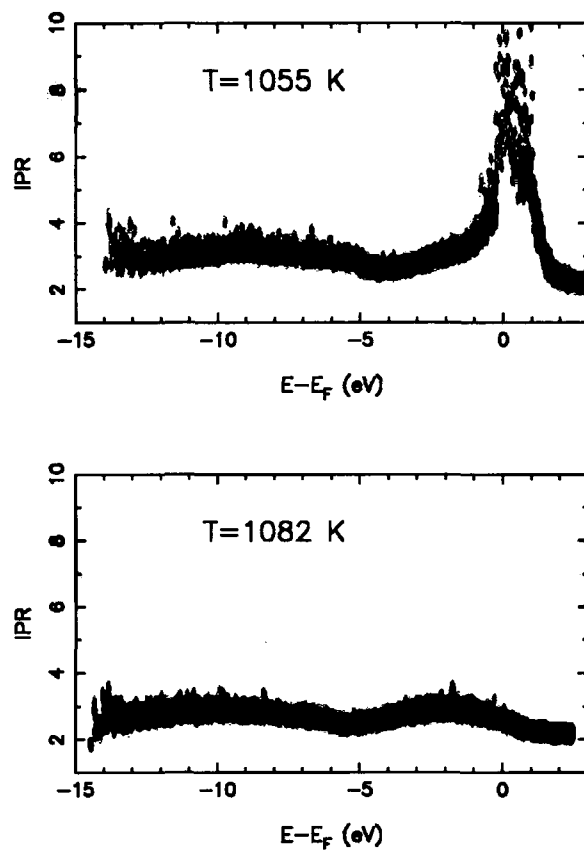


Figure 3.27: Contour plot of $DOS(E, IPR)$ for the inherent structure at $T = 1055K$ and $T = 1082K$ is illustrated. The $T = 1055K$ shows large localization more than the corresponding liquid.

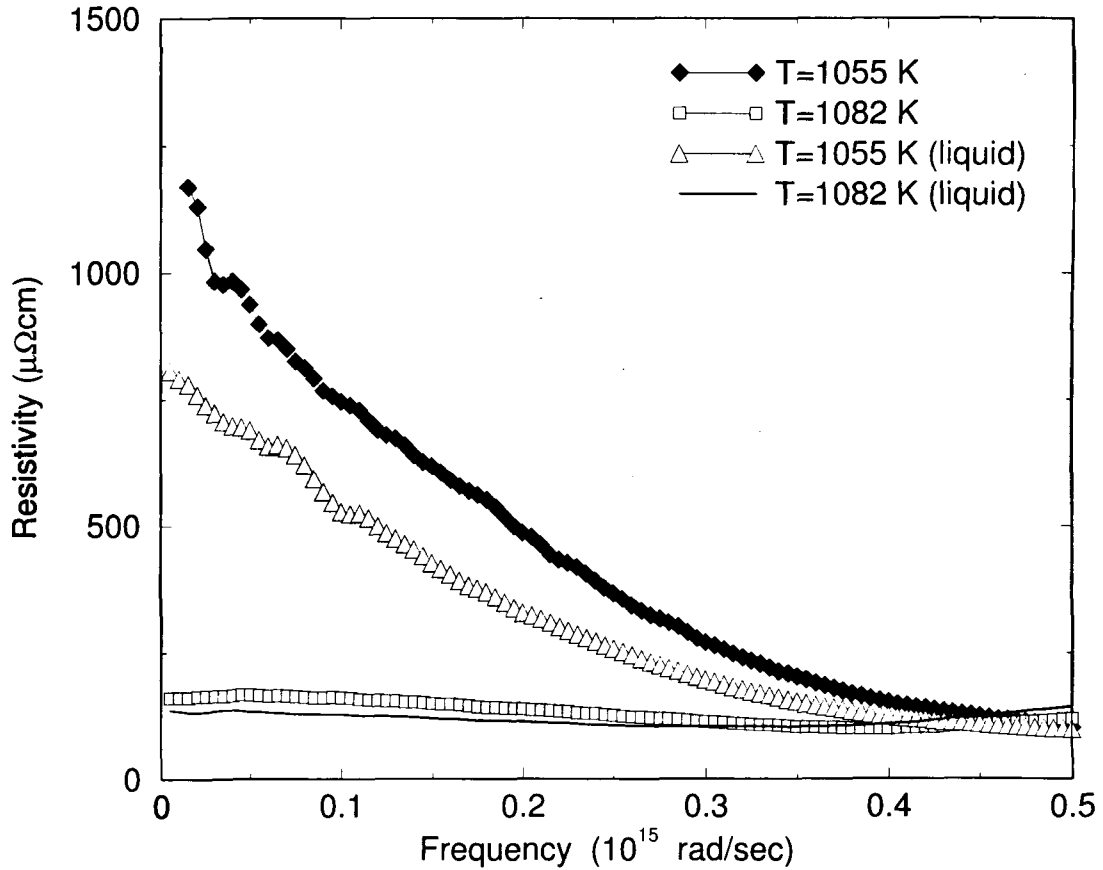


Figure 3.28: Plot of resistivity *vs.* frequency for temperatures $T = 1055K$ and $T = 1082K$ for the inherent structures and the corresponding liquid are shown. The DC resistivity for the inherent structure for $T = 1082K$ is $\sim 160 \mu\Omega cm$ and the liquid is about $120 \mu\Omega cm$. The low temperature phase $T = 1055K$, the DC resistivity for inherent structure is $\sim 1250 \mu\Omega cm$ and the liquid is $\sim 800 \mu\Omega cm$. The resistivity shows about 33% increase for the low temperature phase compared to the liquid and 56 % increase in the high temperature phase.

Chapter 4

The Relationship Between Mechanical and Dynamical Properties of Glass Forming Liquids

4.1 Introduction

Nagel, Liu and coworkers [86] have put forward a “jamming picture” which proposes a unified description of systems exhibiting structural arrest, including glass forming liquids, granular materials, colloidal systems, foams, gels, *etc.* Temperature and the associated thermal motion of atoms and molecules plays a significant role in the behaviour of glass forming liquids, while temperature plays no significant role in systems such as granular materials, which are therefore termed *athermal*. In athermal systems, the parameter that

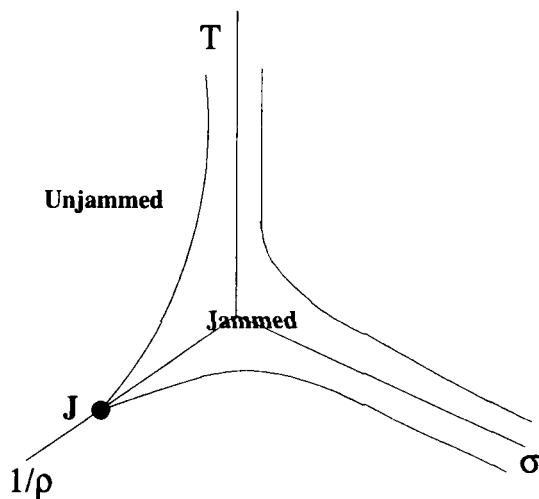


Figure 4.1: Unifying phase diagram, having density (ρ), load (σ) and temperature (T) as control parameters for jamming and the glass transition. The point J marks the zero temperature jamming.

determines the transition from jammed (or structurally arrested) states to fluid states is some form of external mechanical agitation, unlike glass forming liquids where temperature and density play the controlling role. Given the broad similarity of behaviour, *i. e.* a transition from a structurally arrested state to a fluid state, there has been an attempt in recent times to formulate a common description of both thermal and athermal systems within a unified picture. In this spirit, Liu and Nagel proposed a “jamming phase diagram” [86] where one conceives of a single jammed domain in a phase diagram with temperature, density and mechanical load forming independent control variables [127], as illustrated in Fig 4.1. Indeed, within the context of glass forming liquids themselves, the influence on dynamics of applied shear stress, in addition to temperature and density changes, has

been appreciated and studied for some time [17, 133]. The jamming picture has been very useful in demonstrating the equal stature of external driving, temperature and density in controlling flow both in and out of equilibrium in glassy systems [17, 91].

A quantity that has been studied recently in this context is the distribution of forces acting between particles in jammed *vs.* unjammed structures [61]. Initially studied for granular systems [26, 32], experimental and theoretical studies of three dimensional stationary bead-packs revealed an exponential distribution at large forces, with the presence of a finite, small force peak or plateau. A simulation study of compressible granular systems showed that at low stress, the distribution of forces is exponential, while a change to a Gaussian distribution is seen at high stresses [73]. Force distributions have also been studied recently in model glass forming liquids studied by computer simulations [88–90].

In these studies, it was found that in equilibrated liquids, the force distribution is a featureless exponential, and the exponential nature of the distribution was rationalized in terms of the interaction potential, the behaviour of the tail of the distribution argued to be more nearly exponential for inverse power law potentials with larger powers [88]. When the liquid falls out of equilibrium, the force distribution develops a small force peak, which is seen to present a signature of the glass transition [88]. In [89] evidence was shown of a breakdown of self-averaging in the force distributions for jammed configurations. Thus, the appearance of a plateau or peak at small forces, which marks the onset of jamming (the development of a yield stress) in a granular systems, may signal the onset of vitrification in a thermal system [88–90].

Interestingly, this feature would then serve as a subtle *structural* signal of the glass transition.

In this work [10], we investigate several aspects of the *dynamics* of supercooled liquids as they relate to jamming concepts. First, we investigate the correlation between force distribution $P(f)$ and the onset of vitrification in a variety of systems, including simple and more complicated liquids (such as networked liquids) that involve both attractive and repulsive interactions. Since the analogy with granular systems may be less clear in complex cases, e.g. network forming systems, our study is aimed to probe the boundaries of this aspect of the jamming picture. While we find that amorphous solids (as defined by inherent structures) always show essentially a Gaussian $P(f)$, in agreement with the jamming picture, the behaviour in the liquid state is perhaps more complex than that originally posited by O'Hern *et al* [88–90]. In particular, we do find examples where a plateau in $P(f)$ may occur in the equilibrium liquid phase, and where no plateau may occur even under glassy conditions. We postulate that the prominence of the plateau behaviour may be related to the fragility of the glass-former. Motivated by other aspects of the jamming picture, we qualitatively investigate the behaviour of force networks in the supercooled state, and investigate how the application of a shear strain disrupts local glassy states. In particular, we demonstrate that the onset of a rapid change in the depth of inherent structures (as well as the onset of non-exponential relaxation) is accompanied by a marked onset in the yielding behaviour of the local packing structures [69].

The chapter is organized as follows: Section 4.2 provides computational details concerning the systems we study. In section 4.3 we investigate the

correlation of the features of $P(f)$ for small forces f with the dynamical behaviour of the liquid. In section 4.4 we study the behaviour of the onset of inherent structure yielding with an applied shear deformation. In section 4.5, we qualitatively study various connections between the behaviour of inherent structures (and the transitions between them) with force distributions and force networks. Section 4.6 contains a discussion of our results and a summary.

4.2 Computational Details

We have studied the force distributions and related quantities for a number of model liquids, as described in subsequent sections. Here, the relevant computational details for each of these model liquids is briefly described. Further details are available in previously published work that are cited. The models we study are:

1. The Kob-Andersen binary Lennard-Jones liquid [67]. Systems consisting of $N = 256$ (204 type A and 52 type B) particles and $N = 10000$ particles (8000 type A and 2000 type B) have been studied. The particles interact *via* the Lennard-Jones (LJ) potential, with parameters $\epsilon_{AB}/\epsilon_{AA} = 1.5$, $\epsilon_{BB}/\epsilon_{AA} = 0.5$, $\sigma_{AB}/\sigma_{AA} = 0.8$, and $\sigma_{BB}/\sigma_{AA} = 0.88$, and $m_B/m_A = 1$. The LJ potential is modified with a quadratic cutoff and shifting at $r_c^{\alpha\beta} = 2.5\sigma_{\alpha\beta}$. The pair-wise potential used is:

$$V_{\alpha\beta}(r) = 4\epsilon_{\alpha\beta} \left[\frac{\sigma_{\alpha\beta}^{12}}{r^{12}} - \frac{\sigma_{\alpha\beta}^6}{r^6} \right] - V_{cut}(r) \quad (4.1)$$

$$V_{cut}(r) = [(6\sigma_{\alpha\beta}^{12}/r_{c\alpha\beta}^{12}) - (3\sigma_{\alpha\beta}^6/r_{c\alpha\beta}^6)](r/r_{c\alpha\beta})^2 - 7(\sigma_{\alpha\beta}^{12}/r_{c\alpha\beta}^{12}) + 4(\sigma_{\alpha\beta}^6/r_{c\alpha\beta}^6). \quad (4.2)$$

The reduced density is 1.2. For $N = 256$ the temperature range spans $T = 0.39$ to $T = 0.57$, at which T the liquid is equilibrated. Out-of-equilibrium runs are also considered at $T = 0.38$ and $T = 0.40$. Further details are as in [101, 104]. The $N = 10000$ system is studied between $T = 0.377$ and $T = 0.7$. The liquid is not in equilibrium below $T = 0.552$.

2. The 50:50 binary Lennard-Jones liquid studied by Schröder *et al* [108]. The system contains 251 particles of type A and 249 particles of type B interacting via a LJ potential with parameters $\sigma_{BB}/\sigma_{AA} = 5/6$, $\sigma_{AB} = (\sigma_{AA} + \sigma_{BB})/2$, and $\epsilon_{AA} = \epsilon_{AB} = \epsilon_{BB}$. The masses are given by $m_B/m_A = 1/2$. The length of the sample is $L = 7.28\sigma_{AA}$ (reduced density = 1.296) and the potential was cut and shifted at $r_{c\alpha\beta} = 2.5\sigma_{\alpha\beta}$. The form of the potential is the same as above, but with $V_{cut} = 4\epsilon_{\alpha\beta}[\frac{\sigma_{\alpha\beta}^{12}}{r_{c\alpha\beta}^{12}} - \frac{\sigma_{\alpha\beta}^6}{r_{c\alpha\beta}^6}]$. The temperatures range from $T = 0.60$ to $T = 0.69$ and the system is equilibrated at all temperatures. Further details are as in [108].
3. A two dimensional soft sphere liquid with $N = 10000$ particles [133]. The particles interact *via* the potential $V_{\alpha\beta} = \epsilon(\sigma_{\alpha\beta}/r)^{12}$, with parameters $\sigma_{BB}/\sigma_{AA} = 1.4$ (additive diameters) and $m_B/m_A = 2$. The potential is cut and shifted at $r/\sigma_{AA} = 4.5$. The reduced density is 0.8. The temperature range is $T = 0.337$ to $T = 2.54$ and the system

is equilibrated at all temperatures. Further details are as in [133].

4. A two dimensional polydisperse Lennard-Jones liquid [25, 122]. The particle diameters are uniformly distributed between 0.8 to 1.2 of the average value. The number of particles is $N = 990$ and the temperatures $T = 0.4$ to $T = 2.0$ and the system is equilibrated at all temperatures.
5. The Stillinger-Weber model of silicon [103, 119]. Simulated configurations containing $N = 512$ particles are analyzed, at zero pressure, and $T = 1055K, 1070K$ and $1710K$. The Stillinger-Weber potential consists of a two and a three body term. The two body term has the form:

$$v_2(r_{ij}) = \epsilon f_2(r_{ij}/\sigma) \quad (4.3)$$

$$\begin{aligned} f_2 &= A(Br^{-p} - r^{-q})\exp[(r - a)^{-1}], & r < a \\ f_2 &= \mathbf{0}, & r > a \end{aligned} \quad (4.4)$$

Where ϵ and σ are energy and length units and r_{ij} is the inter particle distance between the i^{th} and the j^{th} particles. The cutoff is at $r = a$ beyond which the potential is equal to zero.

The three body term has the following form:

$$v_3(\mathbf{r}_i, \mathbf{r}_j, \mathbf{r}_k) = \epsilon f_3(\mathbf{r}_i/\sigma, \mathbf{r}_j/\sigma, \mathbf{r}_k/\sigma) \quad (4.5)$$

$$f_3(\mathbf{r}_i/\sigma, \mathbf{r}_j/\sigma, \mathbf{r}_k/\sigma) = h(r_{ij}, r_{ik}, \theta_{jik}) \quad (4.6)$$

$$+ h(r_{ji}, r_{jk}, \theta_{ijk}) + h(r_{ki}, r_{kj}, \theta_{ikj})$$

Here θ_{ijk} is the angle between \mathbf{r}_i and \mathbf{r}_j subtended at the vertex i . We then have h given by

$$h(r_{ij}, r_{ik}, \theta_{jik}) = \lambda \exp[\gamma(r_{ij} - a)^{-1} + \gamma(r_{ik} - a)^{-1}][\cos(\theta_{jik} + \frac{1}{3})]^2 \quad (4.7)$$

The parameters defining the model are:

Parameter	values
A	7.049556277
B	0.6022245584
p	4
q	0
a	1.8
λ	21.0
γ	1.20
σ	0.20951 nm
ϵ	50 kcal/mol

The supercooled liquid silicon has been shown [103] recently to exhibit a liquid-liquid phase transition, with the low temperature liquid displaying “strong” character in the fragile-strong classification of the dynamical behaviour of glass forming liquids [4]; fragile liquids display non-Arrhenius temperature dependence of viscosity and relaxation times,

while strong liquids show Arrhenius temperature dependence. Further, strong liquids have been observed to exhibit strong Boson peaks [6]; in simulation studies a manifestation of the Boson peak has been identified [58] as a dip in the intermediate scattering function between the short time (“microscopic”) process and the caging plateau that precedes the alpha relaxation. The system is equilibrated at all temperatures. Further details are given in [103].

6. The BKS model of silica [107,128]. The interatomic potential for BKS Silica is given by

$$V_{ij} = q_i q_j / r_{ij} + A_{ij} \exp[-b_{ij} r_{ij}] - c_{ij} / r_{ij}^6 \quad (4.8)$$

with parameters:

i-j	A_{ij}	b_{ij}	c_{ij}	atomic charges
O-O	1388.7730	2.76000	175.0000	$q_o = -1.2 e$
Si-O	18003.7572	4.87318	133.5381	$q_{si} = 2.4 e$

Simulations of a system containing $N = 336$ atoms (112 silicon and 224 oxygen), in a cubic box of size 18.8 \AA have been studied. Temperatures studied range from $T = 2750K$ to $T = 6100K$. The liquid is equilibrated at all studied temperatures. BKS silica has been shown to display a fragile to strong crossover around $T = 3500K$. [57]. Further details may be found in [107].

For each system we study, we calculate the set of forces between all pairs of particles present. This is straight-forward in all the cases except silicon,

since the interactions are pair-wise additive. What we mean by pair-wise forces in the case of silicon, where two-body and three-body interactions are present, is described below when we present results for silicon.

4.3 Force Distributions

Figure 4.2(a) shows the force distribution for the Kob-Andersen liquid for $N = 10000$ and a range of temperatures. The repulsive as well as attractive forces are shown, with the attractive forces on the negative axis. Focusing on the repulsive forces, it is seen that in all cases, the distribution is exponential. Figure 4.2(b) shows the force distributions for the Kob-Andersen liquid for $N = 256$ and a range of temperatures which includes temperatures below the mode coupling temperature $T_c = 0.435$ [67]. It has been shown recently that the diffusion constant shows a non-Arrhenius to Arrhenius crossover in this system across $T = 0.435$ [12]. In this case also, the repulsive part of the force distribution is seen to be close to exponential. Indeed, for similar temperatures the force distributions for $N = 10000$ and $N = 256$ are very similar, and the $N = 256$ cases have been considered simply to extend the range of temperatures studied. Figure 4.2(c) shows the force distribution for the 50:50 binary Lennard-Jones liquid which also displays exponential repulsive force distribution. The same behaviour is seen in Fig. 4.2(d) for the two dimensional polydisperse LJ liquid. In all cases, the peak at zero force arises from pairs of particles at large separations, which experience weak attractive forces between them.

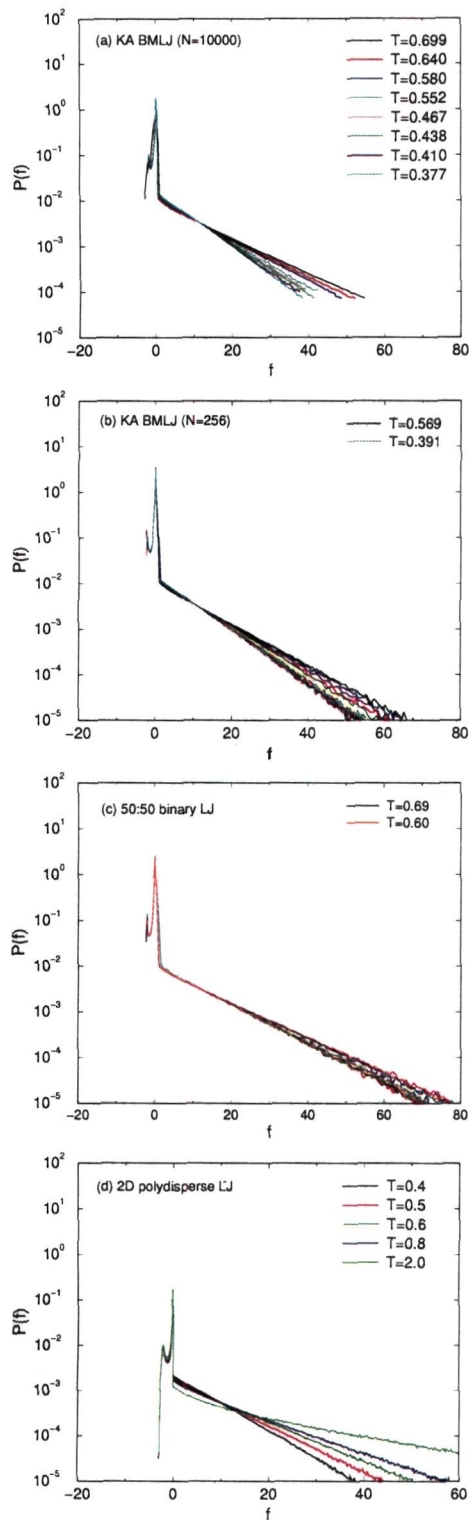


Figure 4.2: Force distribution for (a) A type particles for instantaneous configuration of the Kob-Andersen liquid for $N = 10000$. The liquid is not equilibrated below $T = 0.552$, (b) A type particles for instantaneous configuration of the Kob-Andersen liquid for $N = 256$. (c) A type particles for instantaneous configurations of the 50:50 binary LJ liquid for $N = 500$. (d) Instantaneous configurations of the two dimensional polydisperse LJ liquid.

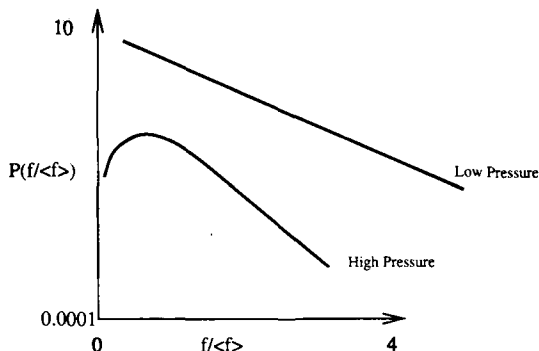


Figure 4.3: A schematic of the force distribution for a granular system at low (100KPa) and high pressures (2.3MPa). The low pressure is unjammed and high pressure is jammed. Note the exponential and gaussian nature of the force distribution in the low and the high pressures respectively.

Next, we consider the force distributions for local energy minimum configurations or inherent structures, obtained by subjecting a sample of liquid configurations to local energy minimization. Energy minimizations are performed using steepest descent or the conjugate gradient method, and the number of configurations analyzed varies from a few tens to a few thousand configurations in the different cases analysed. The stopping criterion for minimization is that the energy change per iteration decreases to less than one part in 10^{12} . Figure 4.4(a) shows the force distribution for the inherent structures of the Kob-Andersen liquid with $N = 10000$. It is seen that the force distribution has a Gaussian form, similar to observations by Makse *et al* [73] for $P(f)$ above a critical value of the stress (Fig 4.3). Since local energy minima are by definition mechanically stable or jammed configurations, the observation of a Gaussian distribution is consistent with expectations based on previous work. Figure 4.4(b) shows the corresponding force distributions for the two dimensional polydisperse system, which also displays Gaussian

force distributions.

While the results shown so far conform to expectations by and large, an interesting exception is the Kob-Andersen liquid at low temperatures for $N = 10000$ where the system is not properly equilibrated, but we nevertheless observe force distributions that are similar to the cases which are well equilibrated. It should be noted that in Ref [88] the glass transition is defined to occur when threshold relaxation time of $\tau = 1000$ (in reduced units) is reached. For all case presented, *e.g.*, in Fig. 4.4(b), our results are for T 's below the effective glass transition as defined by O'Hern *et al.* [88–90] even though our system is in equilibrium. To clarify, we perform additional simulations (both constant energy and constant temperature) for 5 million time steps, quenched from a high temperature initial run, for the Kob-Andersen liquid, $N = 256$, at $T = 0.38$. At this temperature, the system does not equilibrate for runs exceeding a few hundred million time steps, and therefore the system is clearly out of equilibrium in the 5 million time step run. Further, in view of the lack of self averaging indicated in [89], we calculate the force distribution with and without normalizing the forces to the configuration-wise average of the repulsive forces. These distributions are shown in Fig. 4.5. It is seen that the force distributions are exponential in each case. This indicates that lack of self-averaging is not an issue in this instance.

We next consider the two dimensional binary soft sphere liquid, for which the force distributions are shown in Fig. 4.6. In this case, as the temperature is lowered, but with the liquid still in equilibrium, a small force peak is seen to develop, and be clearly visible at the lowest two temperatures. This case provides a second counterexample to expectations, since one sees a finite

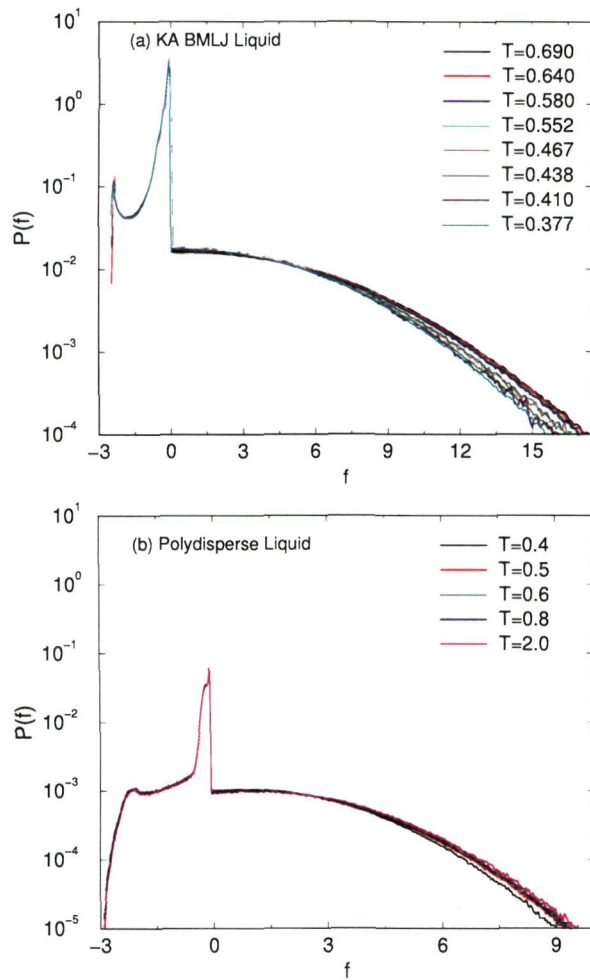


Figure 4.4: Force distribution for (a) A type particles for inherent structure configurations of the Kob-Andersen system for $N = 10000$. (b) Inherent structure configurations of the two dimensional polydisperse LJ liquid.

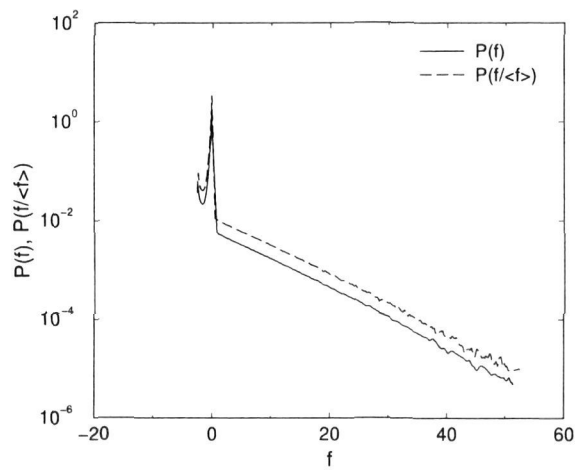


Figure 4.5: Force distribution for A type particles for instantaneous configurations of the out of equilibrium Kob-Andersen liquid, for $N = 256$ and $T = 0.38$. The force distribution is calculated both (a) without normalization ($P(f)$ in figure), and (b) normalizing to the average repulsive force for each configuration ($P(\frac{f}{\langle f \rangle})$) in figure. Data for (b) has been scaled by 7.454 (x axis) to match the range of curve (a) and shifted by 0.656 (y axis) for clarity.

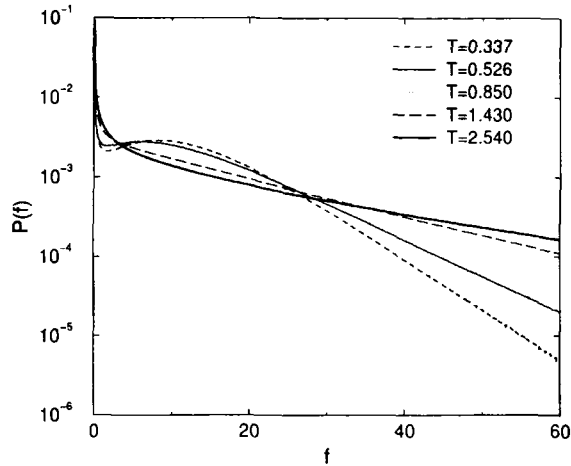


Figure 4.6: Force distribution for instantaneous configurations of the two dimensional binary soft sphere liquid.

force peak appear in a liquid in equilibrium.

From previous results, we expect the binary soft sphere liquid to display “strong” behaviour¹. Such liquids have so far not been analyzed and therefore the possibility that strong liquids exhibit force distributions that differ qualitatively from fragile liquids deserves further exploration. To this end, we consider two liquids for which evidence of strong behaviour exists. The first is liquid silicon. In a recent study [103] of silicon using the Stillinger-Weber potential [119] it has been shown that a liquid-liquid transition exists around

¹Evidence that the 50:50 soft-sphere mixture has some features of a strong liquid comes from three sources. First, the self intermediate scattering function $F_s(k, t)$ shows marked short-time oscillations characteristic of strong liquids [58, 93]. While it is known that the strength of such oscillations is dependent on system size [85], the appearance of such behaviour at all is indicative of strong behaviour. Second, the 50:50 soft-sphere mixture shows marked finite size effects in the alpha relaxation time [65] that is expected for strong liquids [59]. Lastly, the ratio of the T_c of mode-coupling theory [51] to the expected ideal glass transition temperature T_K where an entropy crisis would occur in the mean-field limit [29] is large for the 50:50 soft-sphere mixture compared to the more fragile BMLJ system of Kob and Andersen [30]. This is consistent with strong behaviour on the fragility scale.

$T = 1060K$ and the low temperature phase displays strong behaviour which the high temperature phase displays fragile behaviour at zero pressure. We therefore calculate the force distribution for liquid silicon at $T = 1055K$ (below the transition), $T = 1070K$ (above the transition) and $T = 1710K$ (above the liquid-solid transition). Figures 4.7(a,b,c) show the force distributions at these temperatures.²

In each case, the distribution of nearest neighbor repulsive forces shows a Gaussian character (or a tendency to plateau), and the distribution of all forces shows a small force peak. However, the peak corresponds to neighbors farther away than the first shell, as seen by a comparison with the distribution considering the nearest neighbors alone. Therefore, in this case also, the non-exponential force distribution for small forces (or the appearance of a plateau) does not correspond to a glass transition. Further, the qualitative form of the distribution remains roughly the same (but with a growing exponential regime in the tail of the distribution at higher temperatures) at all temperatures. Thus, a sharp connection with strong behaviour is also not obvious. It is likely that the nature of the distributions is related to the type of interactions that may lead to strong dynamical character in a limited temperature domain. In order to investigate further the role of fragility in determining the nature of the force distributions, we study liquid silica, simulated using the BKS potential [128]. We calculate $P(f)$ for $T = 2750, 3000,$

²In addition to two body interactions, the Stillinger-Weber potential includes a sum over three body terms of the form $U_3(\mathbf{r}_i, \mathbf{r}_j, \mathbf{r}_k)$. The α^{th} component of the total force on a given atom i can be written as,

$$F_{i,\alpha} = - \sum_{j,k} \frac{\partial U_3(\mathbf{r}_i, \mathbf{r}_j, \mathbf{r}_k)}{\partial r_{i,\alpha}} \equiv \sum_j F_{ij,\alpha}$$

where the second step defines what we consider to be “pair-wise” forces between i and j , arising from three body interactions.

3580, 4000, 4700 and 6100K as shown in Fig 4.8 (a,b). BKS silica is known to have a strong to fragile transition at around 3500K [57]. We investigate the $P(f)$ for the repulsive parts *i.e.*, $Si - Si$ and $O - O$ interactions. The force distributions in this case display much richer structure, reflecting the static structure of the liquid. Comparison with the nearest neighbor force distributions reveals that the largest force peak arises from nearest neighbor interactions.

The overall picture that emerges is one that is grossly consistent with that of O'Hern *et al.* [88–90] with some interesting exceptions. We have found that the LJ mixtures do not show a plateau in $P(f)$ at small f even at temperatures where equilibration is no longer possible, while the soft-sphere mixture shows a plateau in the liquid phase, above T_c . While inherent structures always display Gaussian profiles, in accordance with Ref [73, 88–90], the appearance of a plateau in $P(f)$ may not be a sensitive measure of the location of T_g . What can one draw from the results presented in this section? It appears that there is indeed some correlation between the properties of $P(f)$ at small f and the strong-fragile properties of the liquid. In particular, if we confine our discussion to spherical particles where the analogy with granular media is clearer, then we find that the appearance of a plateau at small f occurs in the case of the stronger soft sphere mixture and not in the more fragile LJ liquids.

Silicon and silica are also liquids that display a peak at low repulsive force values, and are systems that may exhibit characteristics of strong liquids. It was noted above, however, that these features persist above the strong-to-fragile crossover temperatures in these systems. Given that the inherent

structures of all systems show peaks in $P(f)$ at small f , while instantaneous configurations may not, a useful correlation between the average number of imaginary modes (in the language of instantaneous normal modes) at a given set of thermodynamic parameters and the low f properties of $P(f)$ may exist. While it may be useful to pursue this connection in future work, we will argue in the next section that $P(f)$ has some fundamental limitations as an indicator of the rheological properties of a glassy system.

4.4 Response to Deformation

In order to investigate other possible connections between mechanical properties of glass forming systems, and their dynamical properties, we study the response of inherent structures to shear deformations, for the Kob-Andersen binary LJ liquid, and the polydisperse Lennard-Jones systems with $N = 110$ particles. Each inherent structure is subjected to a deformation given by $x'_i = x_i + \gamma y_i$, where γ is a strain variable. After such a deformation, the deformed configuration is subjected to energy minimization, and the resulting inherent structure is compared with the initial one. In each case, we determine the smallest value of γ which results in a transition to a new inherent structure. This critical γ is averaged over 1000 inherent structures for each temperature studied.

Figure 4.9(a) shows γ_c for the polydisperse LJ system. While at the high temperatures γ_c is relatively constant, a trend towards larger values is seen at low temperatures, indicating that the inherent structures become more “robust” at low temperatures. A comparison with the average inherent

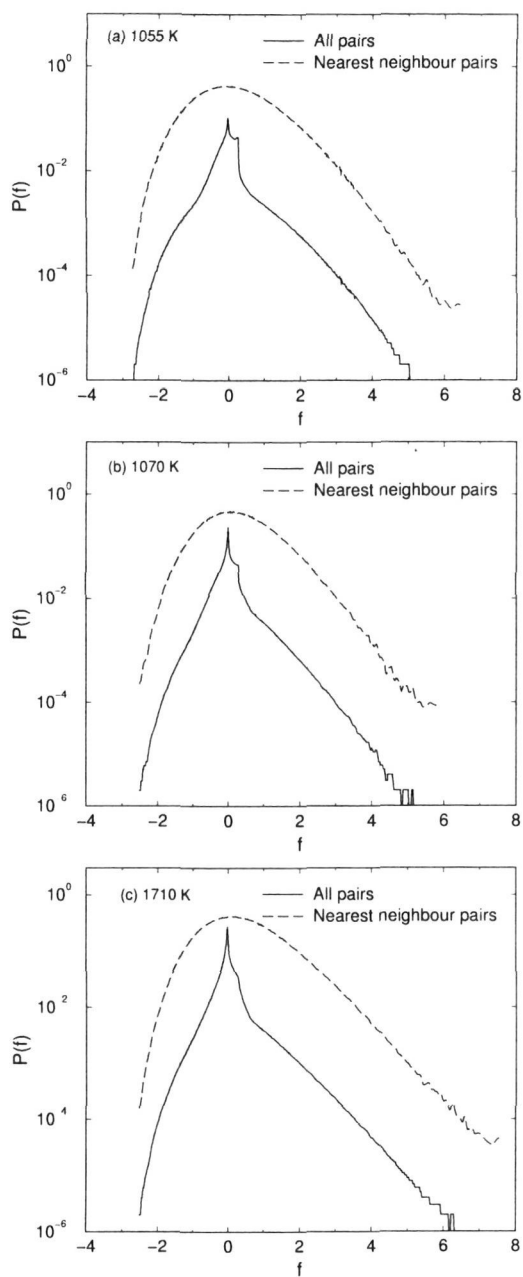


Figure 4.7: Force distribution for liquid Silicon at (a) $T = 1055K$, (b) $T = 1070K$, (c) $T = 1710K$

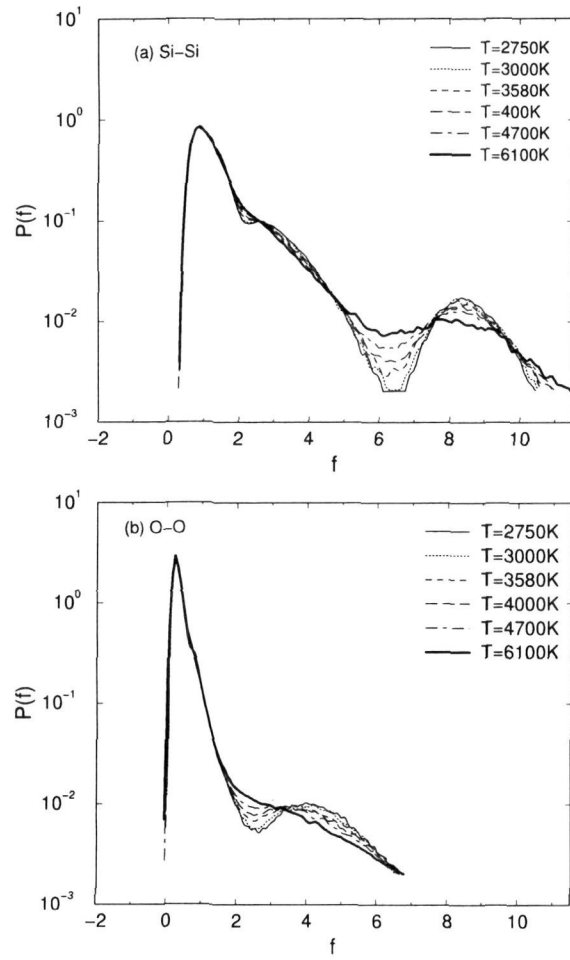


Figure 4.8: Force distribution for silica, considering all pair-wise (a) Si-Si interactions, (b) O-O interactions.

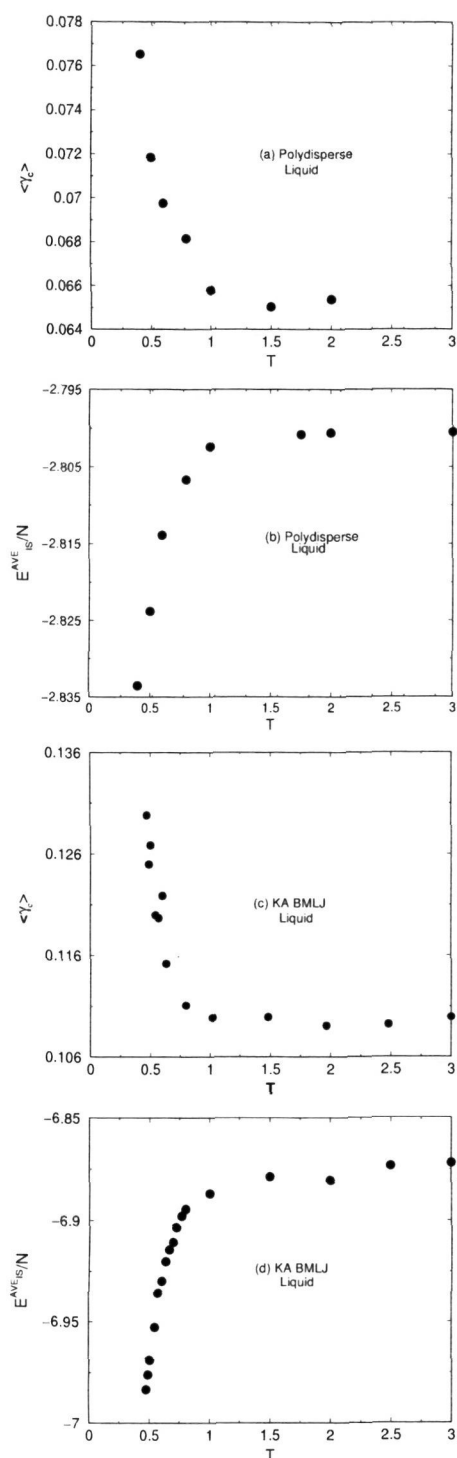


Figure 4.9: (a) Critical shear deformation γ_c vs. temperature for the polydisperse LJ liquid. (b) The average inherent structure energy vs. temperature for the polydisperse LJ liquid. (c) Critical deformation γ_c vs. temperature for the Kob-Andersen liquid. (d) Inherent structure energy vs Temperature for Kob-Andersen liquid for reduced density 1.2.

structure energy *vs.* temperature, shown in Fig. 4.9(b), indicates that the resistance to shear of the inherent structures follows that of the inherent structure energies; in particular, the increase of γ_c is coincident with the onset of a decrease in the inherent structure energies. It has been shown in previous work [101,104] that the progressive decrease of inherent structure energies marks the onset of slow dynamics in the liquid. The resistance to a shear strain deformation of the inherent structures thus also reflects the onset of slow dynamics. Figure 4.9(c) shows γ_c *vs.* temperature for the Kob-Andersen binary liquid, for which the onset temperature has been previously estimated to be $T_o \sim 1.0$ [101,104]. It is clear that for this system as well, the behaviour of γ_c reflects the onset of slow dynamics, and the decrease of average inherent structure energies.

What may be drawn from the results shown in Figs. 4.9(a-d)? The demonstration of a sharp change in the yielding behaviour of the inherent structures sampled below T_o is interesting in its own right. Taken with the results of the previous section, the data presented in Figs. 4.9(a-d) suggest that some care should be taken in attempting to judge changes in mechanical behaviour based on force distributions. *In particular, while the yielding behaviour of the sampled inherent structures show a rather dramatic change near T_o , the force distributions generated from the same inherent structures (the information shown in Figs. 4.2) show only continuous and gradual changes as the temperature is lowered below T_o .*

4.5 Force Networks

In the context of granular materials and models thereof, a quantity of interest have been “force chains” which characterize the distribution of load in these jammed systems [26, 32, 73].

We calculate the force network for inherent structures in the polydisperse LJ liquid at $T = 1.0$, an example of which is shown in Fig. 4.11(a). Given the absence of a directionality to the load (provided in granular materials by gravity), we observe a two dimensional network of forces which are more homogeneous than the corresponding liquid configuration (not shown), consistently with the observation of Makse *et al.* [73].

We next consider transitions between inherent structures and the corresponding changes in particle positions as well as forces. These are shown in Figs. 4.11(b) and 4.11(c) for the same inherent structure transition. The particle displacements and force changes show a clear and predictable correlation, and further, illustrate the spatial extent of rearrangement involved in the inherent structure transition. A more detailed study of such transitions may be valuable in understanding spatially heterogeneous dynamics, and the emergence of a growing length scale of collective particle motions in glass forming liquids. In particular, consideration of changes in the force network may make the task of defining an associated length scale, connected to dynamic heterogeneity, simpler. In an interesting recent study, Wittmer *et al.* have studied force networks and the elastic properties of disordered solids [121, 132]. They have found “soft” elastic regions of a particular average length scale exist in the inherent structure samples, and that these regions are

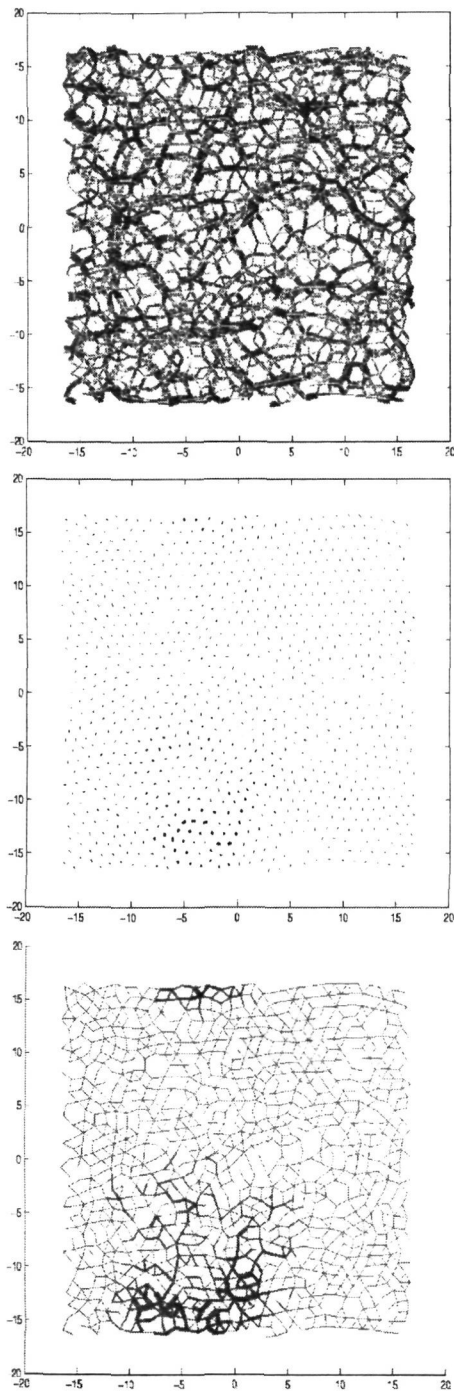


Figure 4.10: (a) Force network in an inherent structure in the polydisperse LJ liquid at $T = 1$. Each line connects two particles and represents the repulsive force between them. The thickness of the lines are proportional to the magnitude of the forces. (b) Particle displacements during an inherent structure transition in the polydisperse LJ liquid at $T = 1.0$. The size of the lines are proportional to the magnitude of the displacement. (c) Changes in forces during an inherent structure transition in the polydisperse LJ liquid at $T = 1.0$. The size of the lines are proportional to the magnitude of the change in the forces.

likely responsible for the anomalous vibrational properties of glasses in the Tera Hertz frequency domain. Wittmer *et al.* did not study the history dependence of this length scale. Our results from this and the previous section suggest that a careful study of the length scale associated with local elasticity and local rupturing of the force network in inherent structures sampled as the temperature is lowered below known crossover temperatures (T_o, T_c) might be useful in understanding dynamical heterogeneity in supercooled liquids and elastic heterogeneity in glasses.

4.6 Discussion and Summary

We have studied [10] the relationship between mechanical properties of glass forming liquids and their dynamical behaviour. First, we studied force distributions in a variety of model liquids and corresponding inherent structures. While most equilibrated atomic liquids display exponential force distributions, and inherent structures display Gaussian distributions, consistent with expectations based on previous work, we have observed some interesting exceptions. The out-of-equilibrium low temperature Kob-Andersen liquid does not show a finite force peak and instead shows an exponential distribution like the equilibrated liquid. Further, we do not find any evidence of a lack of self-averaging in the force distribution. On the other hand, the two dimensional binary soft sphere system displays a finite force peak in equilibrium. This observation, in conjunction with the known “strong” dynamical behaviour of this system, leads us to speculate that the force distributions may look qualitatively different for strong liquids. Silicon and silica, which

show strong behaviour, display features in the force distributions previously attributed to jammed states, and further display considerably richer force distributions than seen in other systems previously. These cases lend support to the idea that force distributions may be correlated with the fragility of the liquids in question. However, the correlation is not entirely clear at present and would require further work to elucidate the precise relationship between fragility and the features seen in $P(f)$.

The behaviour of inherent structures to a shear strain γ , on the other hand, shows a clear connection with the onset of slow dynamics. The exact reason for the observed connection needs to be better understood. Taken together with the gradual dependence of $P(f)$ for inherent structures measured as a function of temperature, the sharp change in the critical value of γ needed to melt an inherent structure implies that $P(f)$ alone cannot be sensitive to the yielding properties of glasses themselves, even if the transition from a liquid to a glass might be grossly indicated by the behaviour of $P(f)$ at small f .

A study of force networks and force changes during inherent structure transitions has been presented here. A detailed study of such behaviour may be useful in understanding spatially heterogeneous dynamics and length scales relevant to the slow of dynamics in glass forming liquids, as well as elastic heterogeneity in glasses.

Chapter 5

Limits of a Liquid: Ideal Glass Transition and the Spinodal Line

5.1 Introduction

A liquid has two extreme limits of existence. When the liquid is brought to quasi equilibrium below its freezing temperature by avoiding crystallization it is said to be in the supercooled phase. A liquid cannot remain in this phase as we keep cooling it further. It turns to a glass at a temperature depending on its cooling rate. Faster the cooling rate higher the temperature of glass transition. If we were to cool the liquid infinitesimally slowly, a thermodynamic description would predict the liquid to become a glass at the Kauzmann temperature. This temperature marks the lowest temperature limit wherein the liquid remains a liquid. The other extreme is when we heat

the liquid high enough that it converts to gas. The metastable liquid whose temperature is above the liquid boiling point, is called a superheated liquid. This metastable liquid has its limit of stability at the liquid-gas spinodal point. In mean field theory, beyond the spinodal point the compressibility becomes negative indicating thermodynamic instability. The Kauzmann temperature and the liquid gas spinodal point define two extreme limits of existence of a liquid for temperature. Figure 5.1 (a,b) we have a schematic picture of the van der Waals equation of state in the pressure-density (P vs ρ) plane for temperatures above and below the critical temperature (T_c). The spinodal points are defined as points where $\frac{\partial P}{\partial \rho} = 0$, beyond which the superheated liquid will become unstable and depending on the ensemble we may have a phase separation or conversion to gas. Indicated in Figure 5.1 (c) is the scenario of entropy crisis wherein the configurational entropy becomes zero as we cool the liquid to the Kauzmann temperature. ΔS is the configurational entropy. At low temperatures, the configurational entropy (defined in section 1.3) can be approximated by the difference of entropy of the liquid and the corresponding crystal at the same temperature. At the Kauzmann temperature (T_K) the supercooled liquid transforms to an *ideal glass*. Indicated in Figure 5.1 (d) is the density dependence of the Kauzmann temperature, which we call the *ideal glass line*. An interesting question to ask is, do the locus of the spinodal points and the ideal glass transition line meet at a finite temperature, leading to the possibility of a glass-gas transition? This question was answered using computer simulation and the inherent structure approach by Sastry [100] for a model liquid. It was shown that the

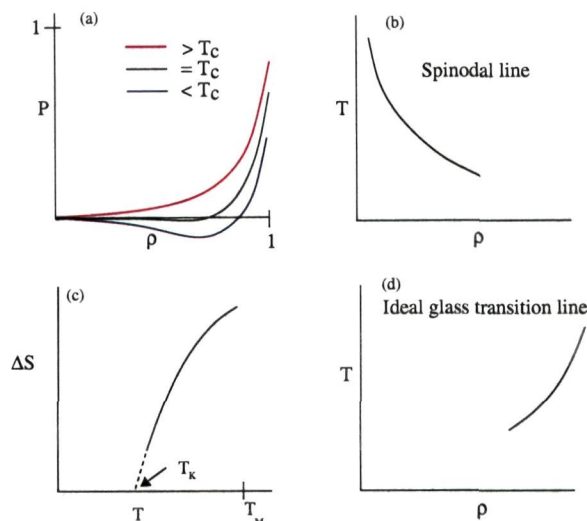


Figure 5.1: (a) The Pressure vs density isotherms for a typical mean field model like the van der Waals gas. The spinodal points are the points where $\frac{\partial P}{\partial \rho} = 0$. (b) Spinodal densities as a function of temperature. (c) The configurational entropy ΔS becomes zero at the Kauzmann temperature T_K , T_M indicates the melting temperature. (d) Dependence of T_K on the density.

locus points describing these two limits intersect at a finite temperature, indicating a possibility of an amorphous to gas transition at low temperatures. It was also shown that the inherent structure pressure *vs* density display a van der Waals type loop indicating the lowest density for glass formation now known as the *Sastry density*.

Here [11] we study this scenario in the context of liquid state theory and a thermodynamic theory for the glass transition proposed by Mezard and Parisi [77]. We begin by describing what was done earlier [100] using computer simulation. We then introduce elements of liquid state theory to estimate the structure of the liquid and hence all the related thermodynamic quantities. We will then describe how the liquid gas spinodal is estimated. We then go on describe the calculation of the Kauzmann temperature using

the Mezard and Parisi scheme [77].

5.2 Prior Work

We describe here briefly how the above mentioned problem was handled [100] using computational means. The model studied earlier was the KABMLJ liquid of 204 of A particles and 52 B particles. We describe briefly first how the spinodal line is calculated and then we describe how the glass transition line is calculated.

5.2.1 Spinodal Line

To estimate the spinodal line [100] a restricted ensemble Monte Carlo (REMC) was performed for eight temperatures and ten densities. The run lengths between 3×10^5 to 1.8×10^6 time steps were performed. In the restricted ensemble Monte Carlo the system is divided into cells and the fluctuations of density in each cell is restricted. Isotherms were calculated to display van der Waals loop in order to calculate the liquid gas spinodal. P vs ρ from these curves were fit to cubic polynomials and further compressibility $\kappa (=1/\rho \frac{\partial \rho}{\partial P})$ was calculated from MD simulation. The inverse of compressibility κ^{-1} was calculated and the density at which it vanishes (on polynomial extrapolation) indicates the liquid gas spinodal point, which compares well with the REMC simulation.

Further an empirical equation of state was constructed from MD simulation. In order to do this we need to calculate the free energy of the system. The absolute free energy which is of interest is the sum of the ideal gas free

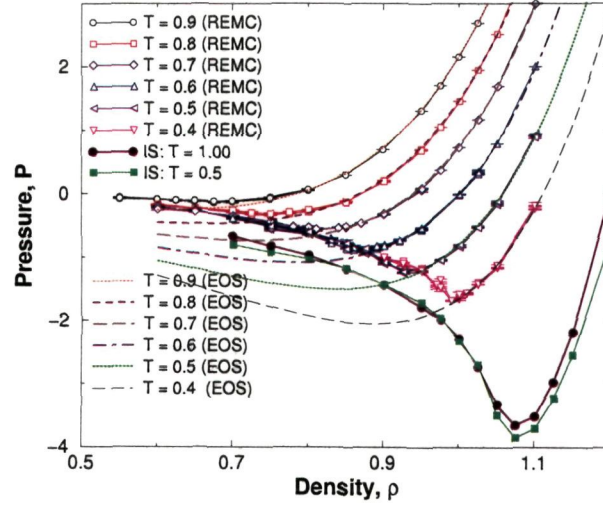


Figure 5.2: Pressure *vs* density Isotherms from REMC points connected with curves. The continuous curves display empirical equation of state (EOS). Also shown are the equation of state obtained for the Inherent structures.

energy A_{id} and the excess free energy A_{ex} ,

$$A(\rho, T) = A_{id}(\rho, T) + A_{ex}(\rho, T) \quad (5.1)$$

The ideal gas component of the free energy is given by

$$A_{id}(\rho, T) = N [3\ln(\lambda) + \ln(\rho) - 1] \quad (5.2)$$

λ is the De Broglie wave length and $\beta = 1/k_B T$. The excess free energy at a reference temperature T_r can be integrated from the pressure equation of state.

$$\beta_r A_{ex}(\rho, T_r) = \beta_r A_{ex}^0(0, T_r) + N \int_0^\rho \frac{d\rho'}{\rho'} \left[\frac{\beta_r P}{\rho'} - 1 \right] \quad (5.3)$$

Where $\beta_r A_{ex}^0(0, T_r)$ arises from mixing entropy at zero density, which is given by,

$$\beta_r A(0, T_r) = -\ln \left(\frac{N!}{N_A! N_B!} \right) \quad (5.4)$$

The excess free energy at the reference temperature was fit to fifth order polynomial in ρ and the free energy at any temperature is calculated through the following integral.

$$\beta A_{ex}(\rho, \beta) = \beta A_{ex}(\rho, \beta_r) + \int_{\beta_r}^{\beta} E(\rho, \beta') d\beta' \quad (5.5)$$

It is difficult to do molecular dynamics simulations near the spinodal points. The energy $E(\rho, \beta)$ near the spinodal region is predicted using a fit to data away from the spinodal point. $E(\rho, \beta)$ was fit to the form $E(\rho, \beta)/N = E_0(\rho) + E_1(\rho)T^{E_2(\rho)}$, where E_0, E_1, E_2 are fit to polynomials in ρ (for details see [100]). We then get one more independent estimate of the spinodal point via the relation,

$$\frac{\partial P(\rho, T)}{\partial \rho} = \frac{\partial}{\partial \rho} \frac{\rho^2}{N} \left(\frac{\partial A(\rho, T)}{\partial \rho} \right)_T = 0 \quad (5.6)$$

Shown in Fig 5.2 are the isotherms and the spinodal points calculated through the two different methods.

5.2.2 Glass Transition Line

Two estimates of the ideal glass transition were obtained via (i) Vogel-Fulcher-Tammann (VFT) [44, 120, 130] equation (discussed in section 1.1.2)

and (ii) vanishing of configurational entropy. The diffusivity $D(\rho, T)$ is calculated as a function of density and temperature using MD. The diffusivity of the A type particles are then fit to the VFT equation

$$D(\rho, T) = D_o(\rho) \exp \left[\frac{A(\rho)}{T - T_o(\rho)} \right] \quad (5.7)$$

$T_o(\rho)$ is estimated, which happens to be the lower estimate of the laboratory glass transition temperature. $T_o(\rho)$ is then calculated for various densities.

Thermodynamic estimate of the Ideal glass transition involves calculating the configurational entropy. Consider the partition function of the liquid.

$$Q_N(\rho, T) = \lambda^{-3N} \frac{1}{N_A! N_B!} \int dr^N \exp(\beta\Phi) \quad (5.8)$$

This partition function can be written in terms of contribution from the inherent structures in the following manner,

$$Q_N(\rho, T) = \sum_k \exp(-\beta\Phi_k) \lambda^{-3N} \int dr^N \exp[\beta(\Phi - \Phi_k)] \quad (5.9)$$

Here Φ_k is the potential energy of the minima. We further write

$$Q_N(\rho, T) = \int d\Phi_k \Omega(\Phi_k) \exp[-\beta(\Phi_k + Nf_{basin}(\Phi_k, T))] \quad (5.10)$$

$\Omega(\Phi_k)$ is the number of inherent structures of energy Φ_k .

The partition function can further be written in terms of the configurational entropy $S_c = k_B \ln \Omega$,

$$Q_N(\rho, T) = \int d\Phi_k \exp[-\beta(\Phi_k + N f_{basin}(\Phi_k, T) - T S_c)] \quad (5.11)$$

The basin free energy is given by

$$\begin{aligned} \beta f_{basin} &= k_B T \sum_i \log \left(\frac{h\nu_i}{k_B T} \right) \\ \beta f_{basin} &= \beta f_{therm} + \beta f_{vib} \end{aligned} \quad (5.12)$$

λ_i are eigen values of the Hessian matrix of the inherent structures. The vibrational part is a slowly varying function of temperature. The vibrational free energy βf_{vib} was fit to the form $f_o(\rho) + \frac{f_1(\rho)}{T^2}$ with 1000 inherent structure below $T = 1$ and 100 inherent structure above $T = 1$. The total entropy of the liquid S was calculated as a function of density and temperature. Thus the configurational entropy is calculated as

$$S_c(\rho, T) = S(\rho, T) - S_{basin}(\rho, T) \quad (5.13)$$

The ideal glass temperature T_K is identified as

$$S_c(\rho, T_K) = 0 \quad (5.14)$$

Shown in Fig 5.3 are the glass transition line estimated via VFT, thermodynamic integration and the spinodal lines via REMC, thermodynamic integration and the compressibility inverse. The ideal glass transition line

and the spinodal line intersect at a finite temperature. The intersection density is now known as the *Sastry density*.

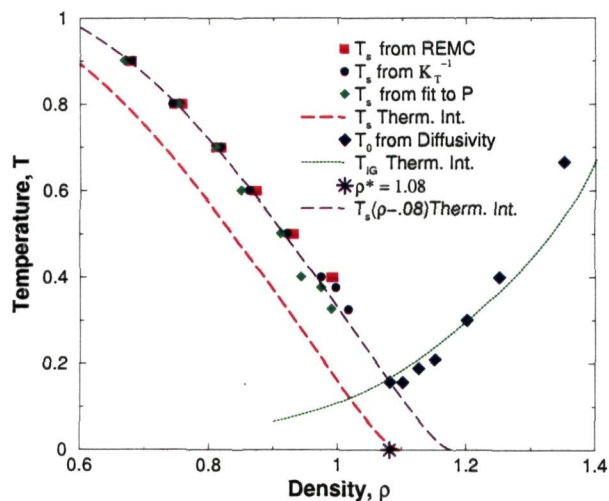


Figure 5.3: Pressure vs density Isotherms from REMC points connected with curves. The spinodals are calculated using restricted ensemble Monte Carlo (REMC), Inverse compressibility, fit to the pressure and thermodynamic integration. The ideal glass transition line is calculated using VFT and thermodynamic integration. From [100].

5.3 Elements of Liquid State Theory

Before we describe how we go about solving this problem using semi analytic and numerical schemes, We introduce key elements of liquid state theory which will be extensively used from now on.

Consider N particles in a volume V and temperature T . Let $P^{(N)}(\mathbf{r}_1, \mathbf{r}_2 \dots \mathbf{r}_N)$ be the probability that particles $1 \dots N$ are existing in a volume element

$\mathbf{dr}_1 \dots \mathbf{dr}_N$. This probability is then given by

$$P^{(N)}(\mathbf{r}_1, \mathbf{r}_2 \dots \mathbf{r}_N) = \frac{\exp[-\beta U_N(\mathbf{r}_1, \mathbf{r}_2 \dots \mathbf{r}_N)]}{Z_N} \quad (5.15)$$

Here Z_N is the configurational part of the partition function defined as

$$Z_N = \int \exp[-\beta U_N] \mathbf{dr}_1 \mathbf{dr}_2 \dots \mathbf{dr}_N \quad (5.16)$$

and U_N is the potential energy of the system, for any $n < N$

$$P^{(N)}(\mathbf{r}_1, \mathbf{r}_2 \dots \mathbf{r}_n) = \frac{\int \exp[-\beta U_N] \mathbf{dr}_{n+1} \dots \mathbf{dr}_N}{Z_N} \quad (5.17)$$

If we assume the molecules to be identical, the probability that the molecules are at $r_1 \dots r_N$ is given by,

$$\rho^{(n)}(\mathbf{r}_1 \dots \mathbf{r}_n) = \frac{N!}{(N-n)!} P^{(n)}(\mathbf{r}_1 \dots \mathbf{r}_n) \quad (5.18)$$

The bulk density ρ is defined as

$$\frac{1}{V} \int \rho^{(1)}(\mathbf{r}_1) \mathbf{dr}_1 = \rho \quad (5.19)$$

We define a correlation function such that

$$\rho^{(n)}(\mathbf{r}_1 \dots \mathbf{r}_n) = \rho^n g^{(n)}(\mathbf{r}_1 \dots \mathbf{r}_n) \quad (5.20)$$

We thus have

$$g^{(n)}(\mathbf{r}_1, \dots, \mathbf{r}_n) = \frac{V^n}{N^n} \frac{N!}{(N-n)!} \frac{1}{Z_N} \int \exp[-\beta U_N] d\mathbf{r}_{n+1} \dots d\mathbf{r}_N \quad (5.21)$$

The function $g^{(2)}(\mathbf{r}_1, \mathbf{r}_2)$ is of special interest as it can be determined experimentally and also a great deal of liquid state theory deals with various approximate methods to determine it. We will discuss in brief how one obtains the pair correlation function $g^{(2)}(\mathbf{r}_1, \mathbf{r}_2)$ or simply $g(r_{12})$ through theoretical means. We define the $h(r_{12})$ through the following equation.

$$h(r_{12}) = g(r_{12}) - 1 \quad (5.22)$$

The motivation for this definition is that it is Fourier transformable unlike $g(r_{12})$. It measures the total influence of molecule 1 on molecule 2 at a distance of r_{12} . It was proposed by Orenstien and Zernike that $h(r_{12})$ would have two parts

- The direct part which we call $c(r_{12})$, which arises due to the direct influence of molecule 1 on molecule 2, which we will call the direct correlation function.
- The indirect part, the amount molecule 1 influences molecule 2 via other molecules. It was proposed that the above definition of the direct correlation function captured the indirect influence in the form,

$$\rho \int c(r_{13}) h(r_{23}) dr_3 \quad (5.23)$$

The Ornstein-Zernike (OZ) equation is thus,

$$h(r_{12}) = c(r_{12}) + \rho \int c(r_{13})h(r_{23})dr_3 \quad (5.24)$$

This equation requires a closure in order to solve for the pair correlation function. There are various approximations to solve the above integral equation. The important ones which are required further are dealt with in this section. The direct correlation function is short ranged. We introduce a function $y(r)$ relating the pair correlation as,

$$g(r) = \exp[-\beta v(r)]y(r) \quad (5.25)$$

outside the range of the potential $g(r)$ and $y(r)$ would be the same. In order to obtain the short range function $c(r)$ we try out the following approximation

$$c(r) = g(r) - y(r) \quad (5.26)$$

This approximation is known as the *Percus Yevick closure*. On combining this with the OZ equation we have the *Percus Yevick equation* (PY). PY equation has been the most successful approximation for the first order integral equation for short range potentials. It has wide variety of applications especially for hard sphere systems. Yet another approximation for $c(r)$ is

$$y(r) = \exp[h(r) - c(r)] \quad (5.27)$$

This approximation is known as the *hypernetted chain closure* (HNC). Along

with the OZ equation it is known as the *HNC equation*. Another way to solve the OZ equation is by splitting the potential, into the *reference* part $v_1(r)$ and the *perturbation* part $v_2(r)$, using a projector P_1 and its complement $P_2 = 1 - P_1$, at the position of the potential minimum r_m .

$$v_1(r) = P_1 v(r) = v(r) - v(r_m) \quad r \leq r_m$$

$$v_1(r) = P_1 v(r) = 0 \quad r \geq r_m$$

$$v_2(r) = P_2 v(r) = v(r_m) \quad r \leq r_m$$

$$v_2(r) = P_2 v(r) = v(r) \quad r \geq r_m$$

(5.28)

The closure for the *soft core mean spherical approximation* (SMSA) reads.

$$g(r) = \exp[-\beta v_1(r)] (1 + h(r) - c(r) - \beta v_2(r)) \quad (5.29)$$

HNC is generally good to describe long range potentials and PY has been successful in describing short range potentials as well as hard sphere systems. A generic problem with all liquid state theories (PY and HNC inclusive), is the so called thermodynamic inconsistency, *i.e.*, equation of state derived through the virial and compressibility routes are different. Rogers and Young [95] resolved this issue by constructing an interpolation function, which uses

a switching parameter which can interpolate the closure between PY and HNC. The interpolation parameter is found such that the thermodynamic inconsistency vanishes. We discuss in detail later, one other interpolation function between SMSA and HNC which yield very good pressure density van der Waals loop for the case of KABMLJ liquid.

5.4 Treatment of the Integral Equations

Using the Eq 5.27 and Eq 5.25 we can write the direct correlation function for the HNC in the following manner

$$c(r) = \exp[-\beta v(r) + \gamma(r)] - \gamma(r) - 1 \quad (5.30)$$

where the function $\gamma(r)$ is defined as,

$$\gamma(r) = h(r) - c(r) \quad (5.31)$$

Where the direct correlation function $c(r)$ and the pair correlation function $g(r)(= h(r) + 1)$ are related through the OZ relation

$$h(r) - c(r) = \rho \int d\mathbf{r}' c(|\mathbf{r} - \mathbf{r}'|) h(|\mathbf{r}'|) \quad (5.32)$$

The procedure to solve the HNC with the OZ closure is as follows. We divide the real space range $|r|$ into N equal parts. The mesh points are labeled by $r_i = i\delta r$, i ranges from 1 to N . All other functions (eg., $\gamma_i = \gamma(r_i)$) are

evaluated at these mesh points. We then define following Fourier transforms.

$$c(k) = \int \mathbf{d}\mathbf{r} \exp(i\mathbf{k}\cdot\mathbf{r})c(r) \quad (5.33)$$

$$\gamma(k) = \int \mathbf{d}\mathbf{r} \exp(i\mathbf{k}\cdot\mathbf{r})\gamma(r) \quad (5.34)$$

Our motivation to work with the Fourier transforms becomes apparent if we notice that the OZ equation (Eq. 5.32) involves a convolution. Using the convolution theorem we could write the OZ equation in the following simple manner in the Fourier space,

$$c(k) = h(k) - \rho h(k)c(k) \quad (5.35)$$

Thus $\gamma(k)$ from Eq 5.31 and Eq. 5.34 is

$$\gamma(k) = \rho \frac{c^2(k)}{1 - \rho c(k)} \quad (5.36)$$

Since we intend to numerically solve these equations, we discretized the equations in the real (index i) and the k space (index j) in following manner.

$$c(r_i) = \exp[-\beta v(r_i) + \gamma(r_i)] - \gamma(r_i) - 1 \quad (5.37)$$

$$c(k_j) = (4\pi\delta r/k_j) \sum_{i=1}^{(N/2)-1} r_i \sin(k_j r_i) c(r_i) \quad (5.38)$$

$$\gamma(k_j) = \rho c^2(k_j) / [1 - \rho c(k_j)] \quad (5.39)$$

$$\gamma(r_i) = (\delta k / 2\pi^2 r_i) \sum_{j=1}^{(N/2)-1} k_j \sin(k_j r_i) \gamma(k_j) \quad (5.40)$$

$$r_i = i \delta r_i \quad (5.41)$$

$$k_j = 2\pi j / N \delta r \quad (5.42)$$

We will now use these equations to describe the algorithm we use to solve these equations.

5.4.1 Computational Details

The algorithm in use is the traditional form of solving the HNC equation with OZ closure. Our aim is to estimate the pair correlation function $g(r)$ for a given state point. We start with trial solutions at low density and high temperature limit. The solutions to these conditions would be the ideal gas $g(r)$. We estimate this $g(r)$ by setting $\gamma(r)$ to zero and using the HNC equation (Eq. 5.37) to obtain the direct correlation function $c(r)$. The Fourier transform of the direct correlation is calculated (Eq. 5.38). We then obtain the new $\gamma(k)$ using Eq 5.39 in the k space (OZ closure). We then inverse Fourier transforms to the real space to obtain $\gamma(r)$ using Eq 5.40. We then estimate $g(r)$ using the discretized form of Eq. 5.31. We continue this process until the difference in the pair correlation function between successive iterations becomes smaller than a tolerance of 10^{-10} *i.e.*, $\sum_i |g_{n+1}(r_i) - g_n(r_i)|^2 < 10^{-10}$, where n and $n + 1$ are the iteration numbers, and r_i , is the i^{th} radial mesh point. We then slightly decrement the temperature until the $g(r)$ of the

required temperature is obtained. We further follow the process while incrementing the density, until the $g(r)$ for the right temperature and density is obtained. We derive now in detail the equations involved for the KABMLJ liquid. For KABMLJ pure HNC over estimates the liquid gas phase separation temperature, whereas the SMSA underestimates estimates it [30]. For this reason we use the Zerah Hansen approach [134] in which is an interpolation between SMSA and HNC. For the binary system the direct correlation function (OZ equation) is given by,

$$h_{ab}(k) = c_{ab}(k) + \sum_{i=a,b} \rho_i c_{ai}(k) h_{ib}(k) \quad (5.43)$$

We then have,

$$\gamma_{ab}(r) = h_{ab}(r) - c_{ab}(r) \quad (5.44)$$

Using Eq. 5.44 in Eq. 5.43 we have,

$$\gamma_{ab}(k) = \sum_{i=a,b} \rho_i c_{ai}(k) (c_{ib}(k) + \gamma_{ib}(k)) \quad (5.45)$$

We then solve for γ_{aa} , γ_{ab} , γ_{ba} , γ_{bb} . The Zerah Hansen closure is of the form

$$c^a c^b \rho^2 g_{ab}(r) = \exp(-\beta V_R^{ab}(r)) \times \left(1 + \frac{\exp[f^{ab}(r) (\gamma^{ab}(r) - \beta V_A^{ab}(r))] - 1}{f^{ab}(r)} \right) \quad (5.46)$$

where V_R and V_A are given by

$$V_R = \begin{cases} V(r) - V_{min} & r \leq r_{min} \\ 0 & r \geq r_{min} \end{cases}$$

$$V_A = \begin{cases} V_{min} & r \leq r_{min} \\ V(r) & r \geq r_{min} \end{cases} \quad (5.47)$$

c^a and c^b are the concentrations of the species a and b . f is the interpolation function which interpolates between SMSA and HNC approximation.

$$f = 1 - \exp\left[-\frac{r}{\sigma_{ab}\alpha}\right] \quad (5.48)$$

α is switch parameter from HNC to SMSA. In the limit of $\alpha \rightarrow \infty$ we have SMSA and HNC in the limit $\alpha \rightarrow 0$.

5.4.2 Estimate of Switching Parameter

The parameter α , which switches the relation between HNC and SMSA; is both a function of density as well as temperature. We propose a fit for α as

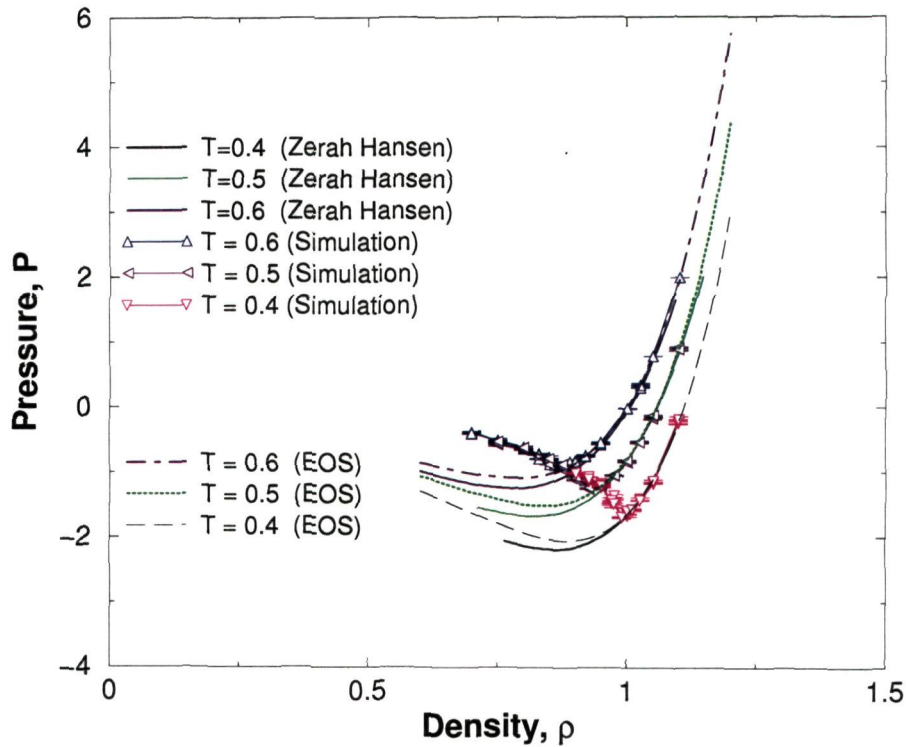


Figure 5.4: Comparison of Pressure vs Temperature Isotherms from the Zerah Hansen scheme and equation of state (EOS) obtained from MD simulation. Isotherms considered are for $T = 0.4, 0.5$ and 0.6 .

a function of temperature and density. The way to choose α in general is through the thermodynamic consistency. As discussed earlier what we mean by thermodynamic consistency is that the thermodynamic equation of state obtained from the virial route or the compressibility route should match. The ZH scheme was originally proposed [134] with success to solve the problem of thermodynamic inconsistency for the Lennard Jones potential for HNC/PY, this scheme does not yield an α which results in thermodynamic inconsistency for the KABMLJ. Though it would be desirable to have such a scheme for the KABMLJ, it is not of primary interest to us. In this project we are satisfied

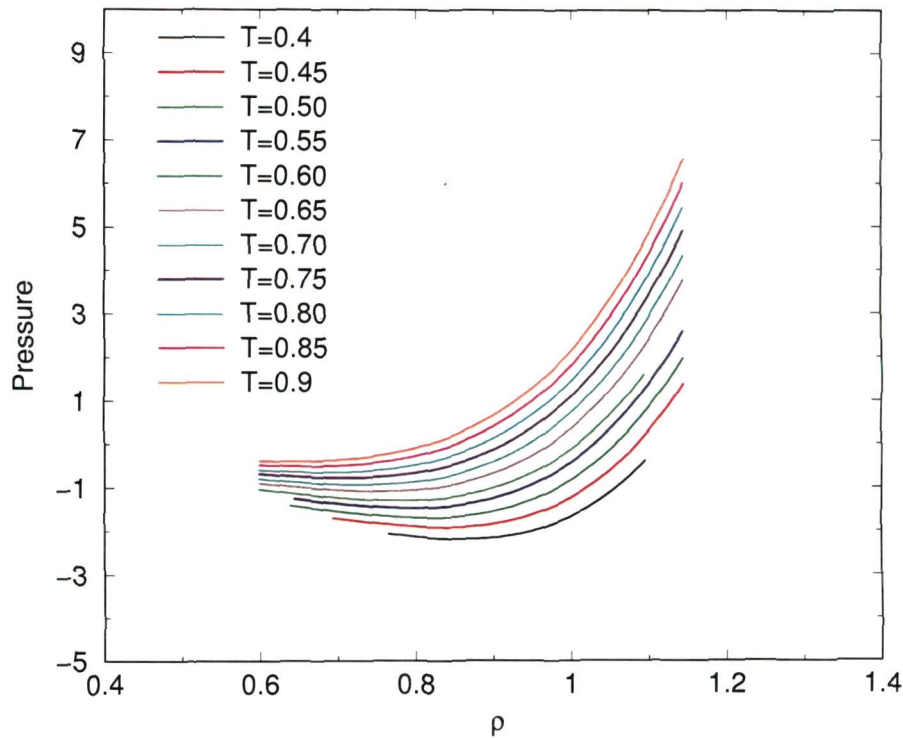


Figure 5.5: Pressure vs density isotherms for the temperature range $T = 0.9 - 0.4$. These calculations have been done using Zerah Hansen scheme.

with an α which yields pressures and temperatures that match simulation. We are interested in getting the spinodals and the entropy (later section), for which we need to have good estimates of the pressure and energy. In order to get a fit for α as a function of temperature and density we compare energy and pressure from molecular dynamics simulation to the pressure and energy from the Zerah-Hansen scheme for various α . Tabulated in tables 5.1-5.12 are the pressures and energy calculated for various values of α for three different temperatures for densities 1.0, 1.1, 1.15, 1.2 and 1.25. The error estimate between the simulation and the ZH equations for the pressure and energy (Shown in Fig 5.6) are studied as a function of α for selected

ρ	β	pressure	error (%)	energy	error (%)	α
1.1	1.0	5.732041	0	-5.218465	0	MD
1.1	1.0	6.458	12.66	-5.124	-1.80	2.431
1.1	1.0	6.384	11.37	-5.134	-1.60	2.586
1.1	1.0	6.316	10.19	-5.144	-1.42	2.741
1.1	1.0	6.196	8.10	-5.160	-1.10	3.051
1.1	1.0	6.094	6.32	-5.175	-0.82	3.362
1.1	1.0	5.896	2.86	-5.202	-0.299	4.123
1.1	1.0	5.864	2.31	-5.207	-0.21	4.270
1.1	1.0	5.731	-0.0143	-5.225	0.1415	5.000
1.1	1.0	5.707	-0.424	-5.229	0.203	5.150

Table 5.1: Pressure and temperature for various α for inverse temperature $\beta = 1.0$ and density $\rho = 1.1$ for the KABMLJ. Errors are relative to the MD simulation (whose pressure and temperature are indicated in the first row). The α that yields the lowest error for **both** pressure and temperature is chosen for the linear fit.

cases. The α which gives minimum errors for the energy and pressure are different. We choose an optimum α , which minimizes the errors in both these parameters. The energy is found not to be so sensitive to α but the pressure is. The optimum $\alpha(\rho, \beta)$ is nonlinear in ρ and β . Since the energy is not very sensitive to α , we try a simple linear fit to ρ and β to reproduce the simulation results. Coefficients in the linear relation are further tuned by inspection so that the pressures away from the spinodal points match the simulation well. We find the form of $\alpha = 11.17 - 11.17\rho + 6.65\beta$, to be a reasonable fit for the densities studied here. We compare the isotherms from this scheme to the isotherms obtained from equation of state for temperatures $T = 0.4, 0.5, 0.6$ (See Fig.5.4). These equation of states were obtained from [100]. We then calculate isotherms for reduced temperature $T = 0.4 - 0.9$. (See Fig. 5.5). The spinodal points are finally obtained from the condition $\frac{\partial P}{\partial \rho} = 0$.

ρ	β	pressure	error (%)	energy	error (%)	α
1.1	1.25	3.943859	0	-5.488472	0	MD
1.1	1.25	4.627	17.32	-5.390	-1.638	2.689
1.1	1.25	4.552	15.43	-5.4058	-1.455	2.887
1.1	1.25	4.485	13.72	-5.417	-1.29	3.086
1.1	1.25	4.368	10.76	-5.433	-1.00	3.482
1.1	1.25	4.270	8.28	-5.446	-0.76	3.879
1.1	1.25	4.064	3.05	-5.473	-0.26	5.0
1.1	1.25	3.958	0.377	-5.488	-0.0078	5.8
1.1	1.25	3.947	0.0858	-5.489	0.020	5.9
1.1	1.25	3.936	-0.197	-5.491	0.046	6.0
1.1	1.25	3.925	-0.47	-5.492	0.071	6.1

Table 5.2: Pressure and temperature for various α for inverse temperature $\beta = 1.25$ and density $\rho = 1.1$ for the KABMLJ. Errors are relative to the MD simulation (whose pressure and temperature are indicated in the first row). The α that yields the lowest error for **both** pressure and temperature is chosen for the linear fit.

ρ	β	pressure	error (%)	energy	error (%)	α
1.1	1.65	1.947087	0	-5.790953	0	MD
1.1	1.65	2.673	37.31	-5.692	-1.702	3.103
1.1	1.65	2.600	33.57	-5.701	-1.54	3.370
1.1	1.65	2.536	30.25	-5.709	-1.40	3.637
1.1	1.65	2.427	24.64	-5.723	-1.168	4.172
1.1	1.65	2.338	20.08	-5.734	-0.97	4.706
1.1	1.65	2.178	11.88	-5.754	-0.63	6.000
1.1	1.65	2.114	8.58	-5.762	-0.492	6.700
1.1	1.65	2.090	7.35	-5.765	-0.440	7.000
1.1	1.65	1.992	2.31	-5.777	-0.229	8.500
1.1	1.65	1.966	0.972	-5.788	-0.173	9.000
1.1	1.65	1.953	0.349	-5.782	-0.147	9.250
1.1	1.65	1.942	-0.245	-5.783	-0.122	9.500
1.1	1.65	1.920	-1.35	-5.786	-0.075	10.000

Table 5.3: Pressure and temperature for various α for inverse temperature $\beta = 1.65$ and density $\rho = 1.1$ for the KABMLJ. Errors are relative to the MD simulation (whose pressure and temperature are indicated in the first row). The α that yields the lowest error for **both** pressure and temperature is chosen for the linear fit.

ρ	β	pressure	error (%)	energy	error (%)	α
1.15	1.10	6.862516	0	-5.459717	0	MD
1.15	1.1	6.979	1.7	-5.454	-0.0871	4.55
1.15	1.1	6.945	1.20	-5.459	0.0011	4.70
1.15	1.1	6.923	0.88	-5.462	0.057	4.80
1.15	1.1	6.882	0.28	-5.468	0.16	5.0
1.15	1.1	6.872	0.14	-5.470	0.189	5.05
1.15	1.1	6.862	-0.002	-5.471	0.21	5.10
1.15	1.1	6.852	-0.14	-5.472	0.23	5.15
1.15	1.1	7.243	5.54	-5.4157	0.804	5.20

Table 5.4: Pressure and temperature for various α for inverse temperature $\beta = 1.1$ and density $\rho = 1.15$ for the KABMLJ. Errors are relative to the MD simulation (whose pressure and temperature are indicated in the first row). The α that yields the lowest error for **both** pressure and temperature is chosen for the linear fit.

ρ	β	pressure	error (%)	energy	error (%)	α
1.15	1.25	5.732776	0	-5.625903	0	MD
1.15	1.25	5.934	3.51	-5.608	-0.316	4.55
1.15	1.25	5.901	2.93	-5.612	-0.235	4.70
1.15	1.25	5.880	2.57	-5.615	-0.183	4.80
1.15	1.25	5.840	1.87	-5.621	-0.085	5.0
1.15	1.25	5.830	1.71	-5.622	-0.061	5.05
1.15	1.25	5.821	1.54	-5.623	-0.038	5.10
1.15	1.25	5.812	1.38	-5.625	-0.0160	5.15
1.15	1.25	5.803	1.22	-5.626	0.0063	5.20
1.15	1.25	5.768	0.615	-5.632	0.0925	5.40
1.15	1.25	5.751	0.323	-5.6334	0.133	5.50
1.15	1.25	5.743	0.181	-5.634	0.1538	5.550
1.15	1.25	5.735	0.041	-5.635	0.173	5.60

Table 5.5: Pressure and temperature for various α for inverse temperature $\beta = 1.25$ and density $\rho = 1.15$ for the KABMLJ. Errors are relative to the MD simulation (whose pressure and temperature are indicated in the first row). The α that yields the lowest error for **both** pressure and temperature is chosen for the linear fit.

ρ	β	pressure	error (%)	energy	error (%)	α
1.15	1.65	3.789415	0	-5.914100	0	MD
1.15	1.65	3.796	0.17	-5.921	0.122	5.30
1.15	1.65	3.788	-0.034	-5.925	0.140	5.35
1.15	1.65	3.557	-0.242	-5.923	0.157	5.40
1.15	1.65	3.772	-0.44	-5.924	0.175	5.450
1.15	1.65	3.764	-0.64	-5.925	0.192	5.50
1.15	1.65	3.757	-0.8461	-5.926	0.209	5.550
1.15	1.65	3.749	-1.04	-5.9279	0.226	5.60

Table 5.6: Pressure and temperature for various α for inverse temperature $\beta = 1.65$ and density $\rho = 1.15$ for the KABMLJ. Errors are relative to the MD simulation (whose pressure and temperature are indicated in the first row). The α that yields the lowest error for **both** pressure and temperature is chosen for the linear fit.

ρ	β	pressure	error (%)	energy	error (%)	α
1.2	1.0	10.5340	0	-5.352063	0	MD
1.2	1.0	11.339	7.64	-5.257	-1.76	2.431
1.2	1.0	11.221	6.52	-5.274	-1.44	2.586
1.2	1.0	11.113	5.49	-5.290	-1.15	2.741
1.2	1.0	10.921	3.68	-5.318	-0.63	3.051
1.2	1.0	10.757	2.11	-5.3418	-0.1904	3.362
1.2	1.0	10.646	1.06	-5.357	0.109	3.600
1.2	1.0	10.561	0.25	-5.370	0.33	3.80
1.2	1.0	10.540	0.06	-5.373	0.39	3.85
1.2	1.0	10.521	-0.12	-5.376	0.44	3.9
1.2	1.0	10.482	-0.48	-5.3815	0.550	4.0

Table 5.7: Pressure and temperature for various α for inverse temperature $\beta = 1.0$ and density $\rho = 1.2$ for the KABMLJ. Errors are relative to the MD simulation (whose pressure and temperature are indicated in the first row). The α that yields the lowest error for **both** pressure and temperature is chosen for the linear fit.

ρ	β	pressure	error (%)	energy	error (%)	α
1.2	1.25	8.210453	0	-5.689269	0	MD
1.2	1.25	8.985	9.43	-5.598	-1.59	2.689
1.2	1.25	8.864	7.97	-5.615	-1.29	2.887
1.2	1.25	8.75	6.64	-5.631	-1.02	3.080
1.2	1.25	8.566	4.33	-5.657	-0.55	3.482
1.2	1.25	8.407	2.39	-5.680	-0.15	3.879
1.2	1.25	8.295	1.04	-5.696	0.120	4.20
1.2	1.25	8.23	0.274	-5.705	0.277	4.4
1.2	1.25	8.203	-0.0877	-5.709	0.351	4.5
1.2	1.25	8.1745	-0.437	-5.713	0.422	4.6

Table 5.8: Pressure and temperature for various α for inverse temperature $\beta = 1.25$ and density $\rho = 1.2$ for the KABMLJ. Errors are relative to the MD simulation (whose pressure and temperature are indicated in the first row). The α that yields the lowest error for **both** pressure and temperature is chosen for the linear fit.

ρ	β	pressure	error (%)	energy	error (%)	α
1.2	1.65	5.763603	0	-6.044759	0	MD
1.2	1.65	6.455	12.01	-5.965	-1.31	3.103
1.2	1.65	6.336	9.94	-5.981	-1.04	3.370
1.2	1.65	6.230	8.10	-5.996	-0.801	3.637
1.2	1.65	6.050	4.97	-6.021	-0.38	4.1724
1.2	1.65	5.9026	2.41	-6.041	-0.051	4.7068
1.2	1.65	5.832	1.19	-6.051	0.108	5.00
1.2	1.65	5.810	0.80	-6.0544	0.159	5.10
1.2	1.65	5.788	0.431	-6.0573	0.209	5.20
1.2	1.65	5.767	0.0658	-6.060	0.25	5.300

Table 5.9: Pressure and temperature for various α for inverse temperature $\beta = 1.65$ and density $\rho = 1.2$ for the KABMLJ. Errors are relative to the MD simulation (whose pressure and temperature are indicated in the first row). The α that yields the lowest error for **both** pressure and temperature is chosen for the linear fit.

ρ	β	pressure	error (%)	energy	error (%)	α
1.25	1.00	13.86074	0	-5.32987	0	MD
1.25	1.00	14.640	5.62	-5.244	-1.60	2.431
1.25	1.00	14.493	4.56	-5.265	-1.20	2.586
1.25	1.00	14.358	3.59	-5.285	-0.83	2.7413
1.25	1.00	14.119	1.86	-5.320	-0.18	3.0517
1.25	1.00	13.913	0.381	-5.350	0.37	3.3620
1.25	1.00	13.860	-0.0024	-5.357	0.52	3.45

Table 5.10: Pressure and temperature for various α for inverse temperature $\beta = 1.0$ and density $\rho = 1.25$ for the KABMLJ. Errors are relative to the MD simulation (whose pressure and temperature are indicated in the first row). The α that yields the lowest error for **both** pressure and temperature is chosen for the linear fit.

ρ	β	pressure	error (%)	energy	error (%)	α
1.25	1.25	11.507220	0	-5.665433	0	MD
1.25	1.25	11.988	4.18	-5.622	-0.76	2.689
1.25	1.25	11.838	2.87	-5.6437	-0.38	2.887
1.25	1.25	11.701	1.68	-5.663	-0.036	3.086
1.25	1.25	11.628	1.05	-5.6737	0.14	3.2
1.25	1.25	11.567	0.52	-5.6824	0.30	3.3
1.25	1.25	11.538	0.269	-5.6866	0.375	3.35
1.25	1.25	11.509	0.019	-5.6909	0.44	3.4
1.25	1.25	11.463	-0.38	-5.697	0.56	3.482
1.25	1.25	11.262	-2.12	-5.726	1.07	3.879
1.25	1.25	11.207	-2.607	-5.733	1.20	4.0

Table 5.11: Pressure and temperature for various α for inverse temperature $\beta = 1.25$ and density $\rho = 1.25$ for the KABMLJ. Errors are relative to the MD simulation (whose pressure and temperature are indicated in the first row). The α that yields the lowest error for **both** pressure and temperature is chosen for the linear fit.

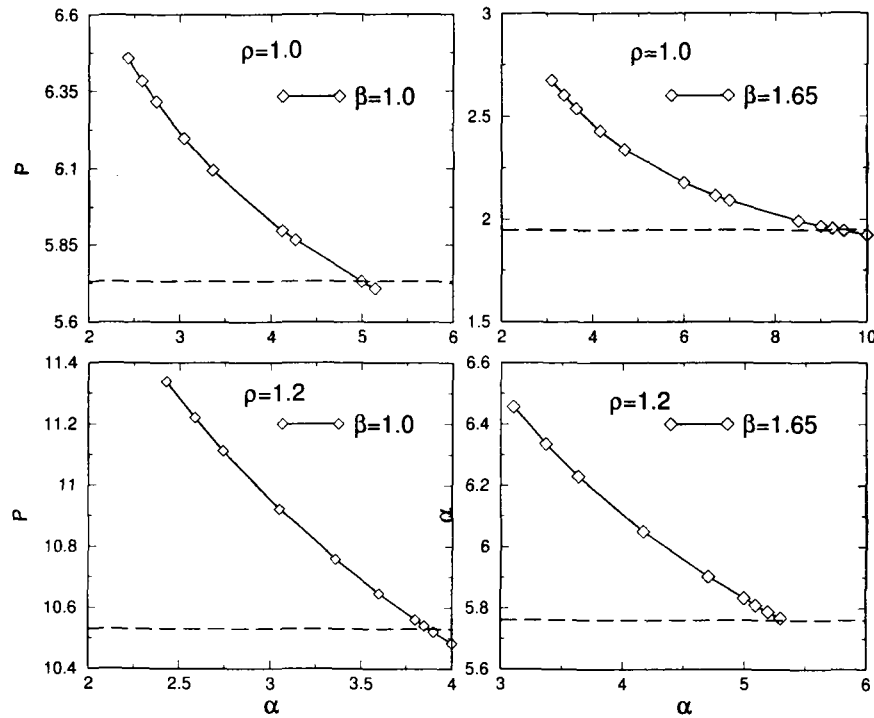


Figure 5.6: Pressure *vs* α for two representative densities and temperatures (indicated in the figure) are shown. The dashed line is the true pressure which has been obtained from molecular dynamics simulation.

5.5 Thermodynamic Approach to Glass Transition

The basic idea of the thermodynamic approach to glass transition was discussed in section 1.3 of the introduction. In this section we go into the details of evaluating the replicated free energy in order to estimate the Kauzmann temperature. Consider m replicas of a liquid. We assume an artificial attractive interaction between the particles in these different replicas. Given the

ρ	β	pressure	error (%)	energy	error (%)	α
1.25	1.65	8.539	0	-6.0906	0	MD
1.25	1.65	9.131	6.92	-6.0300	-0.99	3.103
1.25	1.65	8.980	5.16	-6.051	-0.64	3.370
1.25	1.65	8.846	3.59	-6.070	-0.33	3.637
1.25	1.65	8.617	0.91	-6.1022	0.18	4.1724
1.25	1.65	8.588	0.570	-6.106	0.258	4.25
1.25	1.65	8.569	0.353	-6.108	0.301	4.30
1.25	1.65	8.551	0.140	-6.111	0.34	4.35
1.25	1.65	8.544	0.056	-6.112	0.359	4.37
1.25	1.65	8.533	-0.068	-6.114	0.38	4.40
1.25	1.65	8.498	-0.47	-6.118	0.46	4.500
1.25	1.65	8.430	-1.27	-6.128	0.62	4.706
1.25	1.65	8.341	-2.32	-6.141	0.82	5.000

Table 5.12: Pressure and temperature for various α for inverse temperature $\beta = 1.65$ and density $\rho = 1.25$ for the KABMLJ. Errors are relative to the MD simulation (whose pressure and temperature are indicated in the first row). The α that yields the lowest error for **both** pressure and temperature is chosen for the linear fit.

interaction between different replicas the replicated Hamiltonian is

$$H_m = \sum_{i=1, N} \sum_{k=1, m} v(x_i^k - x_j^k) + \epsilon \sum_{i=1, n} \sum_{k < l = m} w(x_i^k - x_i^l) \quad (5.49)$$

Where w is the attractive term between the replicas, v is the inter atomic potential, k is the replica index and i, j are the particle indices, and ϵ is the control parameter which controls the interaction between the replicas, which is switched to zero at the end. We then write the replicated partition function as

$$Z_m = \frac{1}{(N!)^m} \int \prod_{i=1, N} \prod_{k=1, m} (d^3 x_i^k) \exp(-\beta H_m) \quad (5.50)$$

The idea of the replica formalism for the structural glasses is, that when

the configurational entropy of the system is finite (in a liquid), and ϵ is made to go to zero, the system has access to exponential number of states. But at the Kauzmann temperature where the configurational entropy of the system is not extensive any more, the system is stuck to a very small number of states. This scenario which leads to a thermodynamic transition at the Kauzmann temperature is captured using the replica formalism.

5.5.1 Replicated Free Energy for the One Component Atomic Liquid

For the sake of simplicity we will explain these ideas for a mono atomic liquid, which will be generalized later to the binary case. The partition function for such a mono atomic liquid is written using center of mass coordinates r_i and the relative coordinates u_i^k , with $x_i^k = r_i + u_i^k$ as follows,

$$Z_m = \frac{1}{N!} \int \prod_{i=1,N} (d^3 r_i) \prod_{i=1,N} \prod_{k=1,m} (d^3 u_i^k) \prod_{i=1,N} (m^3 \delta(\sum_k u_i^k)) \quad (5.51)$$

$$\times \exp \left[-\beta \sum_{i < j, k} v(r_i - r_j + u_i^k - u_j^k) - \beta \epsilon \sum_i \sum_{k,l} w(u_i^k - u_i^l) \right]$$

k, l are replica indices, i, j are particle indices. This would imply studying a system of “replica *molecules*” each of them consisting of m atoms, which forms a loop or a *cage*. If the temperatures are low, these atoms in the cage would vibrate with a small amplitude. It is reasonable to use a harmonic potential as inter replica potential, this is called the *small cage expansion*.

We make a variable change $\epsilon = \frac{1}{4\alpha}$. The partition function is now written as,

$$Z_m = \frac{1}{N!} \int \prod_{i=1,N} (d^3 r_i \prod_{i=1,N} \prod_{k=1,m} (d^3 u_i^k) \prod_{i=1,N} (m^3 \delta(\sum_k u_i^k))) \quad (5.52)$$

$$\exp \left[-\beta \sum_{i<j,k} v(r_i - r_j + u_i^k - u_j^k) - \frac{1}{4\alpha} \sum_{i,k,l} (u_i^k - u_i^l)^2 \right]$$

If we were to Taylor expand the potential and consider terms up to the quadratic order of relative coordinates, we will have the following form for the partition function,

$$Z_m = \int \prod d^3 r_i \prod d^3 u_i^k \left(m^3 \delta(\sum_k u_i^k) \right) \exp \left(-\beta m \sum_{i<j} v(r_i - r_j) \right)$$

$$\exp \left[-\frac{\beta}{2} \sum_{i<j} \sum_{k,\mu,\nu} (u_i^k - u_j^\mu)^2 \frac{\partial^2 v(r_i - r_j)}{\partial r^2} - \frac{1}{4\alpha} \sum_{a,b} (u_i^a - u_i^b)^2 \right] \quad (5.53)$$

We notice that we have a Gaussian integral for the evaluation of the partition function. If we were to work directly with $\frac{1}{\alpha} = 0$ and do the integration over the Gaussian relative variables, we would have the following form of the partition function.

$$Z_m = C \int \prod d^3 r_i \exp \left[-\beta m \sum_{i<j} v(r_i - r_j) - \frac{m-1}{2} \text{Tr} \log(\beta M) \right] \quad (5.54)$$

Here C is given by,

$$C = \frac{m^{N\frac{3}{2}} (\sqrt{\pi})^{N3(m-1)}}{N!} \quad (5.55)$$

The matrix M is $3N \times 3N$ matrix defined as follows

$$M_{(i\mu)(j\nu)} = \delta_{ij} \left(\sum_k v_{\mu\nu}(r_i - r_k) \right) - v_{\mu\nu}(r_i - r_j) \quad (5.56)$$

where $v_{\mu\nu} = \frac{\partial^2 v}{\partial r_\mu \partial r_\nu}$. On taking the logarithm; using a further approximation $\left\langle \exp \left[-\frac{(m-1)}{2} \text{Tr} \log(m\beta) \right] \right\rangle \approx \exp \left[-\frac{(m-1)}{2} \langle \text{Tr} \log(m\beta) \rangle \right]$, the replicated free energy is written as follows:

$$\beta\phi(m, T) = \frac{-3}{2m} \log(m) - \frac{3(m-1)}{2m} \log(2\pi) - \frac{1}{mN} Z(T^*) + \frac{m-1}{2m} \langle \text{Tr} \log(\beta M) \rangle^* \quad (5.57)$$

Much of the effort from this point is to calculate the Trace spectrum of instantaneous normal modes. We make the following approximation.

$$\sum_k v_{\mu\nu}(r_i - r_k) \approx \delta_{\mu\nu} \frac{1}{3} \int d^3g^*(r) \Delta v(r) = r_o \quad (5.58)$$

This approximation would mean that the diagonal terms do not fluctuate much at high densities. Therefore we could substitute for them with a constant value r_o . We can factor out the terms containing r_o and then write the trace of the logarithm for a liquid at temperature T^* , the temperature scaled by m . The “*” denotes the scaled temperature.

$$\langle \text{Tr} \log M \rangle^* = 3N \log(r_o) + \left\langle \text{Tr} \log \left[\delta_{ij} \delta_{\mu\nu} - \frac{1}{r_o} v_{\mu\nu}(r_i - r_k) \right] \right\rangle^* \quad (5.59)$$

We could now do a perturbative expansion in the powers of $\frac{1}{r_o}$. The p^{th} order term in the perturbative expansion of the trace would then be

$$T^p = \frac{(-1)^{p-1}}{p r_o^p} \left\langle \sum_{i_1 \dots i_p \dots \mu_1 \dots \mu_p} v_{\mu_1 \mu_2}(r_{i_1} - r_{i_2}) \dots v_{\mu_{p-1} \mu_p}(r_{p-1} - r_p) v_{\mu_p \mu_1}(r_p - r_1) \right\rangle \quad (5.60)$$

We then need to evaluate the p^{th} order correlation function. If we assume the chain approximation, this would be easily calculated through the pair correlation function. We can thus write the p^{th} term in the trace expansion as

$$\begin{aligned} T^p &= \sum_{\mu_1 \dots \mu_p} \int dx_1 dx_2 \dots dx_p g^*(x_1 \dots x_p) [v_{\mu_1 \mu_2}(x_1 - x_2) \\ &\quad \dots v_{\mu_{p-1} \mu_p}(x_{p-1} x_p) v_{\mu_p \mu_1}(x_p - x_1)] \\ &\approx \sum_{\mu_1 \dots \mu_p} \int dx_1 dx_2 \dots dx_p [g^*(x_1 - x_2) v_{\mu_1 \mu_2}(x_1 - x_2)] \\ &\quad \dots [g^*(x_p - x_1) v_{\mu_p \mu_1}(x_p - x_1)] \end{aligned} \quad (5.61)$$

This integral is easily done in the Fourier space. We define Fourier transformed functions $a(k)$ and $b(k)$ as follows

$$\int g^*(r) v_{\mu\nu}(r) e^{ikr} d^3r = \delta_{\mu\nu} a(k) + \left(\frac{k_\mu k_\nu}{k^2} - \frac{1}{3} \delta_{\mu\nu} \right) b(k) \quad (5.62)$$

Thus the p^{th} order term in the trace expansion would be

$$T_p = \int d^3k \left[\left(a(k) + \frac{2}{3} b(k) \right) \right]^p + 2 \int d^3k \left[\left(a(k) - \frac{1}{3} b(k) \right) \right]^p \quad (5.63)$$

$$\begin{aligned}
\langle \text{Tr} \log(\beta M) \rangle^* &= d \log(\beta r_o) + \int d^3 k L_3 \left(\frac{a(k) + \frac{2}{3}b(k)}{r_o} \right) \\
&+ \int d^3 k L_3 \left(\frac{a(k) - \frac{1}{3}b(k)}{r_o} \right) \\
&- \frac{1}{2} \int d^3 g(r) \sum_{\mu\nu} \frac{v_{\mu\nu}(r)^2}{r_o^2}
\end{aligned} \tag{5.64}$$

where the function L_3 is defined as

$$L_3(x) = \log(1-x) + x + x^2/2 \tag{5.65}$$

5.5.2 Replicated Free Energy for Binary Mixture

Let us consider the case of the KABMLJ system. The ideas are same as illustrated for the mono atomic case. The Hamiltonian is given by

$$H = \sum_{1 < i < j \leq N} V^{pq}(x_i - x_j) \tag{5.66}$$

Here V^{pq} is the inter particle potential given by,

$$V_{pq}(r) = 4\epsilon_{pq} \left[\frac{\sigma_{pq}^{12}}{r^{12}} - \frac{\sigma_{pq}^6}{r^6} \right] - V_{cut}(r) \tag{5.67}$$

Where p, q run over particle type index A and B of the KABMLJ. The cutoff V_{cut} is given by

$$\begin{aligned}
V_{cut}(r) &= [(6\sigma_{pq}^{12}/r_{cpq}^{12}) - (3\sigma_{pq}^6/r_{cpq}^6)](r/r_{cpq})^2 \\
&- 7(\sigma_{pq}^{12}/r_{cpq}^{12}) + 4(\sigma_{pq}^6/r_{cpq}^6).
\end{aligned} \tag{5.68}$$

We start from the replicated partition function

$$Z_m = \frac{m^{Nd/2} \sqrt{2\pi}^{Nd(m-1)}}{N^+! N^-!} \int \prod_{i=1, N} d^d z_i \quad (5.69)$$

$$\times \exp \left[-\beta m \sum_{i < j} V^{pq}(r_i - r_j) - \frac{m-1}{2} \text{Tr} \log(\beta M) \right]$$

Where M is a $Nd \times Nd$ matrix given by the following relation,

$$M_{(i\mu)(j\nu)}^{pq} = \delta_{ij} \left[\sum_k V^{pq}(r_i - r_k) + \frac{m}{\alpha} \right] - V_{\mu\nu}^{pq}(r_i - r_j) \quad (5.70)$$

N^+ and N^- are the number of A and B type particles.

Where $V_{\mu\nu}$ is defined as $\frac{\partial^2 V}{\partial r_\mu \partial r_\nu}$, r_i are positions of the molecules at the effective temperature $T^* = \frac{1}{\beta m}$. The so called *quenched approximation* is invoked,

$$\left\langle \exp \left[-\frac{m-1}{2} \text{Tr} \log(\beta M) \right] \right\rangle_{\beta m} \approx \exp \left[-\frac{m-1}{2} \langle \text{Tr} \log(\beta M) \rangle_{\beta m} \right] \quad (5.71)$$

We substitute for this in the partition function to get,

$$Z_m = m^{Nd/2} \sqrt{(2\pi)^{Nd(m-1)}} Z_{liq}(\beta, m) \exp \left[-\frac{m-1}{2} \langle \text{Tr} \log(\beta M) \rangle_{\beta m} \right] \quad (5.72)$$

This approximation becomes exact near the Kauzmann temperature when $m \rightarrow 1$. On normalizing the matrix elements we have.

$$C_{i\mu j\nu}^{pq} = \sqrt{\frac{C_p C_q}{r_p^2}} V_{\mu\nu}(r_{ij}) \quad (5.73)$$

where c_p and c_q are the concentrations of the p^{th} and q^{th} components of the mixture, r_p is defined as

$$r_p = \sum_{p'} c_{p'} \rho \int d^d r g_{pp'}(r) \frac{1}{d} \Delta V^{pp'}(r) + \frac{m}{\alpha} \quad (5.74)$$

The free energy now becomes

$$\begin{aligned} \beta\phi(m, \beta) &= -\frac{d}{2m} \log(m) - \frac{d(m-1)}{2m} \log(2\pi) - \frac{1}{mN} \log(Z_{liq}(\beta, m)) \\ &+ \frac{d(m-1)}{2m} (c_p \log(\beta r_p) + c_q \log(\beta r_q)) \\ &+ \frac{1}{N} \frac{(m-1)}{2m} \left\langle Tr \log \left[\delta_{ij} \sum_k C_{i\mu k\nu}^{pq} - C_{i\mu j\nu}^{pq} \right] \right\rangle \end{aligned} \quad (5.75)$$

We then write the free energy up to second order in $\sum_k C_{i\mu k\nu}^{pq}$. All of C_{ij} is resummed within the chain approximation. The free energy is then given by

$$\begin{aligned} \beta\phi(m, \beta) &= -\frac{d}{2m} \log(m) - \frac{d(m-1)}{2m} \log(2\pi) \\ &- \frac{1}{mN} \log [Z_{liq}(\beta, m)] \\ &+ \frac{d(m-1)}{2m} [c_p \log(\beta r_p) + c_q \log(\beta r_q)] \\ &- \frac{1}{2N} \frac{m-1}{2m} (\langle Tr C_{i\mu k\nu}^{pq} C_{i\mu k'\nu}^{pq} \rangle - dN) \\ &+ \frac{1}{N} \frac{(m-1)}{2m} \sum_{p=2}^{\infty} \left\langle Tr \frac{C^p}{p} \right\rangle \end{aligned} \quad (5.76)$$

We once again encounter a p point correlation function

$$\langle Tr C^p \rangle = \sum_{q_1 \dots q_p \{A,B\}} \sum_{\mu_1 \dots \mu_p} \int d^d z_1 \dots d^d z_p \rho^p g^{q_1 \dots q_p}(z_1 \dots z_p) C_{\mu_1 \mu_2}^{q_1 q_2}(z_2 - z_1) \dots C_{\mu_p \mu_1}^{q_p q_1}(z_p - z_1) \quad (5.77)$$

Using the chain approximation, we write the correlation as follows

$$\langle Tr C^p \rangle = \int d^d z_1 \dots d^d z_p \sum_{\mu_1 \dots \mu_p} \sum_{q_1 \dots q_p} \rho^p C_{\mu_1 \mu_2}^{q_1 q_2} g(z_1 - z_2) \dots C_{\mu_p \mu_1}^{q_p q_1}(z_p - z_1) g(z_p - z_1) \quad (5.78)$$

We then compute the traces in the Fourier space, for that we define a matrix D whose elements are given by

$$D_{\mu\nu}^{pq} = \int d^d r g^{pq}(r) C_{\mu\nu}^{pq}(r) e^{ikr} \quad (5.79)$$

If we were to decompose this matrix into a diagonal (longitudinal) and a traceless (transversal) part,

$$D_{\mu\nu}^{pq}(k) = \delta_{\mu\nu} a^{pq}(k) + \left(\frac{k_\mu k_\nu}{k^2} - \frac{\delta_{\mu\nu}}{d} \right) b^{pq}(k) \quad (5.80)$$

We then can diagonalize in the space of its components, corresponding to the longitudinal

$$D_{\parallel}^{pq} = a^{pq}(k) + \frac{d-1}{d} b^{pq}(k) \quad (5.81)$$

and the transverse part

$$D_{\perp}^{pq} = a^{pq}(k) - \frac{1}{d} b^{pq}(k) \quad (5.82)$$

The eigen values then are

$$\begin{aligned}
\lambda_{\parallel} &= \frac{1}{2}[D_{\parallel}^{pp} + D_{\parallel}^{qq} + \sqrt{((D_{\parallel}^{pp} - D_{\parallel}^{qq})^2 + 4D_{\parallel}^{pq})}] & (5.83) \\
\mu_{\parallel} &= \frac{1}{2}[D_{\parallel}^{pp} + D_{\parallel}^{qq} - \sqrt{((D_{\parallel}^{pp} - D_{\parallel}^{qq})^2 + 4D_{\parallel}^{pq})}] \\
\lambda_{\perp} &= \frac{1}{2}[D_{\perp}^{pp} + D_{\perp}^{qq} + \sqrt{((D_{\perp}^{pp} - D_{\perp}^{qq})^2 + 4D_{\perp}^{pq})}] \\
\mu_{\perp} &= \frac{1}{2}[D_{\perp}^{pp} + D_{\perp}^{qq} - \sqrt{((D_{\perp}^{pp} - D_{\perp}^{qq})^2 + 4D_{\perp}^{pq})}]
\end{aligned}$$

The total replicated free energy is now given by,

$$\begin{aligned}
\phi(m, \beta) &= \frac{d}{2m} \log(m) - \frac{d(m-1)}{2m} \log(2\pi) - \frac{1}{mN} \log[Z_{liq}(\beta, m)] & (5.84) \\
&+ \frac{d(m-1)}{2m} [c_p \log(\beta r_p) + c_q \log(\beta r_q)] \\
&- \frac{(m-1)}{2m} \frac{1}{\rho} \int \frac{d^d k}{2\pi^3} \sum_{ijk} a^{ij}(k) a^{jk}(k) h^{ki}(k) + \left(1 - \frac{1}{d}\right) b^{ij}(k) b^{jk}(k) h^{ki}(k) \\
&\times \int \frac{d^d k}{2\pi^3} [L_3(\lambda_{\parallel}(k) + \mu_{\parallel}(k) + (d-1)(\lambda_{\perp}(k) + \mu_{\perp}(k))] \\
&- \frac{(m-1)}{2m} \int d^d r \rho \sum_{\alpha\gamma} g^{\alpha\gamma}(r) \sum_{\mu\nu} (C_{\mu\nu}^{\alpha\gamma}(r))^2
\end{aligned}$$

We then compute the complexity from

$$\Sigma_{eq} = m^2 \frac{\partial \beta \phi}{\partial m} = S_{liq} - S_{sol} \quad (5.85)$$

S_{liq} is the entropy of the liquid at effective temperature T , which would

equal the actual temperature at $m = 1$. The solid entropy to be given by

$$S_{sol} = \frac{d}{2} \log(2\pi e) - \frac{1}{2N} \langle Tr \log(\beta m) \rangle \quad (5.86)$$

The condition of the Kauzmann temperature is

$$S_{sol} = S_{liq} \quad (5.87)$$

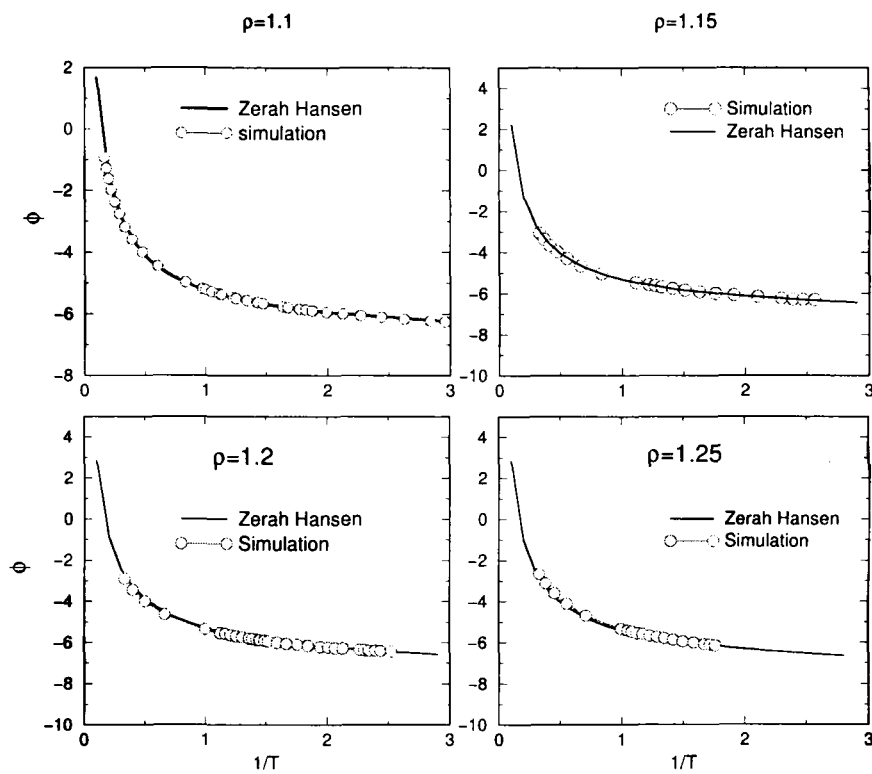


Figure 5.7: Energy the Liquid for densities $\rho = 1.1, 1.15, 1.20, 1.25$ got from simulation and ZH scheme.

5.5.3 Calculation of the Kauzmann Temperature

In order to evaluate the Kauzmann temperature, we need to calculate the entropy of the liquid and the solid phase. The entropy of the liquid is obtained via the following thermodynamic equation,

$$S_{liq}(\rho, T) = S_{liq}^0 + \beta e_{liq}(\beta) - \int_0^\beta d\beta' e_{liq}(\beta') \quad (5.88)$$

Here, S_{liq}^0 is the entropy of a perfect gas with density ρ , in the binary mixture case it is given by,

$$S_{liq}^0 = 1 - \log(\rho) - c \log(c) - (1 - c) \log(1 - c) \quad (5.89)$$

c here is the concentration of one of the components. The internal energy e_{liq} is obtained from the ZH scheme. We show in Fig 5.6 the potential energy match from ZH and simulation for $\rho = 1.0, 1.05, 1.10, 1.15, 1.20$ as a function of temperature. This is further proof that the fits for the interpolation function is a good one. The entropies of the liquid phase for these densities are shown in Fig 5.7. The entropy of the solid phase is given by

$$S_{sol}(\rho, T) = 3/2 (1 + \log(2\pi)) - \frac{1}{2N} \langle Tr \log(\beta M) \rangle \quad (5.90)$$

where $\langle Tr \log(\beta M) \rangle$, can be obtained using Eq. 5.84-5.85; at $m=1$ and comparing with Eq. 5.86

$$\begin{aligned}
\langle Tr \log(\beta M) \rangle &= \frac{d}{2} [c_p \log(\beta r_p) + c_q \log(\beta r_q)] & (5.91) \\
&- \frac{1}{2} \frac{1}{\rho} \int \frac{d^d k}{2\pi^3} \sum_{ijk} a^{ij}(k) a^{jk}(k) h^{ki}(k) + \left(1 - \frac{1}{d}\right) b^{ij}(k) b^{jk}(k) h^{ki}(k) \\
&\times \int \frac{d^d k}{2\pi^3} [L_3(\lambda_{\parallel}(k) + \mu_{\parallel}(k) + (d-1)(\lambda_{\perp}(k) + \mu_{\perp}(k))] \\
&- \frac{1}{2} \int d^d r \rho \sum_{\alpha\gamma} g^{\alpha\gamma}(r) \sum_{\mu\nu} (C_{\mu\nu}^{\alpha\gamma}(r))^2
\end{aligned}$$

The ZH equations become unstable at low temperatures. We need to extrapolate the liquid and the solid entropies. The liquid entropies are extrapolated using the power law [96] [30], $S_{liq}(T) = aT^{-2/5} + b$. Solid phase entropy is extrapolated as $S_{sol} = a + b \log(T)$ [31]. The configurational entropy $S_{sol} - S_{liq}$ is illustrated in Fig 5.8. The Kauzmann temperature is found as the temperature when $S_{sol} - S_{liq} = 0$.

5.6 Phase Diagram

We now have the complete phase diagram which bounds the limit of stability of a liquid. We compare our results with earlier computer simulations (illustrated in Fig 5.9). The spinodals points deviate from those of the simulations at low temperatures, this we attribute to the extrapolated equation of state in the case of computer simulation. Also the Kauzmann temperature happens to be slightly higher with the Mezard-Parisi scheme as compared to

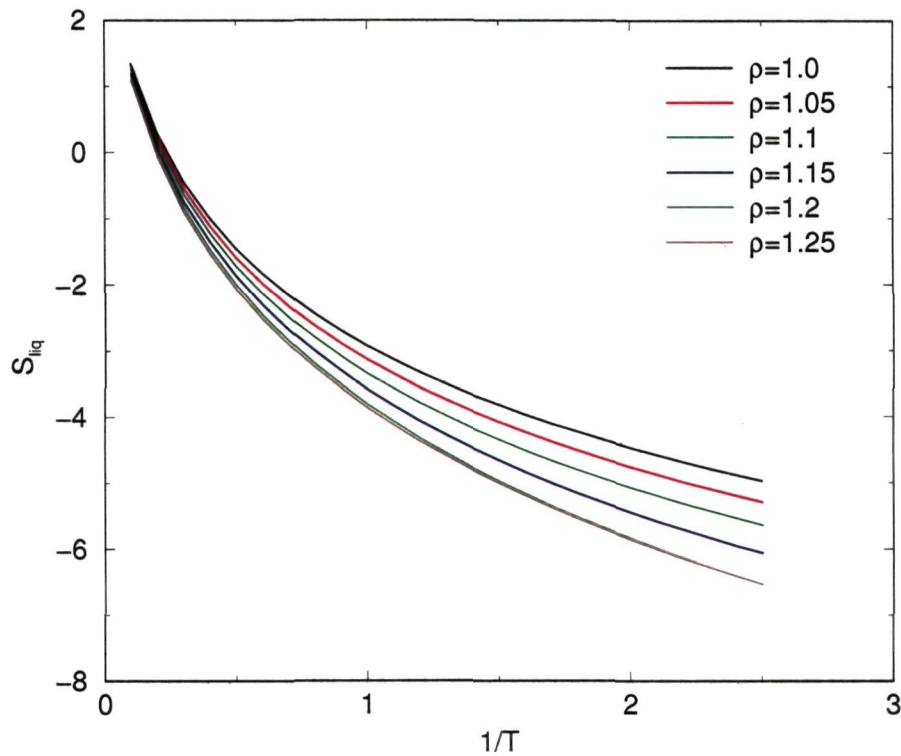


Figure 5.8: Excess entropy of the liquid relative to the ideal gas for densities $\rho = 1.0, 1.05, 1.10, 1.15, 1.20, 1.25$ calculated through thermodynamic integration.

those calculated from simulation. This we attribute to the harmonic resummation scheme which becomes less accurate as the density is lowered. We have qualitative consistency with computer simulations, and we show that indeed the two limits of stability meet at a finite temperature. The Sastry density in our case is slightly under estimated at $\rho \approx 0.95$ as compared to $\rho \approx 1.08$ in simulations.

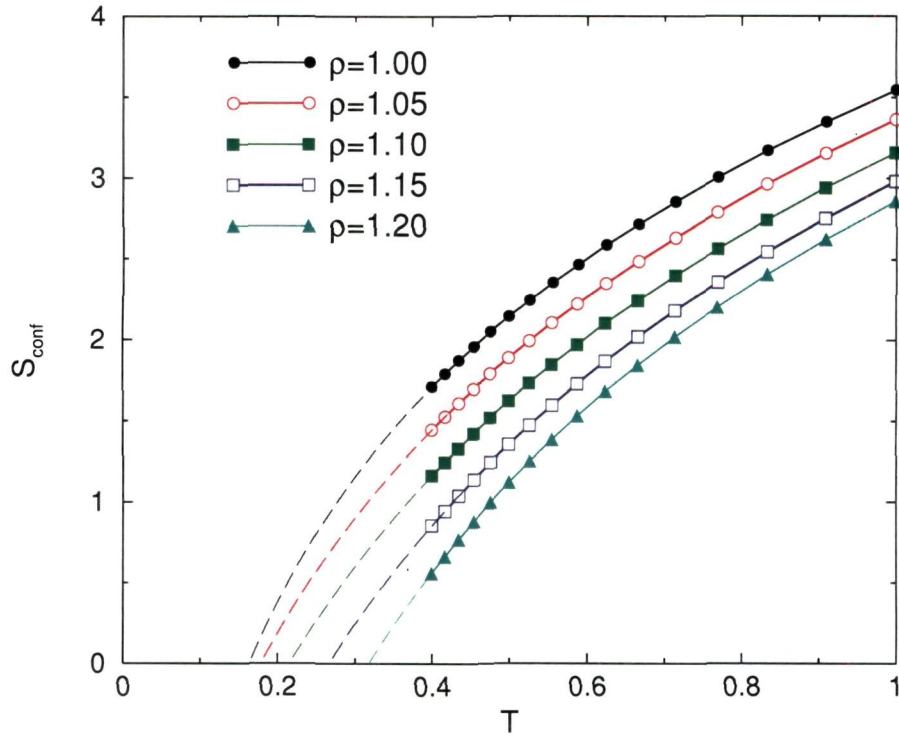


Figure 5.9: The configurational entropy of the the liquid has been calculated for $\rho = 1.0, 1.05, 1.10, 1.15, 1.20$. The temperatures at which the configurational entropy is zero is identified as the Kauzmann temperature for that particular density.

5.7 Conclusions

In conclusion we have demonstrated theoretically that the loci of the extreme limits of stability namely the ideal glass transition line and the liquid-gas spinodal curve intersect at a finite temperature. We find that our results [11] match qualitatively well with the earlier computer simulations.

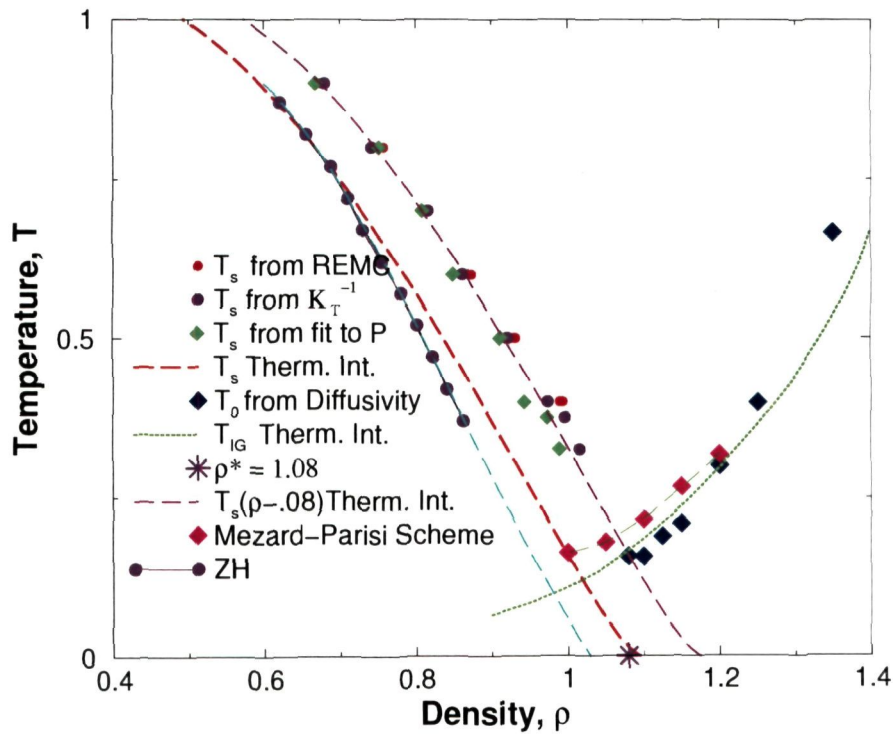


Figure 5.10: Depicted in the phase diagram s the spinodal lines and the ideal glass transition line. The spinodals are calculated from REMC (red circles), inverse compressibility (violet star), fit from the equation of state (green diamond), thermodynamic integration (red dashed line) and analytic spinodal through the ZH scheme (violet circles). Glass transition line is calculated from VFT (blue diamonds), thermodynamic integration (green dotted line) and Mezard-Parisi scheme (magenta diamonds). The big violet star in the $T = 0$ indicates the Sastry density through simulation.

Chapter 6

Onset of Breakdown of the Stokes-Einstein Relation

In the introduction we mentioned that the dynamics changes at the onset of slow dynamics temperature [104]. Above this temperature the liquid displays Arrhenius temperature dependence of diffusivity and super-Arrhenius dependence below. The situation below the onset temperature has been described as *energy landscape influenced* [104]. In order to characterize this cross over one could examine various physical characteristic such as inherent structure energies, extent of heterogeneity etc. In this chapter we examine the Stokes-Einstein relation (S-E) and show that it breaks down at the onset temperature.

For simple liquids at high temperatures the viscosity η and the diffusivity D are related by the well known Stokes-Einstein relation.

$$D = \frac{k_B T}{6\pi\eta d} \quad (6.1)$$

T is the temperature and d is called the hydrodynamic diameter, it characterizes the size of the particle. This relation yields d to be

$$d = \frac{k_B T}{6\pi\eta D} \quad (6.2)$$

As one lowers the temperature below the onset temperature, this relation starts to break down yielding a varying d [21]. We wish to establish in this chapter that the Stokes-Einstein relationship indeed breaks down at the onset temperature of slow dynamics. We do these calculations for two densities $\rho = 1.1$ and 1.2 for the KABMLJ liquid whose onset temperature is known [101]. The onset temperature for density 1.1 is around 0.7 and that of density 1.2 is around 1.0 in KABMLJ reduced units [67]. In order to calculate the viscosity we use Müller-Plathe's algorithm [84]. The diffusivity is also calculated simultaneously from the mean squared displacement (MSD). We will first describe Müller-Plathe's method and then we discuss our results.

6.1 Müller-Plathe's Algorithm

Consider a fluid subjected to shear. See Fig. 6.1. One could consider the flow to be in a series of layers as indicated in Fig 6.1. The velocity in each of the layer would be different depending on the boundary conditions. The momentum flux along z corresponding to the velocity gradient is given by

$$j_z(p_x) = -\eta \frac{\partial v_x}{\partial z} \quad (6.3)$$

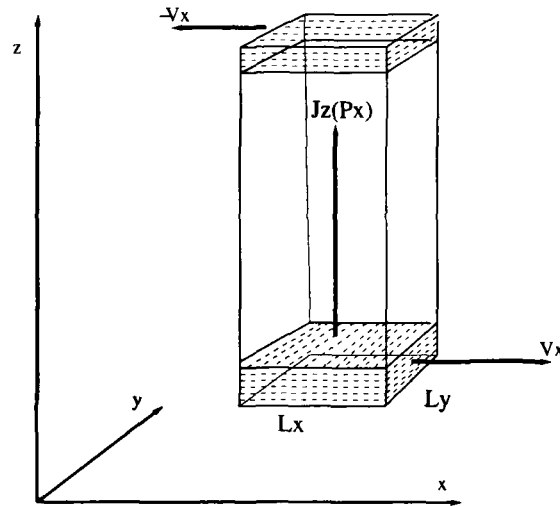


Figure 6.1: Simulation box showing the direction of atom velocities and momentum transfer along z -directions.

The proportionality constant is defined as the viscosity. The simulation box is of size L_z along the z -direction and one divides the simulation box along the z -direction into N equal slabs as shown in Fig. 6.2. Müller-Plathe's method for calculating the shear viscosity involves the imposition of a momentum flux and measuring the velocity gradient in the steady state. It is done in the following manner. Consider the slab with $z=0$. One chooses the particle with the largest momentum p_x along the $-x$ direction. One also chooses the atom with the largest momentum along the $+x$ direction from the slab corresponding $z = L_z/2$ and then one exchanges the x component of the velocity of these two atoms. This operation conserves the linear momentum, kinetic energy and the potential energy (relative positions remain unchanged) of the system. When many such operations are performed one has a velocity profile as illustrated in Fig. 6.2. After many such operations

the amount of momentum Δp_x transferred from the $z = L_z/2$ to $z = 0$ is P_x .

The momentum flux is then given by

$$j(p_x) = \frac{P_x}{2tL_xL_y} \quad (6.4)$$

Here L_x, L_y are the lengths of the simulation box along the x and the y direction, t is the time interval over which the exchanges are made and the factor of 2 arises due to the periodicity in the system. The flow velocity v_x is calculated as an average over all the atoms. Under the condition that the momentum flux is small the velocity profile $\langle \frac{\partial v_x}{\partial z} \rangle$ would be linear. One can then calculate the viscosity from equation (6.3).

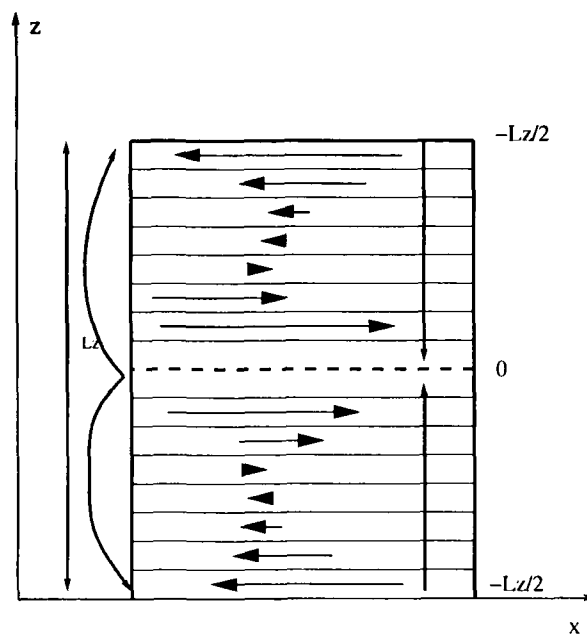


Figure 6.2: Simulation box with velocity profiles shown as arrows. The different slabs have different velocities.

6.2 Results and Discussions

We have used Müller-Plathe's algorithm to calculate viscosity for the densities $\rho = 1.1$ and $\rho = 1.2$. We use a 750 atom Kob Andersen binary Lennard Jones system [67] (see chapter 1). The simulation box is divided into 16 slabs as discussed in the previous section. We use a time step of 0.003 in KABMLJ units. We do the calculations for twelve temperatures varying between $T = 0.35 - 1.60$ for density 1.1. We have done simulations for 20-40 million time steps. For density 1.2 we do simulations for 11 temperature between $T = 0.59 - 1.99$. We have done simulations for 20-65 million time steps. We calculate the velocity profiles as shown in Fig 6.3-6.4. We get the expected velocity profile. One notices that there is a slight hump in the middle, this is caused because the small [20] exchange period used. If one were to increase the exchange period one may have to do longer runs. So we let this be, since this does not effect the velocity gradient.

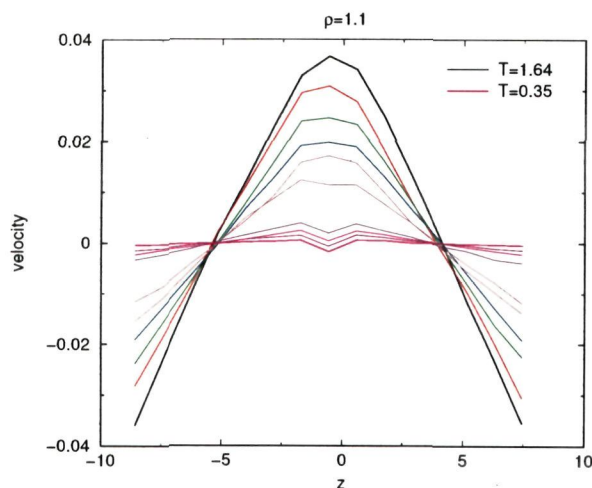


Figure 6.3: velocity profile v as a function of the slab height z for density 1.1. These profiles have been calculated for temperatures between $T=0.35-1.64$.

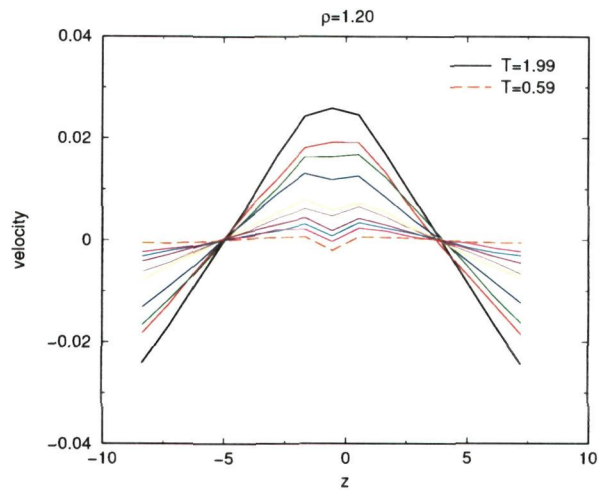


Figure 6.4: velocity profile v as a function of the slab height z for density 1.2. These profiles have been calculated for temperatures between $T=0.59-1.99$.

We calculate the the viscosity and fit it to the VFT equation

$$\eta(T) = \eta_{\infty} \exp \left[\frac{AT_o}{T - T_o} \right] \quad (6.5)$$

Fig. 6.8 and Fig. 6.10 show very good fit of the viscosity to the VFT equation. We tabulate the fit parameter η_{∞} , A and T_o for densities 1.1 and 1.2 in Table 6.1.

ρ	η_{∞}	A	T_o
1.1	2.785	2.848	0.20486
1.2	3.00866	3.65319	0.2976

Table 6.1: The fit parameters of viscosity vs temperature using the VFT (Eq 1.1).

The diffusivity was calculated from the mean squared displacement (MSD)

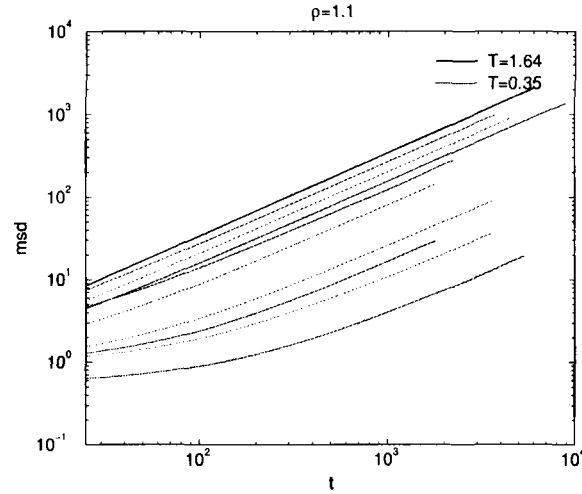


Figure 6.5: Mean squared displacement as a function of time for density 1.1. These calculation are done for temperatures between $T=0.35-1.64$.

$\langle r^2 \rangle$. The diffusivity and the MSD are related via $D = \langle r^2 \rangle / 6t$. Simulations were done till the MSD showed linear behavior with time (Fig 6.5-6.6). This MSD was fit to a linear equation from which the slope is calculated to determine the diffusivity. This diffusivity was calculated for several temperatures shown in Fig 6.7. and Fig 6.9. The estimate of the particle size is sensitive to the errors in the diffusivity and viscosity from the simulations. In order to get a smooth curve of d vs T , to determine the onset temperature, the fits becomes necessary. At low temperatures the evolution of shear viscosity differs from the Arrhenius behaviour and is captured well by the VFT equation (Eq 6.5). For the diffusivity we use here a modified form of the VFT equation [21].

$$D(T) = \frac{T}{\xi} \exp \left[-\frac{AT_o}{T - T_o} \right] \quad (6.6)$$

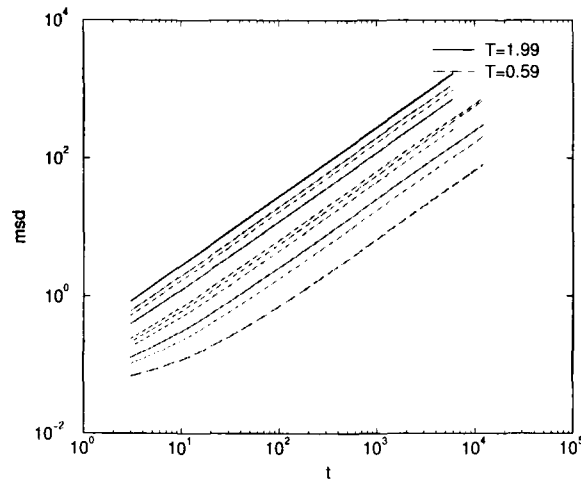


Figure 6.6: Mean squared displacement as a function of time for density 1.2. These calculation are done for temperatures between $T=0.59-1.99$.

ρ	ξ	A	T_o
1.1	18.2344	5.0873	0.136002
1.2	24.2196	3.65319	0.2767

Table 6.2: The fit parameters of diffusivity *vs* temperature using the modified VFT.

The fits parameters are tabulated in Table 6.2.

We then calculate the hydrodynamic diameter as a function of temperature. We note that for density 1.1 (Fig. 6.11) the hydrodynamic diameter is no more a constant below $T \sim 0.7$ and for density 1.2 (Fig. 6.12) this happens around $T \sim 1.0$. This is precisely around the temperature predicted for the onset temperature for slow dynamics [101].

6.3 Fractional Stokes-Einstein

A common explanation for the break down of S-E equation in supercooled liquids is the presence of the so called *dynamical heterogeneity* (DH) [116,

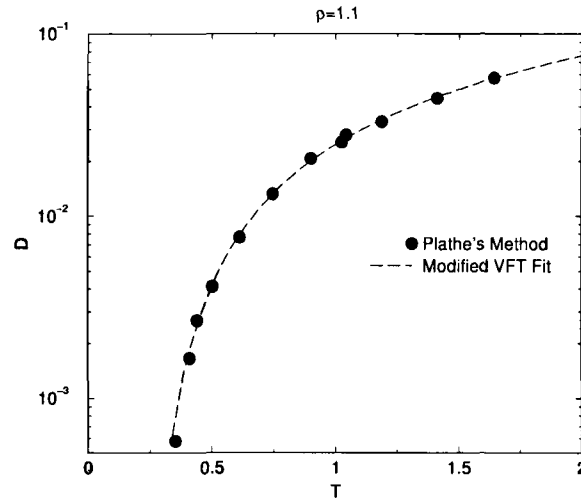


Figure 6.7: Diffusivity *vs* Temperature calculated from the MSD for density 1.1, the fit modified VFT given in the text.

123]. In a supercooled liquid one finds spatially correlated regions of varying mobility that persist for finite life times. These regions grow in size as one decreases the temperature. These regions with varying mobility has been thought of to cause a break down in S-E. Though the S-E relation fails, another empirical relation, the so called fractional Stokes-Einstein (FSE)

$$D \sim (T/\eta)^\kappa \quad (6.7)$$

is seen to hold for many liquids, This empirical law seems to be consistent for KABMLJ below the onset temperature (Fig 6.13,6.14). We estimate κ for two densities $\rho = 1.1$ and 1.2 to be 0.83 and 0.82 respectively. It must be pointed out that DH explanation is still under active investigation and not yet a completely accepted theory. Recent MD simulations [16] using ST2 model for water show that the same FSE relation holds both for mobile as well

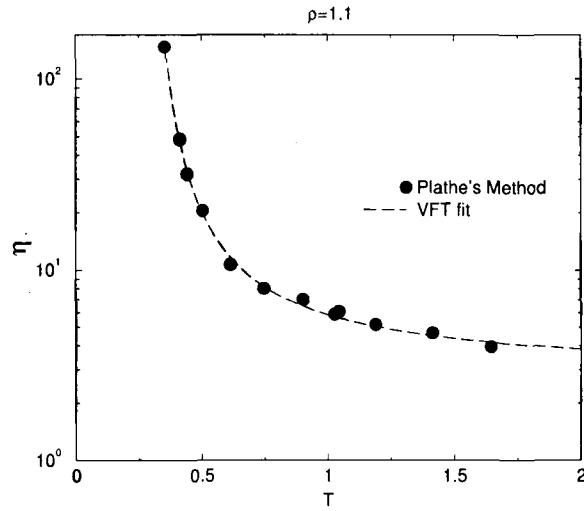


Figure 6.8: Viscosity *vs* Temperature calculated from the MSD for density 1.1, the fit VFT given in the text.

as immobile regions. Further recent simulations [68] on polydispersed hard spheres show the break down of S-E was primarily due to particles involved in hopping dynamics, which do not obey the S-E relation. This could also be a possible scenario for the case of KABMLJ at the onset temperature.

6.4 Conclusions

We have calculated here the viscosity and diffusivity through an algorithm given by Müller-Plathe for the KABMLJ liquid. We investigated the temperatures where the well known Stokes-Einstein relation starts to fail at the onset of slow dynamics temperature. We do these calculations for densities 1.1 and 1.2. It is known that the KABMLJ liquid has an onset temperature of around 0.7 and 1.0 for densities 1.1 and 1.2 respectively. We conclude that indeed the Stokes-Einstein relation breaks around these temperatures and

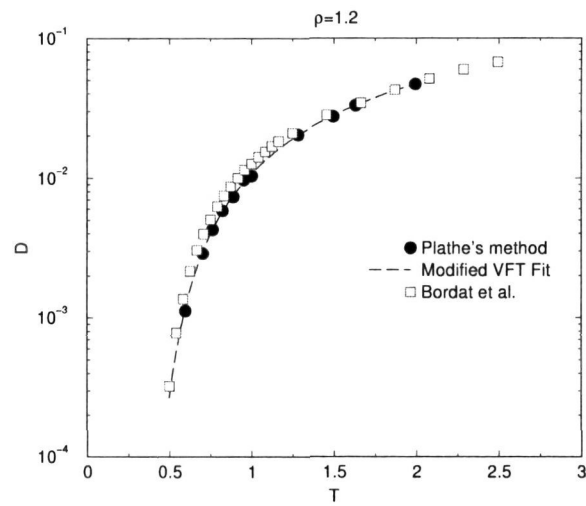


Figure 6.9: Diffusivity *vs* Temperature calculated from the MSD for density 1.2, the fit modified VFT given in the text. Data of Bordat, *et al.*, [21] is compared.

fractional S-E consistent with data below the onset temperature.

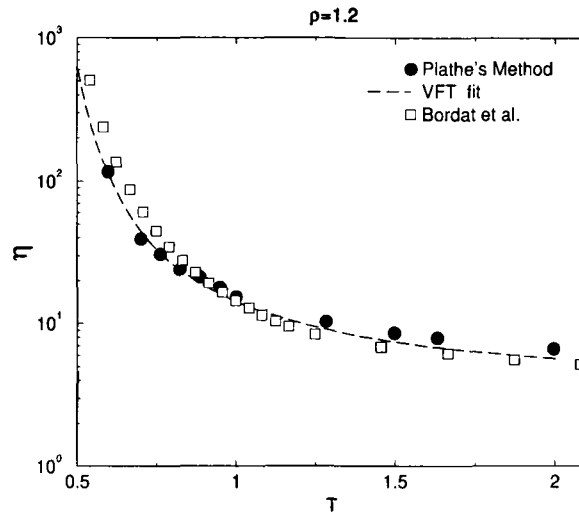


Figure 6.10: Viscosity *vs* Temperature calculated from the MSD for density 1.2, the fit VFT given in the text. Data of Bordat, *et al.*, [21] is compared.

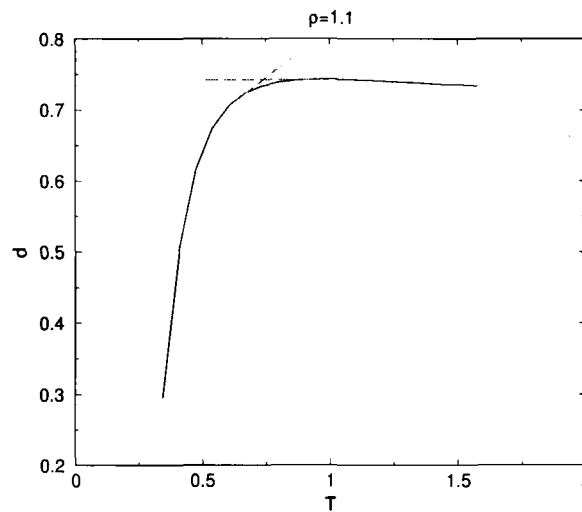


Figure 6.11: Hydrodynamic diameter calculated as function of non equilibrium temperature for density $\rho = 1.1$. The onset of break down of the Einstein stokes relation at around $T=0.7$.

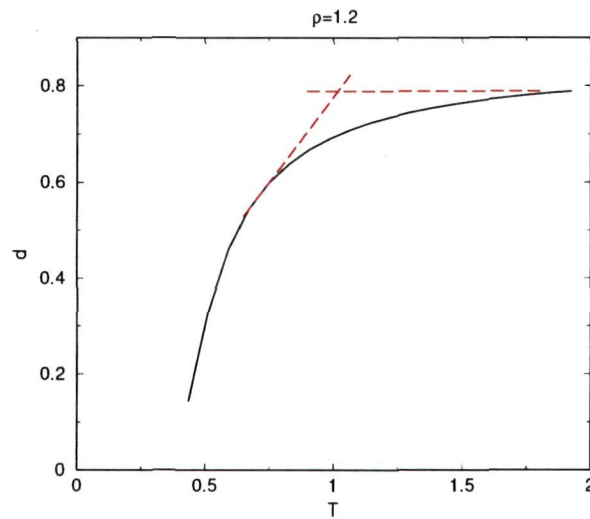


Figure 6.12: Hydrodynamic diameter calculated as function of non equilibrium temperature for density $\rho = 1.2$. The onset of break down of the Einstein stokes relation at around $T=1.0$.

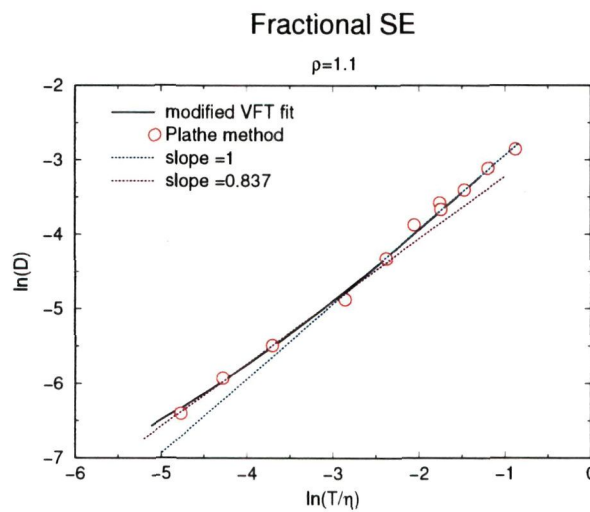


Figure 6.13: Fractional S-E is consistent for the KABMLJ liquid with $\rho = 1.1$ below the onset temperature with $\kappa = 0.837$. The onset of break down of the Einstein stokes relation at around $T=0.7$.

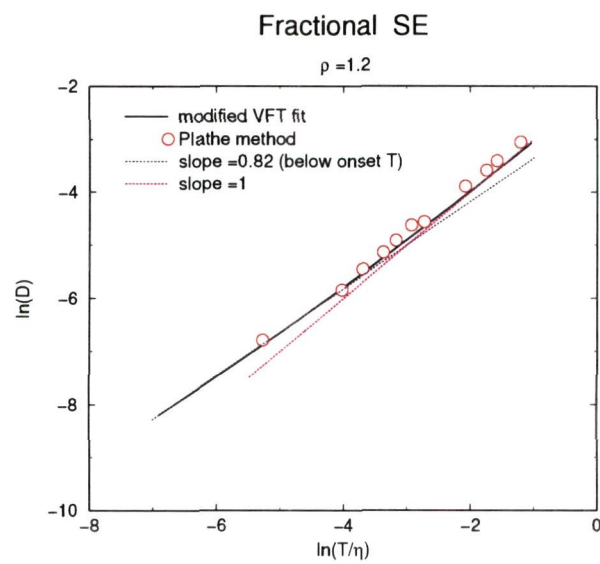


Figure 6.14: Fraction S-E is consistent for the KABMLJ liquid with $\rho = 1.2$ below the onset temperature with $\kappa = 0.82$. The onset of break down of the Einstein stokes relation at around $T=1.0$.

Bibliography

- [1] ALLEN, P. B. & BROUGHTON, J. Q. 1987 *J. Phys. Chem.* **91**, 4964.
- [2] ANGELANI, L., LEONARDO, R. D., RUOCCO, G., SCALA, A. & SCIORTINO, F. 2000 *Phys. Rev. Lett.* **85**, 5356.
- [3] ANGELL, C. A. 1988 *J. Non-Cryst. Sol.* **102**, 205.
- [4] ANGELL, C. A. 2000 *Phys. Chem. Chem. Phys.* **2**, 1599.
- [5] ANGELL, C. A., BORICK, S. S. & GRABOW, M. 1996 *J. Non-Cryst. Solids.* **463**, 205.
- [6] ANGELL, C. A., NGAI, K. L., MCKENNA, G. B., McMILLAN, P. F. & MARTIN, S. W. 2000 *J. Appl. Phys.* **88**, 3113.
- [7] APTEKAR, L. I. 1979 *Sov. Phys. Dokl.* **24**, 993.
- [8] ASHCROFT, N. W. & LEKNER, J. 1966 *Phys. Rev.* **145**, 83.
- [9] ASHCROFT, N. W. & MERMIN, N. D. *Introduction to Solid State Physics* 5th edn. Wiley & Sons, Texas, 1976.
- [10] ASHWIN, S. S., BRUMER, Y., REICHMAN, D. R. & SASTRY, S. 2004 *J. Phys. Chem. B.* **108**(51), 19703.

-
- [11] ASHWIN, S. S., MENON, G. I. & SASTRY, S. (*accepted for publication Europhys. Lett.*), <http://xxx.lanl.gov/abs/cond-mat/0512728> .
- [12] ASHWIN, S. S. & SASTRY, S. 2003 *J. Phys. Cond. Mat* **15**, S1253.
- [13] ASHWIN, S. S., WAGHMARE, U. V. & SASTRY, S. (*Manuscript in Preparation to be submitted to PRB*) .
- [14] ASHWIN, S. S., WAGHMARE, U. V. & SASTRY, S. 2004 *Phys. Rev. Lett.* **92**, 175701.
- [15] BAGLEY, B. G. & CHEN, H. S. *Laser-Solid Interactions and Laser Processing - 1978* 50th edn. AIP Conf. Proc., 1990.
- [16] BECKER, S. R., POOLE, P. H. & STARR, F. W. <http://xxx.lanl.gov/abs/cond-mat/0605170> .
- [17] BERTHIER, L. & BARRAT, J. 2002 *J. Chem. Phys.* **116**, 6228.
- [18] BLOCH, F. 1928 *Z. Phys.* **52**, 555.
- [19] BOON, J. & YIP, S. *Molecular Hydrodynamics* Dover, 1980.
- [20] BORDAT, P. *Private Communication*, .
- [21] BORDAT, P., AFFOUARD, F., DESCAMPS & MÜLLER-PLATHE 2003 *J. Phys.: Condens. Matter* **15**, 5397.
- [22] BRAZHKIN, V. *et al.* 1997 *High Pres. Res.* **15**, 267.
- [23] BRAZHKIN, V. V., BULDYREV, S. V., RYZHOV, V. N. & [EDS], H. E. S. *New Kinds of Phase Transitions: Transformations in Disordered*

- Substances* Proc. NATO Advanced Research Workshop, Volga River
Kluwer, Dordrecht, 2002.
- [24] BRODERIX, K., BHATTACHARYA, K. K., CAVAGNA, A., ZIPPELIUS,
A. & GIARDINA, I. 2000 *Phys. Rev. Lett.* **85**, 5360.
- [25] BRUMER, Y. 2003 *Ph. D. thesis, Harvard University (unpublished)* .
- [26] C.-H. LIU, *et al.* 1995 *Science* **269**, 513.
- [27] CAVAGNA, A. 2001 *Europhys. Lett.* **53**, 490.
- [28] COHEN, M. L. & HEINE, V. 1970 *Solid State Physics* **24**, 37.
- [29] COLUZZI, B., MEZARD, M., PARISI, G. & VERROCCHIO, P. 1999 *J. Chem. Phys.* **111**, 9039.
- [30] COLUZZI, B., MEZARD, M., PARISI, G. & VERROCCHIO, P. 2000 *J. Chem. Phys.* **112**, 2933.
- [31] COLUZZI, B. & VERROCCHIO, P. 2002 *J. Chem. Phys.* **116**, 3789.
- [32] COPPERSMITH, S. N., H. LIU, C., MAJUMDAR, S., NARAYAN, O. &
WITTEN, T. A. 1996 *Phys. Rev. E.* **53**, 4673.
- [33] DEB, S.K., *et al.* 2001 *Nature* **414**, 528.
- [34] DEBENEDETTI, P. G. *Metastable Liquids: Concepts and Principles.*
1st edn. Princeton University Press, 1996.
- [35] DENNY, R. A., REICHMAN, D. R. & BOUCHAUD, J.-P. *Phys. Rev. Lett.* **90**.

-
- [36] DOLIWA, B. & HEUER, A. 2003 *Phys. Rev. E* **67**, 031506.
- [37] DONG, J. & DRABOLD, D. A. 1998 *Phys. Rev. Lett.* **80**, 1928.
- [38] DONOVAN, E.P., *et al.* 1985 *J. Appl. Phys.* **57**, 1795.
- [39] DONTH, E. *The Glass Transition: Relaxation Dynamics in Liquid and Disordered Materials* Springer Verlag, 2002.
- [40] EASTWOOD, J. W. & HOCKNEY, R. W. *J. Comp. Phys.*, .
- [41] FABER, T. E. & ZIMAN, J. M. 1965 *Phil. Mag.* **11**, 153.
- [42] FRANZ, S. & PARISI, G. 1997 *Phys. Rev. Lett.* **79**, 2486.
- [43] FRENKEL, D. & SMIT, B. *Understanding Molecular Simulation* Academic Press, 1996.
- [44] FULCHER, G. S. 1925 *J. Am. Ceram. Soc.* **8**, 339.
- [45] GIBBS, J. H. & DIMARZIO, E. A. 1958 *J. Chem. Phys.* **28**, 373.
- [46] GLAZOV, V. M., CHIZHEVSKAYA, S. N. & GLAGOLEVA, N. N. *Liquid Semiconductors* Plenum, New York, 1969.
- [47] GLOSLI, J. N. & REE, F. H. 2000 *Nature*. **403**, 170.
- [48] GOLDSTEIN, M. 1969 *J. Chem. Phys.* **51**, 3728.
- [49] GÖTZE, W. & SJÖGREN, L. 1992 *Rep. Prog. Phys.* **55**, 241.
- [50] GREENHARD, L. & V.ROCKHLIN *J. Comp. Phys.*, .

-
- [51] GRIGERA, T. S., CAVAGNA, A. & I. GIARDINA, G. P. 2002 *Phys. Rev. Lett.* **88**, 055502.
- [52] HAMANN, D. R., SCHLUTER, M. & CHIANG, C. 1979 *Phys. Rev. Lett.* **43**, 1979.
- [53] HARRISON, W. A. *Pseudopotentials in the Theory of Metals* 1966.
- [54] HEINE, V. & ABARENKOV, I. 1964 *Phil. Mag.* **9**, 451.
- [55] HEREMANS, J., OLK, C. H., EESLEY, G. L., STEINBECK, J. & DRESSELHAUS, G. 1988 *Phys. Rev. Lett.* **60**, 452.
- [56] HORBACH, J. & KOB, W. 1999 *Phys. Rev. B.* **60**, 3169.
- [57] HORBACH, J. & KOB, W. 1999 *J. Phys. Cond. Mat* **60**, 3169.
- [58] HORBACH, J., KOB, W. & BINDER, K. 2001 *Eur. Phys. J. B* **19**, 531.
- [59] HORBACH, J., KOB, W., BINDER, K. & ANGELL, C. A. 1996 *Phys. Rev. E* **54**, R5897.
- [60] I. SAIKA-VOIVOD, P. H. P. & SCIORTINO, F. 2001 *Nature* **412**, 514.
- [61] JAEGER, H., NAGEL, S. & BEHRINGER, R. 1996 *Rev. Mod. Phys.* **68**, 1259.
- [62] KATAYAMA, Y., *et al.* 1999 *Phys. Rev. Lett.* **82**, 3296.
- [63] KAUZMANN, W. 1948 *Chem. Rev.* **43**, 219.
- [64] KEYES, T. 2000 *Phys. Rev. E* **62**, 7905.

-
- [65] KIM, K. & YAMAMOTO, R. 2000 *Phys. Rev. E* **61**, R41.
- [66] KOB, W. *Lecture notes for LES HOUCHEs 2002* 1st edn. Springer-Verlag Berlin, 2003.
- [67] KOB, W. & ANDERSEN, H. C. 1995 *Phys. Rev. E* **51**, 4626.
- [68] KUMAR, S. K. & SZAMEL, G. <http://xxx.lanl.gov/abs/cond-mat/0508172> .
- [69] LACKS, D. 2001 *Phys. Rev. Lett.* **87**, 225502.
- [70] LEWIS, A. 1972 *Phys. Rev. Lett.* **29**, 1555.
- [71] LIU, J. & LUIJTEN, E. 2004 *Phys. Rev. Lett.*, **92**, 035504.
- [72] LUEDTKE, W. D. & LANDMAN, U. 1988 *Phys. Rev. B* **37**, 4656.
- [73] MAKSE, H., JOHNSON, D. L. & SCHWARTZ, L. M. 2000 *Phys. Rev. Lett.* **84**, 4160.
- [74] MARQUES, M. & STANLEY, H. E. <http://xxx.lanl.gov/abs/cond-mat/0603768> .
- [75] MARTIN, R. M. *Electronic structure: Basic theory and practical methods* 1st edn. Cambridge, 2004.
- [76] MEZARD, M. 1999 *Physica A* **265**, 352.
- [77] MEZARD, M. & PARISI, G. 1999 *J. Chem. Phys.* **111**, 1076.
- [78] MILLER, M. A., DOYE, J. P. K. & WALES, D. J. 1999 *Phys. Rev. E*. **60**, 3701.

-
- [79] MISHIMA, O. & STANLEY, H. E. 1998 *Nature* **396**, 329.
- [80] MONASSON, R. 1995 *Phys. Rev. Lett.* **75**, 2847.
- [81] MONKHORST, H. J. & PACK, J. D. 1990 *Phys. Rev. B* **13**, 5188.
- [82] MOSSA, S., NAVE, E. L., STANLEY, H. E., DONATI, C., SCIORTINO, F. & TARTAGLIA, P. 2002 *Phys. Rev. E* **65**, 041205.
- [83] MOTT, N. *Conduction in Non-Crystalline Materials* 2nd edn. Oxford University Press, USA, 1987.
- [84] MÜLLER-PLATHE, F. 1999 *Phys. Rev. E* **59**, 4894.
- [85] MURANAKA, T. & HIWATARI, Y. 1995 *Phys. Rev. E* **51**, R2735.
- [86] NAGEL, S. R. & LIU, A. 1998 *Nature*. **369**, 21.
- [87] NAVE, E. L., STANLEY, H. E. & SCIORTINO, F. 2001 *Phys. Rev. Lett.* **88**, 035501.
- [88] O'HERN, C. S., LANGER, S. A., LIU, A. J. & NAGEL, S. R. 2001 *Phys. Rev. Lett.* **86**, 111.
- [89] O'HERN, C. S., LANGER, S. A., LIU, A. J. & NAGEL, S. R. 2002 *Phys. Rev. Lett.* **88**, 075507.
- [90] O'HERN, C. S., LANGER, S. A., LIU, A. J. & NAGEL, S. R. 2003 *Phys. Rev. E*. **68**, 011306.
- [91] ONO, I., O'HERN, C., DURIAN, D., LANGER, S., LIU, A. & NAGEL, S. 2002 *Phys. Rev. Lett.* **89**, 095703.

-
- [92] PAYNE, M. C. 1992 *Rev. Mod. Phys* **64**, 1045.
- [93] PERERA, D. & HARROWELL, P. 1999 *Phys. Rev. E* **59**, 5721.
- [94] POOLE, P. H., SCIORTINO, F., ESSMANN, U. & STANLEY, H. E. 1992 *Nature* **334**, 360.
- [95] ROGER, F. J. & YOUNG, D. A. 1984 *Phys. Rev. A.* **30**, 999.
- [96] ROSENFELD, Y. & TARAZONA, P. 1998 *Mol. Phys.*, **95**, 141.
- [97] SAIKA-VOIVOD, I., POOLE, P. H., & SCIORTINO, F. 2000 *Nature* **412**, 514.
- [98] SAIKA-VOIVOD, I., SCIORTINO, F. & POOLE, P. H. 2001 *Phys. Rev. E* **63**, 011202.
- [99] SANTEN, L. & KRAUTH, W. 2000 *Nature* **405**, 550.
- [100] SASTRY, S. 2000 *Phys. Rev. Lett.* **85**, 590.
- [101] SASTRY, S. 2000 *Phys. Chem. Comm.* **14**.
- [102] SASTRY, S. 2001 *Nature* **409**, 164.
- [103] SASTRY, S. & ANGELL, C. A. 2003 *Nature Materials* **2**, 739.
- [104] SASTRY, S., DEBENEDETTI, P. G. & STILLINGER, F. H. 1998 *Nature* **393**, 554.
- [105] SASTRY, S., DEBENEDETTI, P. G., STILLINGER, F. H., SCHRÖDER, T., DYRE, J. C. & GLOTZER, S. C. 1999 *Physica A* **270**, 301.

-
- [106] SCALA, A., STARR, F. W., NAVE, E. L., SCIORTINO, F. & STANLEY, H. E. 2000 *Nature* **406**, 166.
- [107] SCHEIDLER, P., W. KOB, A. L., HORBACH, J. & BINDER, K. 2001 *Phys. Rev. B* **63**, 104204.
- [108] SCHRÖDER, T. B., SASTRY, S., DYRE, J. & GLOTZER, S. 2000 *J. Chem. Phys.* **112**, 9834.
- [109] SCIORTINO, F., KOB, W. & TARTAGLIA, P. 1998 *Phys. Rev. Lett.* **83**, 3214.
- [110] SCIORTINO, F. & TARTAGLIA, P. 1997 *Phys. Rev. Lett.* **78**, 2385.
- [111] SMITH, A. P. & ASHCROFT, N. W. 1985 *Phys. Rev. Lett.* **59**, 1365.
- [112] SPAEPEN, F. & TURNBULL, D. *Laser-Solid Interactions and Laser Processing - 1978* 50th edn. AIP Conf. Proc., 1990.
- [113] SPEEDY, R. J. 1993 *Mol. Phys.* **80**, 1105.
- [114] STARR, F. W., HARRINGTON, S., SCIORTINO, F. & STANLEY, H. E. 1999 *Phys. Rev. Lett.* **82**, 3629.
- [115] STILLINGER, F. 1995 *Science* **267**, 1935.
- [116] STILLINGER, F. H. & HODGON, J. A. 1994 *Phys. Rev E* **50**, 2064.
- [117] STILLINGER, F. H. & WEBER, T. A. 1982 *Phys. Rev. A* **25**, 978.
- [118] STILLINGER, F. H. & WEBER, T. A. 1984 *Science* **225**, 983.
- [119] STILLINGER, F. H. & WEBER, T. A. 1985 *Phys. Rev. B* **31**, 5262.

- [120] TAMMAN, G. & HESSE, W. 1926 *Z. Anorg. Allg. Chem.* **156**, 245.
- [121] TANGUY, A., WITTMER, J., LEONFORTE, F. & BARRAT, J. 2002 *Phys. Rev. B* **66**, 174205.
- [122] TANGUY, A., WITTMER, J. P., LEONFORTE, F. & BARRAT, J.-L. 2002 *Phys. Rev. B* **66**, 174205.
- [123] TARJUS, G. & KIVELSON, D. 1995 *J. Chem. Phys.* **103**, 3071.
- [124] TEUKOLSKY, VALLERING & FLANNERY *Numerical Recipes in Fortran* 2nd edn. Cambridge, 2000.
- [125] THOMPSON, M. O., GALVIN, G. J. & MAYER, J. W. 1984 *Phys. Rev. Lett.* **52**, 2360.
- [126] THOULESS, D. J. 1974 *Phys. Rep.* **13**, 93.
- [127] TRAPPE, V., PRASAD, V., CIPELLETTI, L., SEGRE, P. & WEITZ, D. 2001 *Nature* **411**, 772.
- [128] VAN BEEST, B. W. H., KRAMER, G. J. & VAN SANTEN, R. A. 1990 *Phys. Rev. Lett.* **64**, 1955.
- [129] VEYTSMAN & KOTELYANSKII *Online Notes: Statistical Thermodynamics of Materials*. <http://www.plmsc.psu.edu/www/matsc597c-1997/index.html>.
- [130] VOGEL, H. 1921 *Phys. Ziet.* **22**, 645.
- [131] WAHNSTRÖM, G. & LEWIS, L. 1993 *Physica A* **201**, 150.

-
- [132] WITTMER, J., TANGUY, A., BARRAT, J. & LEWIS, L. 2002 *Europhys. Lett.* **57**, 423.
- [133] YAMAMOTO, R. & ONUKI, A. 1998 *Phys. Rev. E* **58**, 3515.
- [134] ZERAH, G. & HANSEN, J.-P. 1986 *J. Chem. Phys.* **84**, 2336.
- [135] ZIMAN, J. M. 1961 *Phil. Mag.* **6**, 1013.

536.7
p06